Laboratory Studies of Planetary Atmospheres and Organic Hazes

by

Melissa S. Ugelow

B.S. Muhlenberg College, 2012

A thesis submitted to the
Faculty of the Graduate School of the
University of Colorado in partial fulfillment
of the requirements for the degree of
Doctor of Philosophy
Department of Chemistry and Biochemistry
2018

This thesis entitled:

Laboratory Studies of Planetary Atmospheres and Organic Hazes

written by Melissa S. Ugelow

has been approved for the Department of Chemistry and Biochemistry

Dr. Margaret A. Tolbert

Dr. Eleanor C. Browne

Date ___________________

The final copy of this thesis has been examined by the signatories, and we find that both the content and the form meet acceptable presentation standards of scholarly work in the above mentioned discipline.

Ugelow, Melissa S. (Ph.D., Chemistry)

Laboratory Studies of Planetary Atmospheres and Organic Hazes

Thesis directed by Professor Margaret A. Tolbert

Atmospheric organic hazes are present in many planetary and satellite atmospheres, possibly including the ancient Earth. Haze composition and how a haze influences surface and atmospheric processes will greatly depend on the atmospheric composition of the planetary body. Therefore, laboratory studies are necessary to determine these atmosphere specific haze properties. This thesis focuses on the chemical, optical and physical properties of Titan and Archean Earth organic haze analogs, along with gas-phase neutral and ion measurements during haze analog formation.

Titan haze analogs were formed by ultraviolet (UV) and spark discharge excitation of various concentrations of methane in nitrogen in a flow-through reactor. The optical properties of these hazes were measured as a function of methane concentration and were found to have increasing light absorption with increasing aromatic and nitrogen content. To monitor the gas-phase during haze analog formation, a new recirculating reactor was used. The concentration of smaller chained hydrocarbons and nitriles, and the isotopic fractionation of carbon in the methane and evolved ethane, was measured as a function of reaction time. Both methane and ethane become enriched in ^{13}C relative to the starting gas mixture.

Archean Earth haze analogs were formed by UV excitation of methane, carbon dioxide, nitrogen and increasing amounts of molecular oxygen in a flow through reactor. As precursor molecular oxygen increases, the particles become more oxidized and non-absorbing. Therefore, haze produced in an oxygen containing atmosphere could form a non-absorbing haze.

Moreover, since Titan's haze is influenced by ion-neutral chemistry, it is possible similar chemistry occurred in the Archean Earth's atmosphere. Archean Earth haze analog production and negative ion concentrations were found to be inversely related, with aerosol mass loading decreasing with increasing precursor molecular oxygen. Additionally, the nitrogen containing ions switch from mainly organic nitrogen to inorganic nitrogen with increasing precursor molecular oxygen, possibly indicative of the chemistry that occurred during the rise of oxygen in Earth's atmosphere. Due to the differences in haze formation and haze properties based on precursor gases, the results of this thesis demonstrate the importance of considering the atmospheric species present during haze formation.

Dedication

To my parents and sister. For every word of encouragement and for always believing in me, thank you.

Acknowledgements

When I first met with my adviser, Maggie Tolbert, I told her I wanted to study the optical properties of Earth aerosol. Maggie told me that she did not have any available funding for me to begin a new project on this topic, but that I could learn the same techniques and apply them to Titan's aerosol. Maggie assured me once she had funding for Earth aerosol projects, I could switch over to studying Earth. Six years and a thesis later, thank you Maggie for introducing me to planetary science. I cannot imagine studying anything else. You have always supported me and helped me gain the confidence to be an independent scientist. Thank you for teaching me how to give good presentations and how to make writing one of my strengths.

The current Tolbert group members have helped me become a better scientist and presenter, and have made graduate school a positive experience for me. I have learned most of the instruments and techniques that I used in my thesis projects from past Tolbert group members. Heidi Yoon taught me how to make gas mixtures and Kyle Zarzana taught me how to use and maintain the optical system. Thank you Danielle Nuding, Raina Gough and Sarah Hörst for all of your career advice and support.

Thank you Professor Ellie Browne for letting me use the APi-ToF-MS for haze experiments and for all of your help with understanding ion chemistry. Both Jenny Berry and Aroob Abdelhamid ran the APi-ToF-MS and taught me how to use the data analysis software. Thank you both for letting me work in your office for as many days as I did. Doug Day taught me how to use the Q-AMS and has provided years of AMS help. Darin Toohey and Leah Williams also provided help and support with the Q-AMS. David De Haan measured and analyzed the CAPS data. Thank you Melissa Trainer for the NASA internship experience and for being a mentor to me. Also, thank you for flying across the country to be on my thesis committee.

In addition to being a part of the "current Tolbert group members", Katie Primm has been my life jacket and my best friend. You have made graduate school a place I looked forward to going to each day. I cannot imagine graduate school without you and I am so glad I only have had to experience this for 12 days. Good luck at SwRI. I know you will be incredibly successful during your postdoc and beyond.

I would not be here today without the love and support of my mom and dad, my sister Lisa, and Ian. You have always believed in me and have been my biggest cheerleaders. You have always encouraged me to go after my dreams and to never give up. Thank you.

Contents

List of Figures

List of Tables

1 Introduction

1.1 Planetary Hazes

Any planetary body with a reduced atmosphere containing methane has the potential to form an organic atmospheric haze. In our solar system, organic hazes have been reported for Titan, Jupiter, Saturn, Uranus, Neptune and, most recently, Pluto (Gladstone et al., 2016; Pyror and Hord, 1991; Wagener et al., 1986). Additionally, haze could possibly have formed in the atmosphere of the ancient Earth (Sagan and Chyba, 1997). Because haze particles can absorb and scatter light, hazes can greatly impact atmospheric and surface properties, including the radiative balance (McKay et al., 1989, 1991) and surface albedos (Griffith et al., 2003, 2012; Hirtzig et al., 2013; Negrão et al., 2006). Figure 1.1 demonstrates how incoming light from the sun can interact with haze particles. When particles scatter the incoming light (1.1a), the result is a local cooling. When particles absorb the incoming light (1.1b), it is re-emitted as heat, causing local warming. Thus, hazes can significantly influence surface and atmospheric temperatures (Pavlov et al., 2001; Haqq-Misra et al., 2008), as well.

1.2 Titan's Organic Haze

Titan, one of Saturn's satellites, is the only moon in our solar system with a considerable atmosphere and the only known planetary object besides Earth with a thick atmosphere that contains mainly nitrogen (N_2). Unlike the current Earth, however, where the next major atmospheric species is oxygen (O_2), in Titan's atmosphere, the next major atmospheric species is methane (CH_4). Complex reactions between CH_4 and N_2, initiated by solar photons and high energy electrons from Saturn's magnetosphere, result in the formation of a thick organic haze around the whole moon, down to Titan's surface (Tomasko et al., 2005). Figure 1.2 includes two images from the Cassini-Huygens mission with Figure 1.2a, taken by the Cassini orbiter, showing the haze layers in the upper atmosphere above the main haze and Figure 1.2b, taken by the Huygens Probe upon landing on Titan's surface, showing the

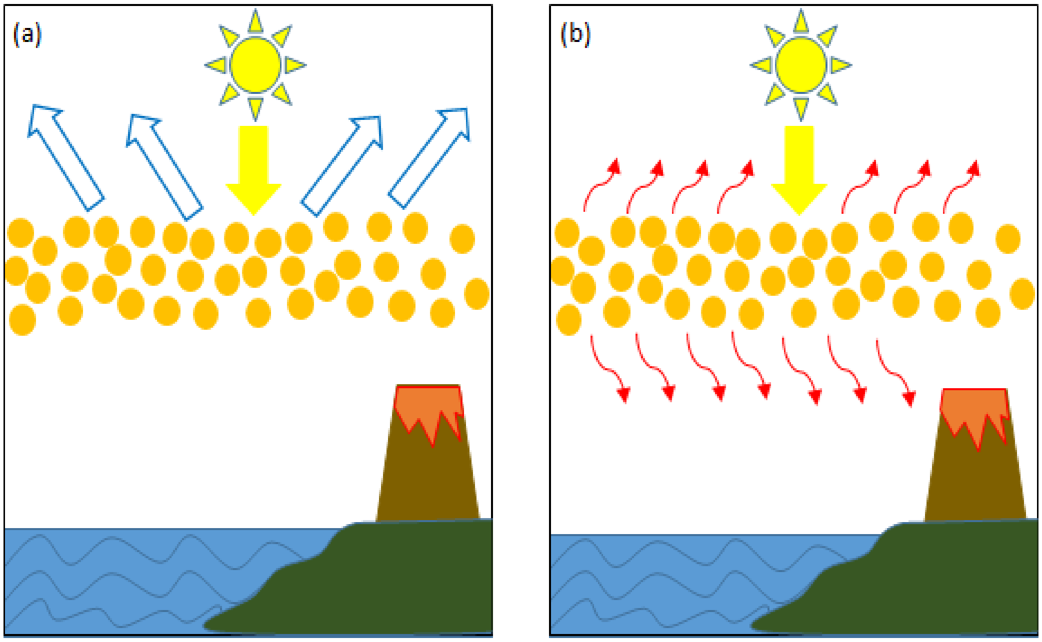

Figure 1.1: (a) Haze particles can scatter incoming light, resulting in local cooling or (b) haze particles can absorb incoming light and re-emit the light as heat, causing local warming.

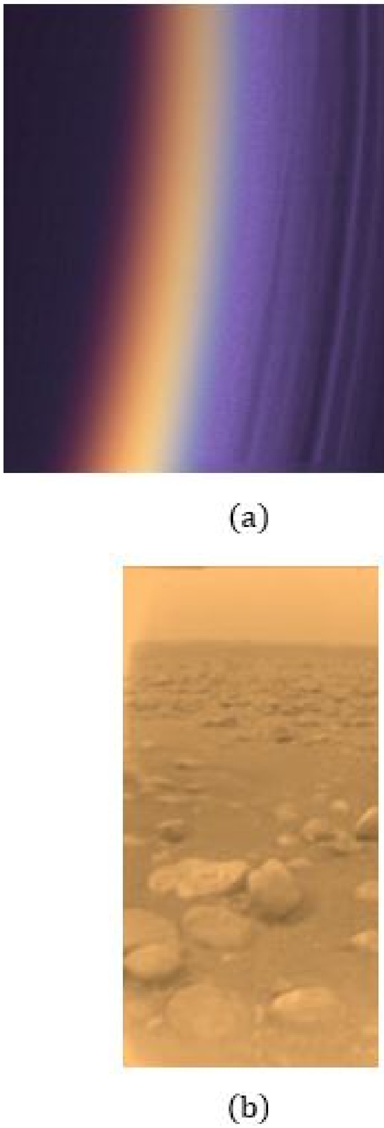

Figure 1.2: (a) Ultraviolet image taken by the Cassini orbiter of the detached haze layers in Titan's upper atmosphere. Image was colorized to look like true colors and was taken December 16, 2004 at about 10°S. NASA/JPL/Space Science Institute. (b) Image taken by the Huygens Probe upon landing on Titan's surface. Image was received from the probe on January 14, 2005 and was colored based on reflection spectra. Photo credit: ESA/NASA/JPL/University of Arizona

presence of haze at Titan's surface. The notional haze formation pathway is summarized in Figure 1.3, which shows that reactions between CH_4 and N_2 initiated by solar photons and energetic particles form ions and neutral species. The ions and neutrals react to make larger molecules, possibly polycyclic aromatic hydrocarbons. As these species travel down through Titan's atmosphere, they continue to react and become larger, ultimately forming aerosol particles. These particles can eventually settle out of the atmosphere and are deposited on Titan's surface.

Before the Cassini-Huygens mission, much about Titan was still a mystery. Being enshrouded in haze limited surface and atmospheric observations by Pioneer 11, Voyager 1 and 2, and ground based telescopes. Figure 1.4 shows images of Titan, obscured by its haze, taken by Pioneer 11, Voyager 1 and Voyager 2. With the Cassini-Huygens mission, however, a distant world similar to Earth was found. Like on Earth where there is a water cycle, Titan has a methane cycle (Atreya et al., 2006; Lunine and Atreya, 2008). For both Earth and Titan this is only possible due to the surface conditions being near the triple point of water and methane, respectively. While the methane cycle is not fully understood due to the unknown subsurface methane reservoirs, surface liquid methane in lakes (Le Gall et al., 2016), convectively-induced methane clouds (Griffith et al., 2000; Roe et al., 2002; Turtle et al., 2009, 2011a), and likely methane rainfall (Turtle et al., 2011b) all participate in Titan's methane cycle. Additionally, like Earth, Titan has surface sand dunes (Elachi et al., 2006; Lorenz et al., 2006) and mountains (Radebaugh et al., 2007).

Along with unprecedented Titan surface measurements by the Cassini-Huygens mission, remote sensing and in-situ atmospheric measurements were also taken of Titan's atmosphere. The Ion Neutral Mass Spectrometer (INMS) and the Composite Infrared Spectrometer (CIRS) detected neutral hydrocarbon and nitrile gases including C_2H_2, C_2H_4, C_2H_6, C_3H_8, CH_3C_2H, C_4H_2, C_6H_6, HCN, CH_3CN, HC_3N and C_2N_2 (Coustenis et al., 2007; Vinatier et al., 2007b; Waite Jr. et al., 2007; Cui et al., 2009; Magee et al., 2009). Additionally, atmospheric observations detected gaseous ions in the upper atmosphere, leading to the

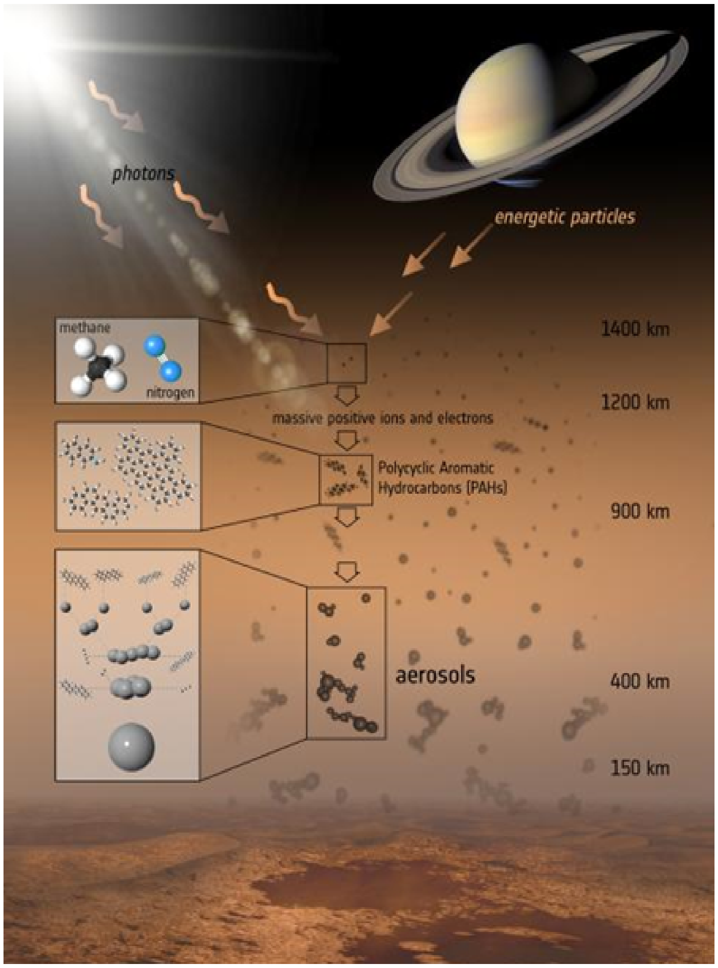

Figure 1.3: Summary of Titan's haze formation pathway. Reactions between CH_4 and N_2 are initiated by solar photons and energetic electrons from Saturn's magnetosphere. The ion and neutral products then react further and make larger molecules, possibly polycyclic aromatic hydrocarbons. As the molecules descend through Titan's atmosphere they become larger and form aerosol particles. The ultimate fate of the aerosol is deposition onto Titan's surface. Photo credit: ESA/ATG Media Lab.

Pioneer 11

Voyager 1

Voyager 2

Figure 1.4: Images of Titan taken during Pioneer 11, Voyager 1 and Voyager 2 missions. Photo credit: NASA Ames and NASA/JPL

determination of haze formation pathways.

In Titan's atmosphere, haze production begins in the upper atmosphere through ion-neutral chemistry (Waite Jr. et al., 2007; Coates et al., 2007, 2010; Wahlund et al., 2009; Lavvas et al., 2013) initiated between CH_4 and N_2. As ions react with neutrals and oppositely charged ions in the ionosphere, they can become aerosol (Lavvas et al., 2013). Evidence of positive ions in Titan's upper atmosphere was detected by the INMS and the Cassini Plasma Spectrometer Ion Beam Spectrometer (CAPS/IBS) (Cravens et al., 2006; Waite Jr. et al., 2007; Crary et al., 2009). While the INMS can only measure ions with a mass up to 99 Da, the CAPS/IBS can measure ions with a mass up to 350 Da. Both Waite Jr. et al. (2007) and Crary et al. (2009) state the likelihood of the presence of positively charged aromatics and nitrogen containing heterocycles in the INMS and CAPS/IBS data. Evidence of negative ions in Titan's upper atmosphere was detected by the CAPS Electron Spectrometer (ELS) (Coates et al., 2007; Waite Jr. et al., 2007), which measured the presence of heavy ions up to 10,000 amu/q. These heavy negative ions are believed to be important to haze formation chemistry, possibly even being small particles themselves (Lavvas et al., 2013). Due to very low resolution in the CAPS/ELS data, however, the composition of the heavy negative ions cannot be determined.

In addition to understanding how haze forms in Titan's atmosphere, instruments on the Cassini-Huygens measured physical, optical and chemical properties of the haze. Many of these haze properties were measured by the Descent Imager/Spectra Radiometer (DISR) on the Huygens Probe during its descent through the atmosphere of Titan. Based on polarization measurements and single-scattering phase function modeling, haze particles were found to be fractal aggregates with ≤ 50 nm sized monomers (Tomasko et al., 2005, 2008). Additionally, above an altitude of 60 km, the fractal aggregates are composed of about 3,000 monomers (Tomasko et al., 2008). The optical properties of the haze particles at two altitude regions were also measured by DISR, including particle single-scattering albedo. The single-scattering albedo, the ratio of light scattered to the total light extinguished by a type of particle, was measured at altitudes of 30 - 80 km and > 144 km. At both altitudes, the single-scattering albedo increases with the wavelength of light until 900 nm, where then the single-scattering albedo decreases (Tomasko et al., 2008). This means that the haze particles absorb certain infrared wavelengths more strongly than certain visible wavelengths.

The chemical properties of the haze particles were measured by three instruments: the Aerosol Collector Pyrolyzer (ACP), CIRS and the Visible and Infrared Mapping Spectrometer (VIMS). VIMS found haze particles to be rich in C-H bonds (Rannou et al., 2010), with possible particle aging resulting in particle composition changing from an aromatic structure in the upper atmosphere to a more aliphatic structure in the stratosphere (Courtin et al., 2015). Agreeing with VIMS, CIRS found the haze particles to contain mostly C-H and C-C bonds (Vinatier et al., 2012). However, the ACP found the haze particles to be rich in nitrogen (Israël et al., 2005), although these results are controversial and may not reflect the bulk aerosol composition (Biemann, 2006). Therefore, the exact chemical composition of haze particles remains unknown.

Despite the depth of new data provided by the Cassini-Huygens mission about Titan's organic haze and its properties, further information relies heavily on models and laboratory investigations. A portion of this thesis includes the study of the optical and chemical properties of Titan haze analogs, along with the carbon isotopic ratio of the neutral gas-phase species consumed and produced during Titan haze analog formation. The goals of these studies are to further our understanding of haze properties and haze formation in Titan's atmosphere, along with providing input parameters for models that require the input of haze properties.

1.3 An Early Earth Organic Haze

Geological time on Earth is divided into different eons, shown in Figure 1.5, adapted from Kasting and Ono (2006), with the earliest eons being the Hadean and Archean. While it is possible life existed earlier (Dodd et al., 2017), the first direct evidence of life on Earth

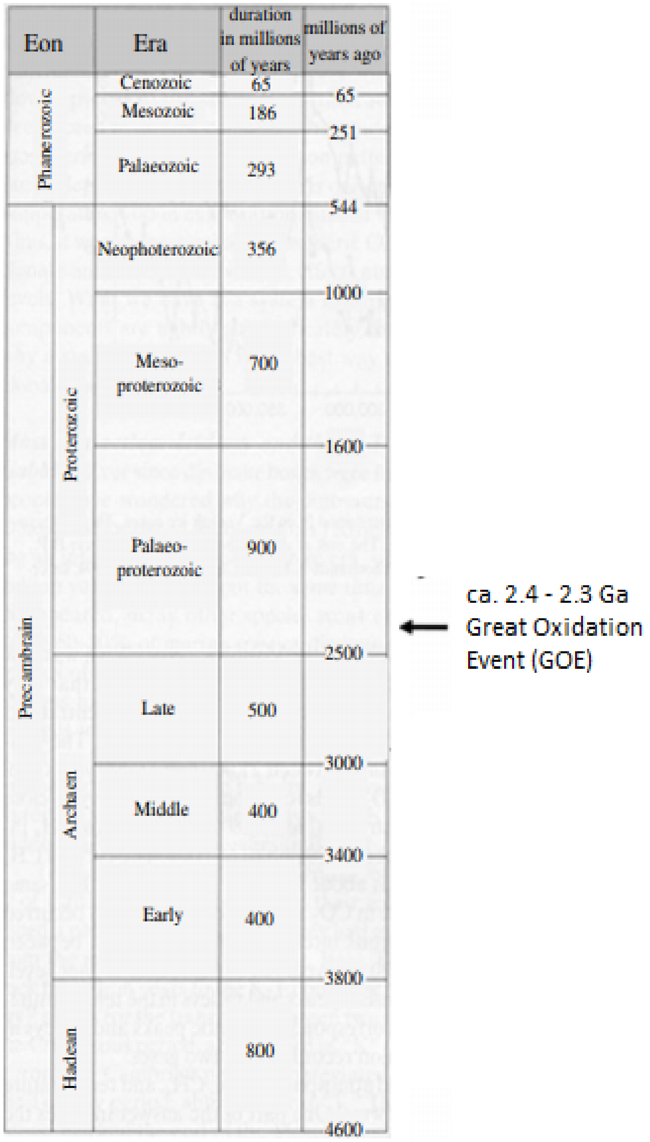

Eon		Era	duration in millions of years	millions of years ago
Phanerozoic		Cenozoic	65	65
		Mesozoic	186	251
		Palaeozoic	293	544
Precambrian	Proterozoic	Neophoterozoic	356	1000
		Meso-proterozoic	700	1600
		Palaeo-proterozoic	900	2500
	Archaen	Late	500	3000
		Middle	400	3400
		Early	400	3800
	Hadean		800	4600

ca. 2.4 - 2.3 Ga
Great Oxidation
Event (GOE)

Figure 1.5: Geological time, adapted from Kasting and Ono (2006).

was during the Archean, with the oldest microfossils aged at 3.5 Ga (Ga; billions of years ago) (Awramik, 1992; Schopf, 1993). However, the atmospheric conditions during this time are quite uncertain. Over the course of geological time, the solar luminosity has increased by 40 ± 10 % (Sagan and Mullen, 1972), so during the Archean, the young sun's solar luminosity would have been reduced. Using the lower bound of this solar luminosity change, Sagan and Mullen (1972) calculated that without an atmosphere, sea water would have been frozen during all of Earth's history (Effective Temperature). With the Earth's current greenhouse gases included in their model (CO_2 and H_2O), surface liquid water could have existed on Earth's surface since approximately 2.3 Ga. However, based on evidence from the geological record, liquid surface water dates back to 4.4 Ga (Wilde et al., 2001). Adding other greenhouse gases to their model, like NH_3, CH_4 and H_2S, result in an overall warmer Earth that could have supported surface liquid water since its formation (4.6 Ga). Results of Sagan and Mullen (1972) are summarized in Figure 1.6.

To maintain liquid water with a faint young sun at times that agree with the geological record, models typically include methane and carbon dioxide as greenhouse gases. However, the estimated atmospheric methane and carbon dioxide concentrations needed to warm the planet could have led to the formation of a photochemical organic haze in the atmosphere of the ancient Earth (Sagan and Chyba, 1997; Trainer et al., 2004, 2006; Domagal-Goldman et al., 2008; Haqq-Misra et al., 2008; DeWitt et al., 2009; Hasenkopf et al., 2010). While the amounts of these gases varied during the Archean, previous laboratory studies have shown that haze can exist with CO_2:CH_4 ratios as high as 10:1 (DeWitt et al., 2009), supporting the possibility of a haze during much of Earth's ancient history. Moreover, the atmospheric conditions necessary to support organic haze formation during the Neoarchean (2.8-2.5 Ga) is supported by geological analysis by Zerkle et al. (2012), Kurzweil et al. (2013) and Izon et al. (2015). The presence of an atmospheric haze is important to consider when examining the evolution of life since haze can be composed of prebiotic molecules, like nucleotide bases and amino acids (Hörst et al., 2012), and can also modulate surface temperatures, and thus

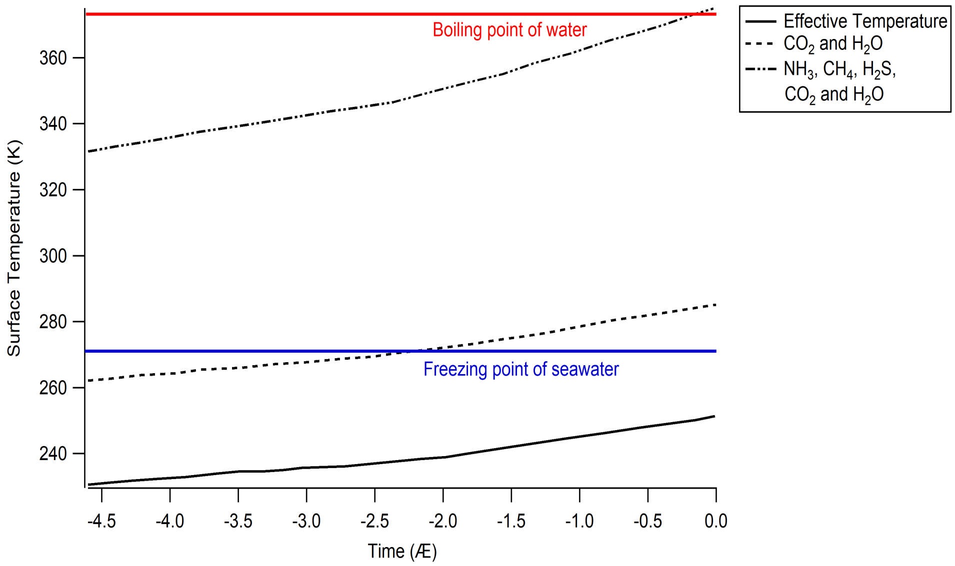

Figure 1.6: Surface temperatures with a faint young sun based on different atmospheric compositions from Sagan and Mullen (1972). To maintain surface liquid water with a faint young sun, greenhouse gases are necessary.

the presence of surface liquid water (Arney et al., 2016).

Laboratory studies have demonstrated that an Archean haze formed in a $CO_2/CH_4/N_2$ atmosphere would be chemically distinct from a haze that was formed in the absence of any major oxygenated species (Trainer et al., 2006; Hicks et al., 2015, 2016). In addition to CO_2 influencing the chemistry during haze formation, it could also lead to the synthesis of molecular O_2 when photolyzed. While the O_2 levels during the Archean are uncertain, it is generally believed that before the Great Oxidation Event (GOE, ca. 2.4 - 2.3 Ga; Figure 1.5), the Archean atmosphere at most contained 2 ppmv O_2 (Kasting et al., 2001; Pavlov and Kasting, 2002). However, Kasting (1993) and Segura et al. (2007) suggest that a planet with 0.2 bars CO_2 could contain up to tenths of a percent of stratospheric O_2 by CO_2 photolysis. In addition, with paleosol chromium isotope analysis, Crowe et al. (2013) found that up to 63 ppm of atmospheric O_2 may have existed as long as 3 Ga. Immediately following the GOE, atmospheric oxygen is estimated to have increased to 0.02 - 0.04 atmospheric pressure (Holland, 2006). Therefore, the presence of molecular oxygen, in any of these quantities, could have altered haze formation chemistry since oxygen is believed to terminate haze production by initiating reactions that oxidize the gas-phase species before they polymerize into haze (Zahnle, 1986).

The influence of molecular O_2 on haze formation and haze properties has only recently began to be studied in the laboratory, and includes the work in this thesis. Like the models for Titan's atmosphere and atmosphere-surface interactions, the models for the early Earth rely on laboratory studies to provide necessary input factors and reaction mechanisms. The second portion of this thesis includes the study of the chemical, physical and optical properties of early Earth haze analogs and the ion chemistry during early Earth haze analog formation. By producing haze analogs with and without the addition of increasing amounts of molecular O_2, this work aims to study haze analogs relevant to the Archean leading up to the Great Oxidation Event.

1.4 Thesis Outline

This thesis explores the chemical, physical and optical properties of planetary haze analogs relevant to Titan and the early Earth. The gas-phase neutrals and ions that are present during haze formation are also studied. The experimental setup used to generate haze analogs, along with the analytical instrumentation and techniques used for analysis, are explained in detail in Chapter 2. In Chapter 3, the optical and chemical properties of discharge-generated organic hazes are explored as a function of abundance of precursor CH_4, with relevance to Titan. The chemical, physical and optical properties of oxidized aerosol, with relevance to the Archean Earth, are investigated in Chapter 4. The ions that are present during Archean Earth analog formation are measured and their connection to haze analog formation and the evolution of the early Earth is investigated in Chapter 5. In Chapter 6, the neutral gas-phase species that are produced during Titan haze analog formation are explored, along with the isotopic fractionation of carbon in these species. The work in Chapter 6 is from an ongoing project that was started during an internship at NASA Goddard Space Flight Center with Dr. Melissa Trainer. Lastly, Chapter 7 includes the overall conclusions from this thesis along with suggestions for future work.

2 Experimental Setup, Instrumentation and Techniques

The following chapter describes the experimental setup, instrumentation and techniques used during the studies described in the thesis. The instruments used by collaborators are briefly described in the experimental section within the specific project chapter.

2.1 Haze Particle Production

Planetary haze analogs have been produced in the Tolbert laboratory previously (Trainer et al., 2004, 2006, 2012, 2013; DeWitt et al., 2009; Hasenkopf et al., 2010; Hörst and Tolbert, 2013; Hörst et al., 2018b; Yoon et al., 2014; Hicks et al., 2015, 2016; Ugelow et al., 2017) using the flow system shown as a schematic in Figure 2.1. Precursor gases are flowed into a mixing chamber where they mix for at least 8 hours. For Titan atmospheric simulations, CH_4 and N_2 are used. For early Earth atmospheric simulations, CO_2, and in some simulations O_2, is included as well. With the exception of N_2, the partial pressures of each precursor gas is measured by a baratron (MKS). The N_2 pressure is controlled by the regulator on the N_2 gas cylinder. Then, using a mass flow controller (MFC; Mykrolis, FC-2900), the mixed gases flow at either 60 or 100 standard cubic centimeters per minute (sccm) to the reaction cell where either a spark discharge energy source or a UV lamp is used to form haze particles at ambient conditions (∼620 Torr and 20 °C). The haze particles then flow to an analyzer. The haze particles are always suspended in the gas flow so no deposition onto a substrate is needed. The experiments discussed in Chapters 3, 4 and 5 use this flow system to produce haze particles.

2.1.1 Spark Discharge

Spark discharge excitation was the energy source used for the experiments discussed in Chapter 3. The voltage source was a tesla coil (Electro Technic Products) that outputs

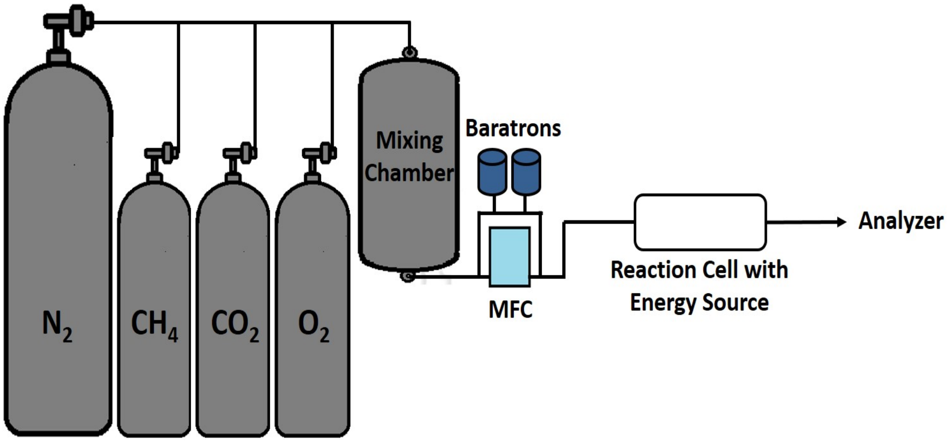

Figure 2.1: Schematic of the aerosol production flow system.

.

between 20 and 50 kV. To produce haze particles, the tesla coil was set to output a voltage of 30 - 35 kV. For the experiments that used the spark discharge energy source, a glass reaction cell with tungsten electrodes spaced 1.27 cm across the height of the cell was used.

The energy output from the tesla coil is greater than even the most energetic of Saturn's magnetospheric electrons that interact with Titan's upper atmosphere, with energies that range from 10 eV to 5 keV (Brown et al., 2009). However, the tesla coil source is used to provide enough energy to directly dissociate the N_2 triple bond. This allows for the study of the impact of nitrogen incorporation in haze particles on haze optical properties.

2.1.2 UV Lamp

To simulate the photochemistry that could have resulted in an organic haze in the atmosphere of the early Earth and haze formation pathways in Titan's atmosphere, a UV energy source was used. The UV energy source is a water-cooled deuterium continuum lamp with a MgF_2 window that emits wavelengths between 115 and 400 nm. The lamp's peak intensity output occurs between 115 and 165 nm. This peak overlaps with the strong absorption cross sections of CH_4 (Kameta et al., 2002; Chen and Wu, 2004; Mount et al., 1977), CO_2 (Yoshino et al., 1996; Stark et al., 2007) and O_2 (Lu et al., 2010), and is shown in Figure 2.2. The UV lamp is inserted directly into the UV glass reaction cell with a custom-made 2" O-ring compression connection fitting. A deuterium continuum lamp was the energy source used for the experiments discussed in Chapter 4, 5 and 6.

After each experiment, the MgF_2 window on the lamp was cleaned using a cleaning solution and lens tissue (Thor Labs). The MgF_2 window was cleaned in order to prevent particles from building up on the window, which could cause a decline in the lamp's output from particle absorption, and to prevent contamination between experiments if the particle film participates in the next experiment's chemistry. For the experiments without the addition of an oxygen-containing precursor gas, the cleaning solution was a 60:40 acetone:methanol mixture. For experiments with the addition of an oxygen-containing precursor gas, the clean-

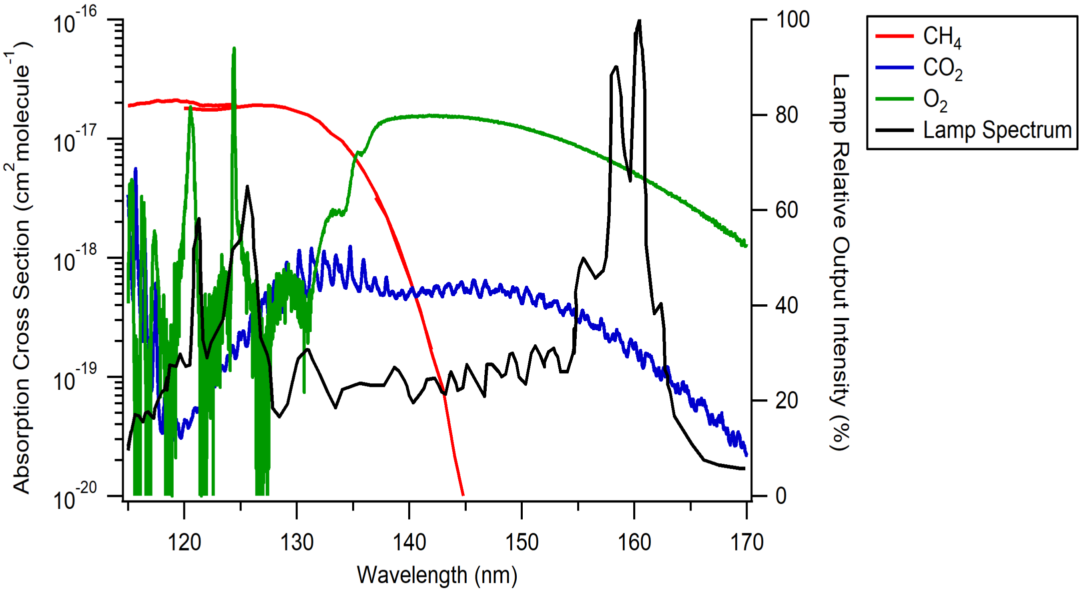

Figure 2.2: Peak emission spectrum of the UV lamp used to make photochemical haze particles and the absorption cross sections of the gases used in the experiments at these wavelengths, as well

ing solution was a 25:75 acetone:methanol mixture. Experiments with an oxygen-containing precursor gas and experiments with no oxygen-containing precursor gas needed different cleaning solutions due to the differences in the chemical properties of the haze particles. The haze particles produced with an oxygen-containing precursor gas were more polar than the haze particles produced with no oxygen-containing precursor gas, and therefore needed a more polar cleaning solution to dissolve the particle film on the lamp.

2.2 Recirculation System

For the studies described in Chapter 6, rather than producing haze particles in the flow system described in Chapter 2.1, haze particles were produced in a recirculation system. Built during an internship at NASA Goddard Space Flight Center with Dr. Melissa Trainer, the recirculation system allows for the study of the neutral gases produced during haze formation as a function of reaction time. Here the method of making gas mixtures to simulate Titan's atmosphere is identical to the method using the flow system. Once the gases are mixed, they enter a closed system instead of an open system that is interfaced to an analyzer.

A schematic of the recirculation is shown in Figure 2.3. Like the flow system, the mixing chamber is connected with stainless steel tubing to the UV reaction cell. On one side of the UV reaction cell an air-cooled deuterium continuum lamp (Hamamatsu, L11798) is connected by a vacuum flange (Hamamatsu, E3444), and on the outlet of the cell there is an aerosol collection chamber. From there, pump tubing (Masterflex, 06442) connects the collection chamber to the inlet of a peristaltic pump (Masterflex, L/S 07528-10P). Because of the pump tubing material, losses due to absorption/adsorption are not expected; however, losses due to the pump tubing were not specifically investigated. The outlet of the peristaltic pump plumbs into the inlet of the recirculation system, before the UV reaction cell. At this point, a gas sampling port is attached for extraction of gas samples with a gas-tight syringe. This design allows the gases to circulate through the closed system continually.

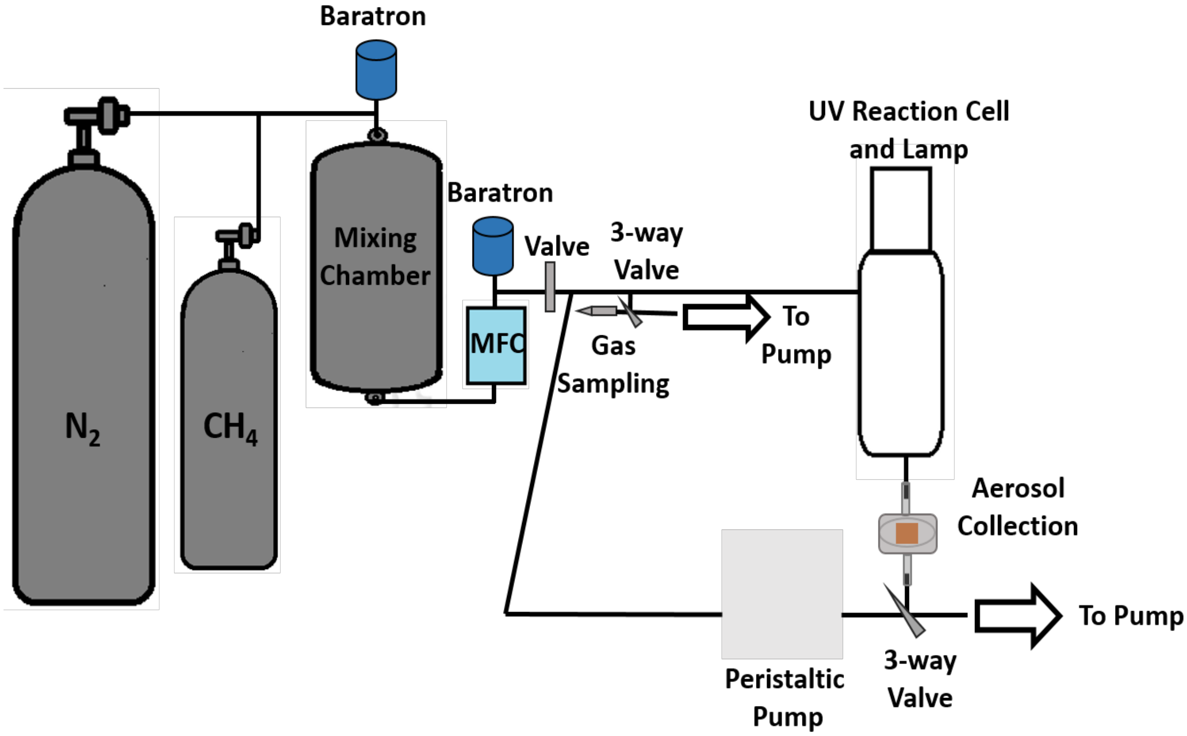

Figure 2.3: Schematic of the recirculation system.

The mixed gases are introduced into the recirculation system to a pressure slightly above ambient conditions (∼800 Torr) to prevent leaks into the system. This also ensures that with gas sampling the pressure remains above or near ambient conditions. Once the system is filled, the recirculation system is isolated from the mixing chamber by a valve. To eliminate dead space, the valve is located just before where the outlet of the peristaltic pump is plumbed into the recirculation system. Once haze particles are being produced, gas and particles flow through a quartz fiber filter (Advantec/QR100 25 mm). Particles are collected on the filter while gases flow through to the peristaltic pump. Particles are collected rather than being allowed to recirculate with gases to prevent clogging the gas-tight syringes and the analyzers' inlets, along with preventing further irradiation of haze particle surfaces. After being recirculated by the peristaltic pump, the gases react again in the UV reaction cell. The gases are constantly recirculating during the experiment at a flow of 100 sccm, set as the rotations per minute (rpm) by the peristaltic pump (20 rpm). Gases are sampled using a gas-tight syringe and are then rapidly transferred and injected into an analyzer.

2.3 Scanning Mobility Particle Sizer

The scanning mobility particle sizer (SMPS) is used to measure the size distribution and mass loading of the haze particles produced in Chapter 4 and 5. The SMPS is a combination of two instruments- a differential mobility analyzer (DMA; TSI, 3081) and a condensation particle counter (CPC; TSI, 3022A). Polydisperse particles flow to an electrostatic classifier (TSI, 3080) where they pass through a Kr-85 bipolar charger. Then the particles flow to the DMA, where a scanning electric field is applied to the particles. The particles are then size-selected based on their electrical mobility in the scanned electric field against the drag force from the sheath flow. The diameter measured by the DMA is the electrical mobility diameter (d_m; the diameter of a unit density sphere with the same electrical mobility in an electric field as the particle of interest; (Flagan, 2001; DeCarlo et al., 2004)). The sized-selected particles then enter the CPC and flow over a butanol reservoir. The butanol condenses onto the particles and the particles grow to a size that can be measured by light scattering, allowing for the number density (N, particles cm^{-3}) at each d_m to be measured. Because of CPC instrument requirements, an additional 200 - 240 sccm of prepurified N_2 dilution flow was added after the flow system reaction cell for measurements with the SMPS.

2.4 Photoacoustic Spectroscopy and Cavity Ring-Down Spectroscopy

To measure the optical properties of haze particles, one of the analyzers used in Chapter 3 and 4 was the combination of photoacoustic spectroscopy and cavity ring-down spectroscopy (PASCaRD). Figure 2.4 shows a schematic of the PASCaRD system used to determine the complex refractive index of haze particles. In these experiments, two channels, one at 405 nm and one at 532 nm, can be used. The current data analysis program used with the PASCaRD system requires measurements in the 405 and 532 nm channels to be done in separate experiments. When using PASCaRD, the polydisperse particles first flow to a DMA to be size-selected. The DMA was calibrated using five different sizes of polystyrene latex spheres (70, 102, 203, 296 and 400 nm) and the uncertainty of the calibration curve for particle size was determined to be ±1 nm. Figure 2.5 shows the calibration curve used to correct for DMA particle size.

Once size selected, the particles pass through the cavity ring-down (CaRD) component of PASCaRD, previously described in detail in Freedman et al. (2009) and Fuchs et al. (2009). The CaRD is composed of a stainless steel tube with highly reflective mirrors on each end (532 nm CaRD: R> 99.998%; 405 nm CaRD: R> 99.994%). The laser light enters as a pulse of light into the cavity and the light is reflected back and forth many times by the highly reflective mirrors. The time it takes for the light to decay to $\frac{1}{e}$ of its original intensity both with (τ) and without (τ_0) aerosol present is measured and the aerosol extinction, with units of inverse megameters, (b_{ext}, Mm^{-1}) is calculated as:

$$b_{ext} = \frac{R_L}{c}(\frac{1}{\tau} - \frac{1}{\tau_0}) \tag{1}$$

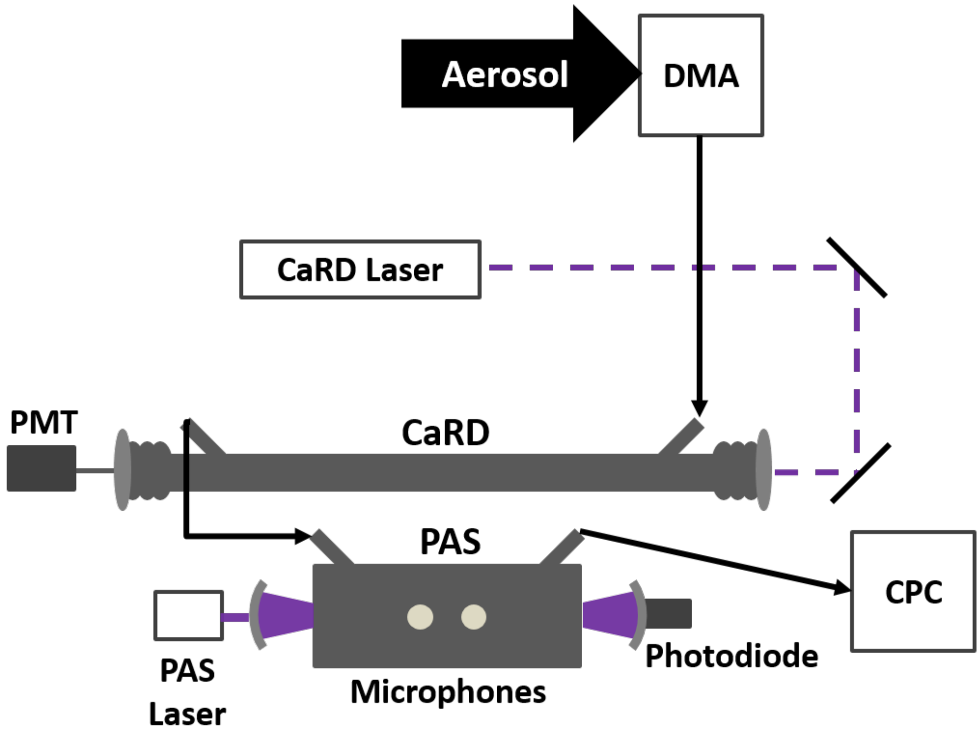

Figure 2.4: Schematic of the photoacoustic and cavity ring-down spectrometers (PASCaRD) with one channel shown for simplicity. Aerosol flows to the differential mobility analyzer (DMA) where particles are size selected. The size-selected particles then flow to the cavity ring-down (CaRD) spectrometer, where aerosol extinction (Mm^{-1}) is measured. Following the CaRD, the particles flow to the photoacoustic spectrometer (PAS), where aerosol absorption (Mm^{-1}) is measured. Finally, the size-selected particles flow to the condensation particle counter (CPC) where the concentration of the particles is measured (particles cm^{-3}).

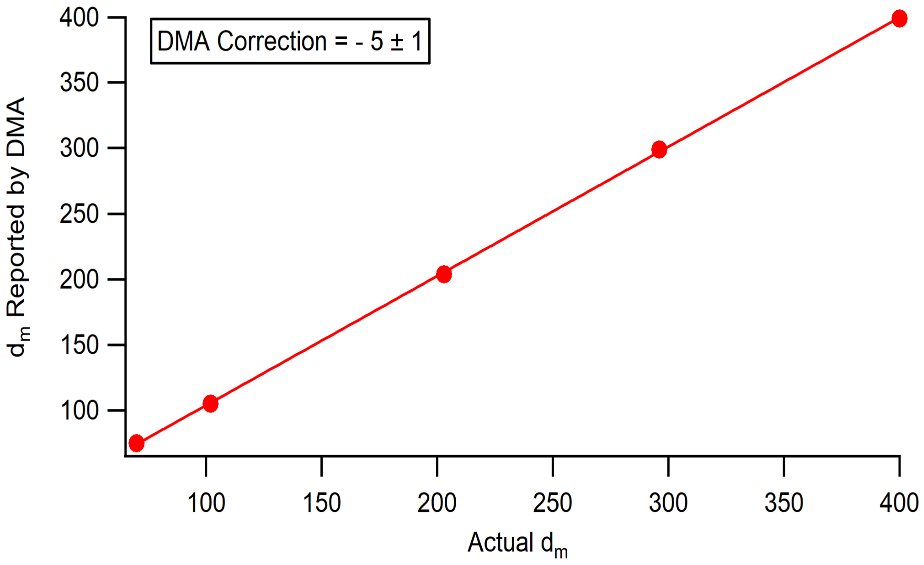

Figure 2.5: DMA size calibration using polystyrene latex spheres.

Here c is the speed of light and R_L is the ratio of the length of the whole cavity (mirror to mirror) to the length of the cavity that particles occupy (the space between the inlet and the outlet) (R_L= 1.13). Typical ring-down times for the 405 and 532 nm CaRD are $\tau_0 = 40$ and 100 μs, respectively. These ring-down times result in an effective pathlength of about 12 and 30 km for the 405 and 532 nm CaRD, respectively.

After the CaRD, the particles then flow to the photoacoustic spectrometer (PAS), based on the design of Lack et al. (2012a). The PAS consists of a resonant cavity and an amplitude-modulated laser. The absorption of light by the particles is measured with a microphone that detects the pressure (sound) wave that the particles emit when expanding and contracting after absorbing the laser light. The absorption signal is read as a voltage. Unlike with CaRD where τ and τ_0 are measured and then used in a calculation to determine b_{ext}, the voltage measured by the microphone needs to be converted to absorption, also with units of inverse megameters, (b_{abs}, Mm^{-1}). This is done by using a calibration factor that results from comparing the extinction of light to the absorption of light by an absorbing gas (Lack et al., 2012a). An absorbing gas is needed since its extinction is almost entirely due to absorption.

In the calibration for the studies detailed in this thesis, ozone generated by exposing oxygen to a mercury pen lamp is used. The extinction of light (measured with the CaRD) and the absorption of light (measured with the PAS) are recorded for many ozone concentrations, controlled by the degree to which the mercury pen lamp is exposed to the flowing oxygen. The raw signal from the PAS is plotted against the CaRD extinction and the points are fit to a line. The slope of that line is the calibration factor. The calibration is done at least two times between different studies to measure the calibration's precision, and the different calibration slopes are always in close agreement resulting in minimal uncertainty. Examples of the linear fit used to determine the calibration factors are shown in Figure 2.6 for the λ = 405 nm channel (a) and the λ = 532 nm channel (b). For both wavelengths the y-intercept of the line is very close to zero (values that are at least < 0.02% of typical PAS signal levels for these experiments), resulting in the following relationship, $\mathrm{b_{ext}}$= PAS Signal/Calibration Slope.

Therefore, to convert the PAS raw signal to b_{abs}, the raw signal is divided by the calibration slope.

Due to the PAS limit of detection, k values less than 0.001 cannot be accurately measured and are reported as $k < 0.001$ rather than $k = 0$. This choice was made since particles that are not entirely scattering can have a k between 0 and 0.001. This limitation can be a source of uncertainty in purely scattering particles and particles that are almost entirely scattering, as well. However, the overall change in particle absorption is minor after three decimal places in k, where the single-scattering albedo for a particle with a k with four decimal places over three decimal places changes by less than a percent.

To check if the gas-phase products and/or unreacted gas-phase species are contributing to the absorption measured by the PAS and to obtain the gas-phase background, the voltage of the DMA is set to zero to prohibit particles from flowing through PASCaRD. This is done at the beginning of an experiment after the UV lamp is turned on and once more during the middle of the experiment, with the UV lamp still on. During this control, there was no absorption measured from the gas-phase species.

Following the PAS, the size-selected particles flow to the condensation particle counter (CPC; TSI, 3022), where the particle concentrations are measured as a number density (N, particles cm^{-3}). Within this PASCaRD system, there are no measurable particle losses from the CaRD to the PAS to the CPC. This was tested by first flowing particles through the entire PASCaRD to the CPC and then flowing particles through the CaRD only to the CPC. There was no difference between the number of particles counted by the CPC in each scenario and therefore the CaRD and PAS are measuring extinction and absorption, respectively, for the same particle concentrations during experiments.

In this study, light extinguished and absorbed was measured for five to seven different haze particle sizes with mobility diameters between 170 and 320 nm. The number of haze particles sizes used is based on the PASCaRD sensitivity study by Zarzana et al. (2014). From the extinction and absorption measurements at each particle size, other size-dependent particle

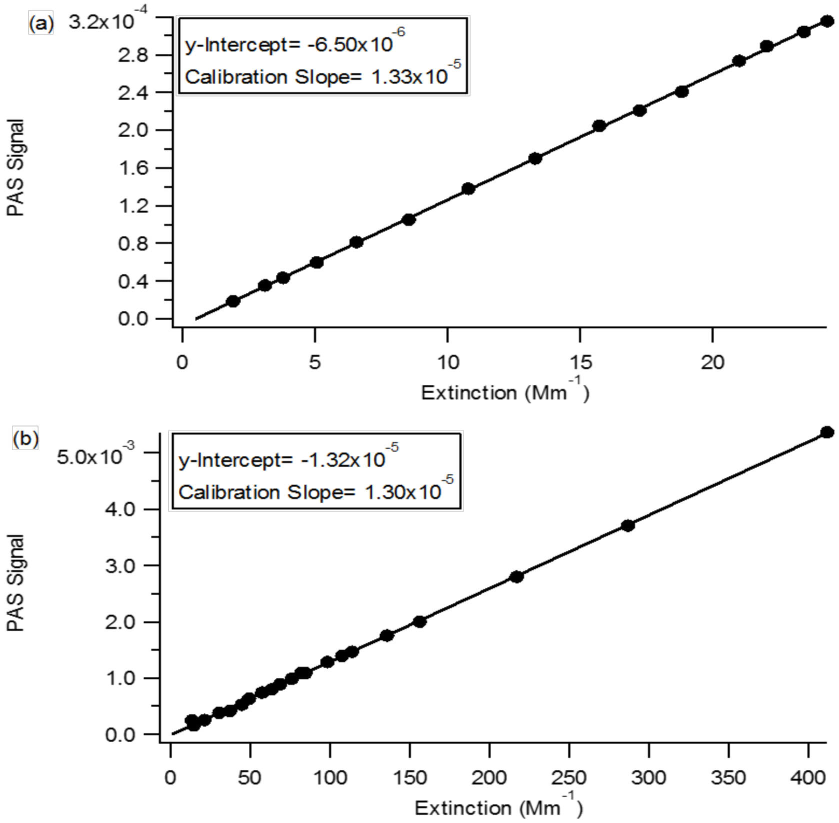

Figure 2.6: Photoacoustic signal versus extinction using ozone as the calibration standard for (a) 405 and (b) 532 nm PASCaRD channels. The slope of the fit line is the calibration factor used to convert the PAS signal into an absorption measurement (Mm^{-1}).

information can be obtained, including the extinction and absorption cross sections (σ_{ext} and σ_{abs}, cm^2), where $\sigma_{ext} = b_{ext}$/N and $\sigma_{abs} = b_{abs}$/N. In addition, the particle extinction and absorption efficiencies (Q_{ext} and Q_{abs}) are found by ratioing the particle extinction and absorption cross sections, respectively, to the particle geometric cross section, πD^2/4, where D is particle diameter measured by the DMA. Thus, $Q_{ext} = \frac{4\sigma_{ext}}{\pi D^2}$ and $Q_{abs} = \frac{4\sigma_{abs}}{\pi D^2}$.

Haze particles within the 170 to 320 nm mobility diameter size range were chosen for the refractive index retrievals since they are much larger than the mode mobility diameters of photochemical and spark discharge generated particles synthesized in this study's setup (Hörst and Tolbert, 2013; Ugelow et al., 2018). Using larger sized particles compared to the mode mobility diameter reduces the influence of doubly-charged particles that result from the DMA size selection process. Despite the precaution of using larger sized particles, a small percentage of doubly-charged particles do make it into the PASCaRD measurements (between < 1 and < 7 % at each particle size selected, calculated based on Wiedensohler (1988)), requiring a correction. The correction for b_{ext} has been detailed previously for CaRD-only retrievals (Hasenkopf et al., 2010; Zarzana et al., 2012), and to correct b_{abs}, a similar method is used.

For each particle mobility diameter, the fraction of singly and doubly charged particles (f_1 and f_2) is calculated based on Wiedensohler (1988) and the number concentration N of the sized particles. The extinction and absorption efficiencies, Q_{ext} and Q_{abs} respectively, which depend on n, k, wavelength (λ) and particle mobility diameter (D), for both singly and doubly charged particles are calculated using a Mie code written in Igor Pro 6.3 (WaveMetrics, Lake Oswego, OR, USA) based on the Fortran code from Bohren and Huffman (2004). Then, the calculated b_{ext} and b_{abs} is given by the sum of contributions from singly and doubly charged particles as

$$b_{ext,calc} = \frac{f_1 N Q_{ext}(n,k,\lambda,D_1)\pi D_1^2}{4} + \frac{f_2 N Q_{ext}(n,k,\lambda,D_2)\pi D_2^2}{4} \tag{2}$$

$$b_{abs,calc} = \frac{f_1 N Q_{abs}(n,k,\lambda,D_1)\pi D_1^2}{4} + \frac{f_2 N Q_{abs}(n,k,\lambda,D_2)\pi D_2^2}{4}, \tag{3}$$

where the mobility diameter of the doubly-charged particles, D_2, is calculated from the mobility diameter of the singly-charged particles, D_1, as explained by Hasenkopf et al. (2010).

The calculated corrected extinctions and absorptions ($b_{ext,calc}$ and $b_{abs,calc}$, respectively) are then compared to the experimentally-retrieved extinctions and absorptions ($b_{ext,exp}$ and $b_{abs,exp}$, respectively) simultaneously through the following merit function (MF) from Zarzana et al. (2014):

$$MF_{CRD+PAS} = \frac{1}{N_d}\sum_{i=1}^{N_d}\frac{(b_{ext,exp} - b_{ext,calc})^2}{b_{ext,exp}^2} + \frac{1}{N_d}\sum_{i=1}^{N_d}\frac{(b_{abs,exp} - b_{abs,calc})^2}{b_{abs,exp}^2} \tag{4}$$

Here N_d is the number of particle sizes used in the retrieval. The goal is to calculate a combination of $b_{ext,calc}$ and $b_{abs,calc}$ that minimizes the merit function. The n and k values that result in the minimization are the best estimates of the real and imaginary refractive indices for the particle population.

Previous work using CaRD alone retrieved the complex refractive index of haze produced by an ultraviolet energy source (Hasenkopf et al., 2010). While there is high precision in the retrieved n value from CaRD alone, there is large uncertainty in the retrieved k value. The extinction efficiency, Q_{ext}, is not very sensitive to small changes in the low k values observed for haze. Therefore, without having a measurement for Q_{abs} from the PAS data, there is no information to constrain the k value, and high uncertainty in k is a commonly observed result.

Further evidence of the inability to determine a precise, and in some cases accurate, n and k when using CaRD alone is the range of k values retrieved for ammonium sulfate in refractive index studies that use only CaRD. Ammonium sulfate is a purely scattering molecule and therefore $k = 0$. However, many studies that use CaRD alone to retrieve the complex refractive index for ammonium sulfate report retrieving a $k > 0$, with k values ranging between 0.002 and 0.01 (Hasenkopf et al., 2010; Lang-Yona et al., 2009; Riziq et al., 2007).

2.4.1 Refractive Index Retrieval Validation

To ensure that both PASCaRD channels, $\lambda = 405$ nm and $\lambda = 532$ nm, retrieve refractive indices correctly, standards commonly used in complex refractive index studies were tested at these two wavelengths. One of the standards used was a purely scattering aerosol, ammonium sulfate (Sigma Aldrich, $\geq 99.0\%$), and the other standard was a strongly absorbing species, nigrosin dye (Sigma Aldrich). Aerosol was produced from aqueous solutions using HPLC grade water. The ammonium sulfate solutions were 0.1 wt.% and the nigrosin dye solutions were 0.05 wt.%. Solutions were atomized (TSI, 3076) using prepurified nitrogen as the carrier gas. The atomized aerosol then flowed through two diffusion driers (TSI, 3062) and two custom-made 4 L Erlenmeyer flask driers to ensure a relative humidity $< 10\%$. Once dried, the particles were sized-selected and flowed through the PASCaRD setup as described in Chapter 2.4.

For the standards, extinction and absorption measurements were retrieved using three to six particle sizes ranging from 245 nm to 445 nm in mobility diameter. The mobility diameters selected for the standards, along with the number of mobility diameters included in the calculations, are based on the size distributions of the ammonium sulfate and nigrosin dye particles from Hasenkopf et al. (2010) and the PASCaRD sensitivity study by Zarzana et al. (2014), respectively. Figures 2.7a and 2.7b show the Q_{ext} and Q_{abs} as a function of particle mobility diameter for ammonium sulfate at $\lambda = 405$ and 532 nm, respectively, and Figure 2.7c and 2.7d show the Q_{ext} and Q_{abs} as a function of particle mobility diameter for nigrosin dye at $\lambda = 405$ and 532 nm, respectively. The points are the values from experimentally-retrieved data and the lines are the fits of the data using the n and k values determined by the minimization of Equation 4.

For ammonium sulfate, the refractive index retrieved at $\lambda = 405$ nm is $n = 1.53 \pm 0.01$

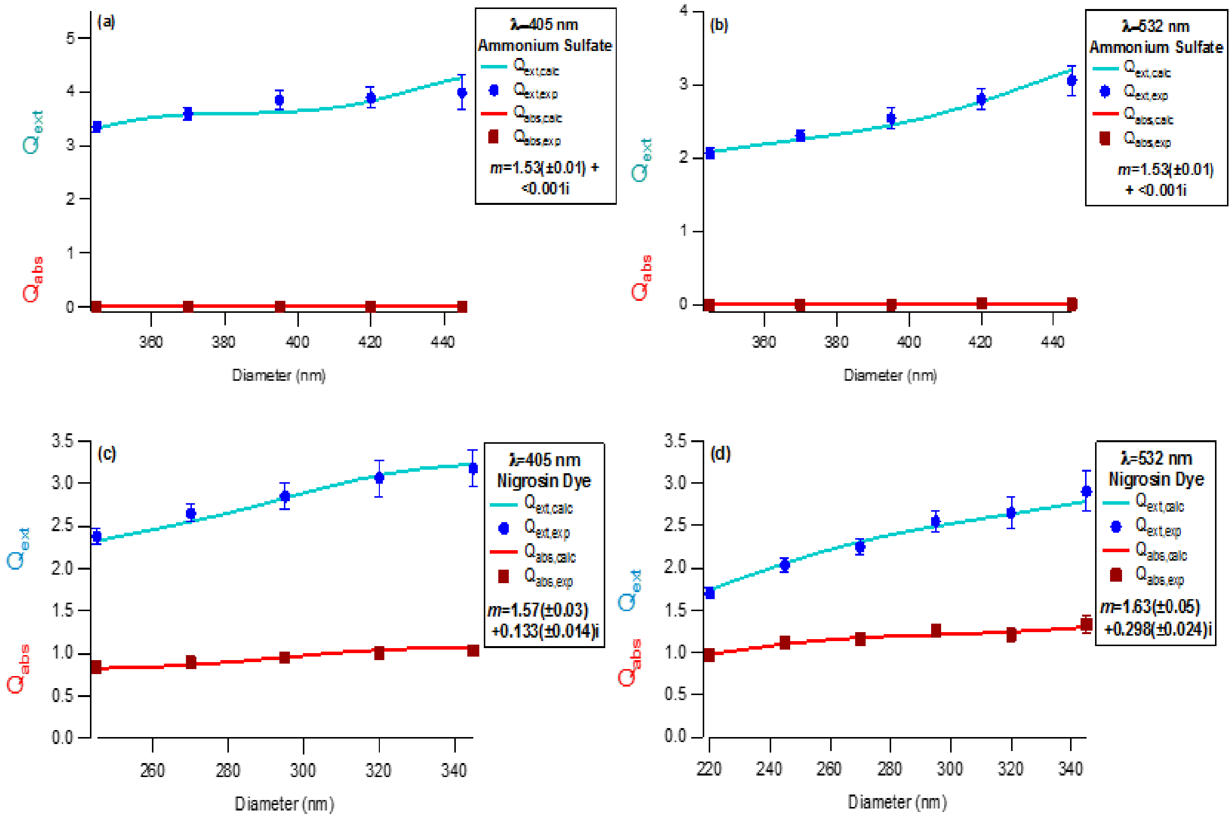

Figure 2.7: Extinction efficiency (Q_{ext}) and absorption efficiency (Q_{abs}) versus particle mobility diameter for ammonium sulfate particles at (a) $\lambda = 405$ nm and (b) $\lambda = 532$ nm and nigrosin dye at (c) $\lambda = 405$ nm and (d) $\lambda = 532$ nm. The points represent the experimental data and the lines represent the calculated Q_{ext} and Q_{abs} using the n and k that result in the minimization of the merit function. Uncertainty in these retrievals includes measurement uncertainty (1σ standard deviation) and retrieval reproducibility (1σ standard deviation), and reflects the limit of detection of the PAS.

and $k < 0.001$, and the refractive index retrieved at $\lambda = 532$ nm is $n = 1.53 \pm 0.01$ and $k < 0.001$. The uncertainties include extinction and absorption measurement uncertainty (1σ), and retrieval reproducibility (1σ), and reflect the inability of the PAS to retrieve a k beyond three decimal places ($k < 0.001$). Both of these retrieved refractive indices agree with the literature, where Toon et al. (1976) retrieves a refractive index of $n = 1.53$-1.55 and $k = 1$ x 10^{-7} at 405 nm and $n = 1.52$-1.55 and $k = 1$ x 10^{-7} at 532 nm. This result highlights the abilities of PASCaRD in determining the real part of the complex refractive index of purely scattering aerosols, while not overestimating the k value.

For nigrosin dye, the refractive index retrieved at $\lambda = 405$ nm is $n = 1.57 \pm 0.03$ and $k = 0.133 \pm 0.014$, and the refractive index retrieved at $\lambda = 532$ nm is $n = 1.63 \pm 0.05$ and $k = 0.298 \pm 0.024$. The uncertainties for these values also include extinction and absorption measurement uncertainty (1σ) and retrieval reproducibility (1σ). Many studies have determined the refractive index of nigrosin dye at $\lambda = 532$ nm (Dinar et al., 2008; Hasenkopf et al., 2010; Lack et al., 2006; Lang-Yona et al., 2009; Riziq et al., 2007) and one study has determined the refractive index of nigrosin dye at $\lambda = 405$ nm (Washenfelder et al., 2013). Amongst the 532 nm studies, there is a wide range of refractive indices retrieved for nigrosin dye, with especially great variation in the real refractive index ($n = 1.63$-1.75). A possible reason for the differences in the retrieved refractive indices of nigrosin dye could be that nigrosin dye is not a pure molecule itself but a mixture of dyes (Hasenkopf et al., 2010). Since it absorbs strongly, it is customary to use it as an absorbing standard, even though it may not be a true standard (i.e. its composition may vary between samples used in different studies). Figures 2.8a and 2.8b compare the imaginary refractive indices of this study and the literature studies at $\lambda = 405$ and 532 nm, respectively. At both wavelengths, the k values retrieved in this study are in good agreement with the literature values.

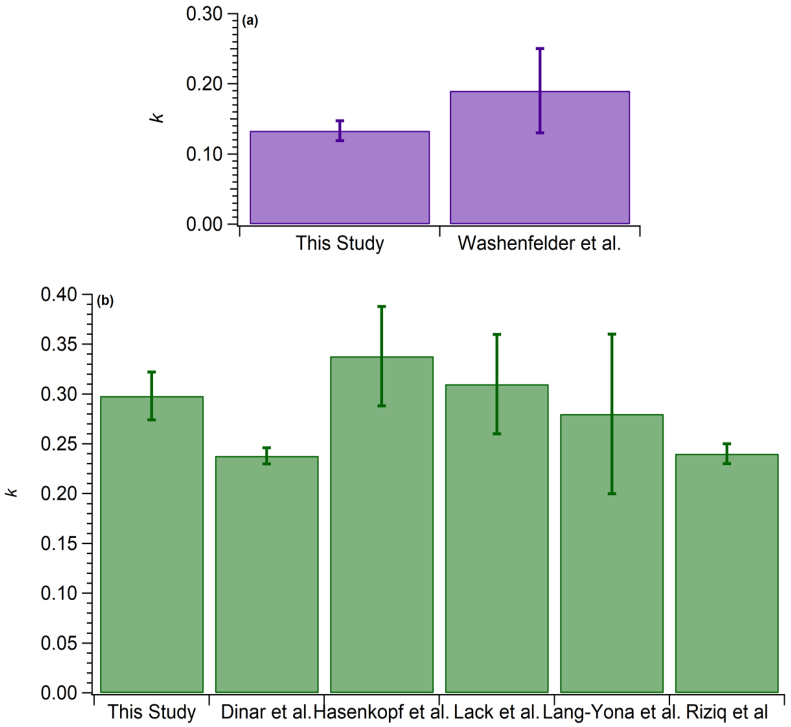

Figure 2.8: The imaginary refractive index of nigrosin dye is compared to the literature imaginary refractive index values at (a) $\lambda = 405$ nm and (b) $\lambda = 532$ nm. The values retrieved here are within error of most previous studies, and error bars in this study include measurement uncertainty (1σ standard deviation) and retrieval reproducibility (1σ standard deviation).

2.5 Aerosol Mass Spectrometry

Aerosol mass spectrometry (AMS; Aerodyne Research, Inc., Billerica, MA) has been used in the Tolbert laboratory previously to determine planetary haze particle composition and particle size (Trainer et al., 2004, 2006, 2012, 2013; DeWitt et al., 2009; Hörst and Tolbert, 2013; Hicks et al., 2015, 2016; Ugelow et al., 2017; Hörst et al., 2018b). By connecting the haze particle generation flow system to the AMS directly, haze particle composition and size information can be measured in-situ without exposing the particles to room air. A schematic of the AMS (Jayne et al., 2000) used in the studies described in Chapter 3 and 4 is shown in Figure 2.9.

Particles and gas enter the AMS through an inlet containing a 120 μm diameter critical orifice. The critical orifice opening restricts the flow into the AMS and reduces the pressure from ambient pressure to about 2.5 Torr. Then the particles are focused into a $\sim$1 mm beam by an aerodynamic lens while differential pumping removes the gas. The aerodynamic lens consists of six apertures with decreasing diameters and transmits particles with diameters between 20 and 1000 nm. However, the collection efficiency drops off steeply for particles with diameters < 60 nm and diameters > 400 nm. At the lens exit, a turbomolecular pump drops the pressure to $< 10^{-3}$ Torr, causing the particles to achieve supersonic expansion and enter the time-of-flight (ToF) chamber once passed the chopper.

The chopper operates in two ways based on the mode of the mass spectrometer. In particle time-of-flight mode (PToF), the chopper, with radial slits, spins continuously. This allows the expanded particle beam to pass through the chopper to the ToF chamber only when the radial slits are in the particle beam's path ("beam chopped"), packetizing the particle transmission and setting a time = 0 for the PToF measurements. In the ToF chamber, the particles travel to the detector at a size-dependent velocity. The size-dependent velocity can then be used to calculate the particle vacuum aerodynamic diameter (d_{va}; the diameter of a unit density sphere that will reach the same terminal velocity in vacuum as the particle of interest) (Jimenez et al., 2003). The AMS is size-calibrated using polystyrene

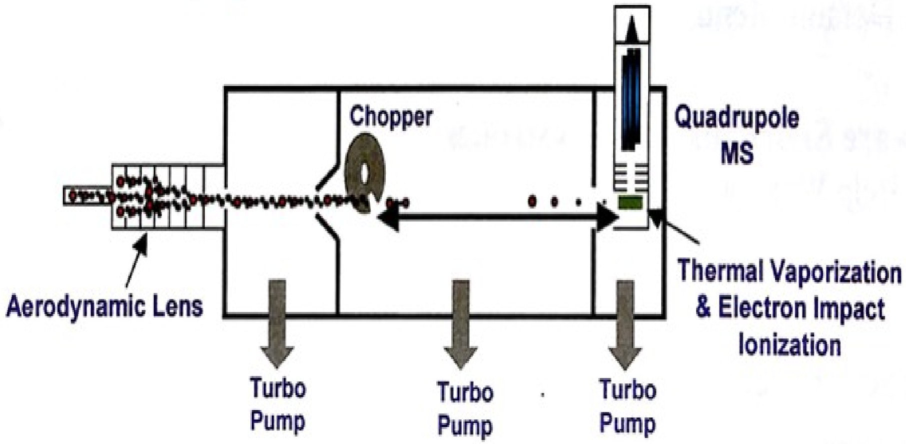

Figure 2.9: Particles are focused into a beam by the aerodynamic lens while the gas is removed by differential pumping. The particles then go into the time-of-flight (ToF) chamber by either passing through the chopper in the "open" position (MS mode) or through the chopper radial slit (PToF Mode). In MS mode, the particles are flash vaporized and ionized by electron ionization, and then mass analyzed by quadrupole mass spectrometry. In PToF mode, the particle's vacuum aerodynamic diameter is measured based on the particle's size-dependent velocity through the ToF chamber

latex spheres to ensure accurate ToF measurements.

In mass spectrum (MS) mode, the chopper moves into ("beam closed") and out of ("beam open") the particle beam, blocking the particle beam entirely and then continuously letting the particle beam pass to the ToF chamber, respectively. Then the focused particle beam is flash vaporized at 600 °C under high vacuum and ionized by electron ionization (70 eV). Quadrupole mass spectrometry (QMA 410, Balzers, Liechtenstein) is used to analyze the ions with unit mass resolution.

Separating the ions that are observed from MS analysis of the haze particles in this study into elemental formulae is not possible due to the low resolution of the Q-AMS. However, an elemental analysis method developed by Hicks et al. (2015) that combines the isotopic labeling of precursor gases and unit resolution AMS was used to quantify the percent of carbon, nitrogen and hydrogen by mass in the haze particles produced during the study detailed in Chapter 3.

When producing particles that contain carbon, isotopically labeling the precursor gas carbon with ^{13}C will cause the mass spectrum to shift to higher *m/z*. Each ion group n, where n= 1, 2, 3..., is defined by the bounds $\mathrm{C_n}$ to $\mathrm{CN_{n-1}H_{n+3}}$, and represents the number of heavy atoms in the ion group. The signal-weighted average mass of each ion group n, ${}^{n}\bar{x}_A$, where A is the isotope of carbon used (i.e. 12 or 13), is calculated as ${}^{n}\bar{x}_A=\frac{\Sigma_i s_i m_i}{\Sigma_i s_i}$. Here s_i is the signal intensity at mass m_i. By comparing the signal-weighted average masses of the ion groups for the labeled and unlabeled particles, the weight percent of carbon, nitrogen and hydrogen in the particles can be quantified (Hicks et al., 2015). Calibration factors are also included in the AMS methods based on Aiken et al. (2008) to account for slight deficiencies in hydrogen detection since $\mathrm{H^+}$ is undetectable.

2.6 Particle Effective Density Calculation

By using the particle diameters measured by the AMS, d_{va}, and the SMPS, d_m, particle effective density (ρ_{eff}) can be calculated. The relationship is shown by DeCarlo et al. (2004)

as:

$$\rho_{eff} = \frac{d_{va}}{d_m}\rho_0 = \rho_m S \tag{5}$$

Here ρ_0 is unit density (1 g cm^3), ρ_m is the particle material density and S is the Jayne shape factor. Therefore, particle effective density depends on particle shape and internal structure, in addition to particle composition. For spherical particles with no internal voids, $S = 1$ and $\rho_{eff} = \rho_m$.

For the study detailed in Chapter 4, the haze particles were flowed alternately to the AMS and the SMPS for size measurements due to flow rate constraints. So while size measurements were not done simultaneously on the same particle population, to ensure an accurate comparison, the stainless steel tubing from the reaction cell to each instrument was the same. The additional tubing to the instrument entry was measured to be identical in length, as well. Other considerations to ensure an accurate comparison include calculating the effective density from AMS and SMPS size data that were measured on the same day using the same precursor gas mixture, and making a new precursor gas mixture for each day that measurements were taken.

2.7 Gas Chromatography Mass Spectrometry

During the study detailed in Chapter 6, the consumption of CH_4 and the presence of secondary gas-phase products were monitored during haze formation as a function of reaction time by a Thermo Scientific Trace 1310 Gas Chromatograph coupled to a Thermo Scientific ISQ QD single quadrupole mass spectrometer (GC-MS). The gas-phase species were extracted from the gas sampling port shown in Figure 2.3 using gas-tight syringes and were injected into the GC-MS. The column used was a Restek Rt-Q-Bond PLOT column, which is optimized for hydrocarbon and carbon dioxide analysis. The GC inlet temperature was 100°C and the temperature program used is shown in Figure 2.10.

Mass spectra were analyzed using Thermo Scientific XCalibur Software. To determine

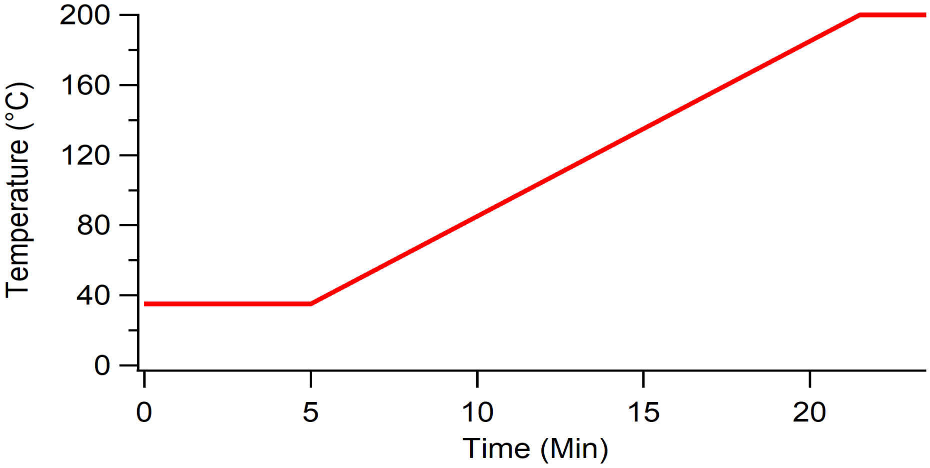

Figure 2.10: GC temperature program for GC-MS measurements

the retention time that corresponded to each gas, the NIST database for electron ionization mass spectra was used. Alkane concentrations were determined based on a standard (Scott Gas, 303102) that contained 64% methane, 12.5% ethane, 7% propane, 3% n-butane, 3% isobutane, 0.5% n-pentane, 0.5% isopentane, 0.5% carbon dioxide and 9% nitrogen. The standard was diluted by 1/100 in a nitrogen background. To calculate the alkane concentrations during the recirculation experiments, the peak areas measured in the 1/100 diluted standard were compared as a direct proportion to the peak areas of the measured gases during the recirculation experiments. Nitriles and acetylene have not yet been quantified but will be quantified once a nitrile and acetylene standard is available.

3 The Optical and Chemical Properties of Discharge Generated Organic Haze Using In-Situ Real-Time Techniques

3.1 Introduction

Because the Descent Imager/Spectral Radiometer (DISR) on the Huygens Probe has shown that haze exists throughout Titan's atmosphere (Tomasko et al., 2005), it is important to understand the optical and chemical properties of the haze since its abundance has major implications for other atmospheric and surface properties, like the radiative balance (McKay et al., 1989, 1991) and surface albedos (Griffith et al., 2003, 2012; Hirtzig et al., 2013; Negr*ão* et al., 2006). In order to calculate or model many of these impacts, knowledge of the complex refractive index of the haze, m, is required. The complex refractive index is defined as $m=n+k\mathrm{i}$, where the real part, n, describes scattering, and the imaginary part, k, describes absorption. Ideally, measurements of chemical composition would accompany the complex refractive index retrievals since chemical composition fundamentally determines how the haze will interact with light. A review by Brass*é* et al. (2015) provides an in depth analysis of previous work on haze analog complex refractive indices.

The most comprehensive study of haze particle optical constants that included a wide range of wavelengths is reported in Khare et al. (1984). In that study, haze was produced by the direct current (DC) electrical discharge of 10% CH_4 in N_2 and was collected on a substrate. The optical constants of the haze particles over a wide wavelength range were determined by the combination of transmittance, reflectance, interference, ellipsometric polarization and Brewster angle measurements. The cold plasma energy source, the collection of haze produced from gas mixtures of CH_4 and N_2 on a substrate and the spectrophotometric and ellipsometric methods used by Khare et al. (1984) are similar to the experimental procedures and methods used by most studies that determined the full complex refractive index of haze analogs decades later (Imanaka et al., 2012; Mahjoub et al., 2012; Ramirez et al., 2002; Sciamma-O'Brien et al., 2012, Studies that report only the imaginary refractive index are not referenced).

Studies that differ from Khare et al. (1984) include Khare et al. (1987), Tran et al. (2003) and Hasenkopf et al. (2010). While Khare et al. (1987) used similar experimental methods as Khare et al. (1984), they produced haze from various combinations of methane, hydrogen and helium. Additionally, both Tran et al. (2003) and Hasenkopf et al. (2010) used ultraviolet excitation to produce haze. Tran et al. (2003) irradiated methane and nitrogen mixtures that included hydrogen, acetylene, ethylene and cyanoacetylene using wavelengths at 185 and 254 nm. Hasenkopf et al. (2010) produced haze from Lyman-α excitation of methane and nitrogen and used cavity ring-down spectroscopy to determine the haze optical constants. Cavity ring-down spectroscopy allows for the measurement of the complex refractive index in situ on freely flowing aerosol. However, that study was performed only at 532 nm.

Despite the many studies that have determined the optical constants of haze particles produced from methane and nitrogen, there is still great variation in the reported k values. Experimental differences resulting in different k values, such as initial gas mixture compositions, energy source (including temperature changes resulting from the energy source) and pressure during haze formation, have been discussed in detail by Sciamma-O'Brien et al. (2012). And while most haze particle optical constant studies have synthesized haze at room temperature, a study by Mahjoub et al. (2014) has shown that the complex refractive indices of hazes are different when produced in a colder environment. Hazes that were produced at 105 K had higher n values and lower k values than the hazes produced at 300 K (Mahjoub et al., 2014). Further, experiments that use the same energy source and experimental setup can measure different imaginary refractive index values by simply changing the type of substrate used to collect the haze particles (Mahjoub et al., 2012; Sciamma-O'Brien et al., 2012). Substrates' electric properties can influence the flux of the energy source used to produce haze (Mahjoub et al., 2012), possibly impacting the chemical properties of the particles.

In addition to the variation in the imaginary refractive index of these hazes between studies, there is also high uncertainty in the reported k values in the visible and ultraviolet wavelength range (at least 30% uncertainty) (Hasenkopf et al., 2010; Khare et al., 1984; Ramirez et al., 2002), which can result from experimental effects like the retrieval method used (Hasenkopf et al., 2010), nonuniform film thickness and aerosol porosity (Ramirez et al., 2002), and sample variations (Khare et al., 1984). Imanaka et al. (2012) reports an uncertainty of $< 10\%$ in their haze particle k values, but that experiment focused on the infrared range, solving for complex refractive indices between 2.5 and 25 μm. Having precise k values are important for understanding the radiative forcing of an aerosol (Zarzana et al., 2014). Zarzana et al. (2014) show that even small uncertainties in k can exacerbate radiative forcing uncertainties, where they show that a 150 nm sized particle with an uncertainty of $\pm$ 0.01 in k can result in approximately $\pm$ 20% uncertainty in forcing.

Although there is variation and high uncertainty in the optical constants of haze particles, many planetary studies use the complex refractive indices of the particles produced by Khare et al. (1984) in data retrieval programs and algorithms to calculate other parameters, including the single-scattering albedo of Titan aerosol (Tomasko et al., 2005, 2008). In addition to Titan studies, ancient Earth studies have used the optical constants determined by Khare et al. (1984) to study the impact of potential haze on the paleoclimate (Sagan and Chyba, 1997; Pavlov et al., 2001; Domagal-Goldman et al., 2008; Haqq-Misra et al., 2008; Wolf and Toon, 2010; Arney et al., 2016). Even some past studies of Pluto and Jupiter have used the optical constants from Khare et al. (1984) in their atmospheric models (Grundy and Buie, 2001; Irwin et al., 1998).

In the study presented here, three different hazes have been produced with a spark discharge source using 0.1, 2 and 10% by volume methane in nitrogen. These specific concentrations of CH_4 have been chosen in order to study the optical and chemical properties of haze analogs produced with a concentration of CH_4 covering two orders of magnitude. The first two concentrations, 0.1 and 2% CH_4, were included because they are at the peak aerosol production rate for this study's experimental setup using the UV (Trainer et al., 2006) and spark discharge (Hörst and Tolbert, 2013) energy sources, respectively. In addition, 10% CH_4 was also included in this study as a point of comparison since it is a common precursor methane concentration used in previous organic haze analog studies that determine the complex refractive index of haze analogs produced by methane in nitrogen only (Khare et al., 1984; Imanaka et al., 2004, 2012; Mahjoub et al., 2012).

The resulting particles were produced in a flow system, and their compositions were determined in situ using quadrupole aerosol mass spectrometry (Q-AMS) with the aid of isotopically labeled precursor gas. The complex refractive indices at wavelengths of 405 and 532 nm were determined in situ using photoacoustic spectroscopy coupled to cavity ring-down spectroscopy (PASCaRD). The addition of photoacoustic spectroscopy to the optical measurements allows for the direct measurement of particle absorption, which can enhance precision and accuracy in the imaginary refractive index term k. While photoacoustic spectroscopy and cavity ring-down spectroscopy have been used together before in studies of the optical properties of Earth aerosol (Atkinson et al., 2015; Cappa et al., 2016; Lack et al., 2006, 2012a,b; Lambe et al., 2013; Radney et al., 2013, 2014; Zarzana, 2014.; Zhang et al., 2016), this is the first study that uses this technique for planetary haze analogs. Like previous work by Imanaka et al. (2004) and Mahjoub et al. (2012), this study will use the chemical properties of haze analogs formed under different experimental conditions to help explain their optical properties.

3.2 Results and Discussion

3.2.1 Haze Particle Refractive Index Retrievals

Figures 3.1a and 3.1b illustrate examples of the Q_{ext} and Q_{abs} at 405 and 532 nm, respectively, determined from experimentally-retrieved data for haze particles produced with 0.1, 2 and 10% CH_4 in N_2 using the PASCaRD setup described in Chapter 2.4. Also shown are the calculated Q_{ext} and Q_{abs} values as a function of particle size using the best fit n and k

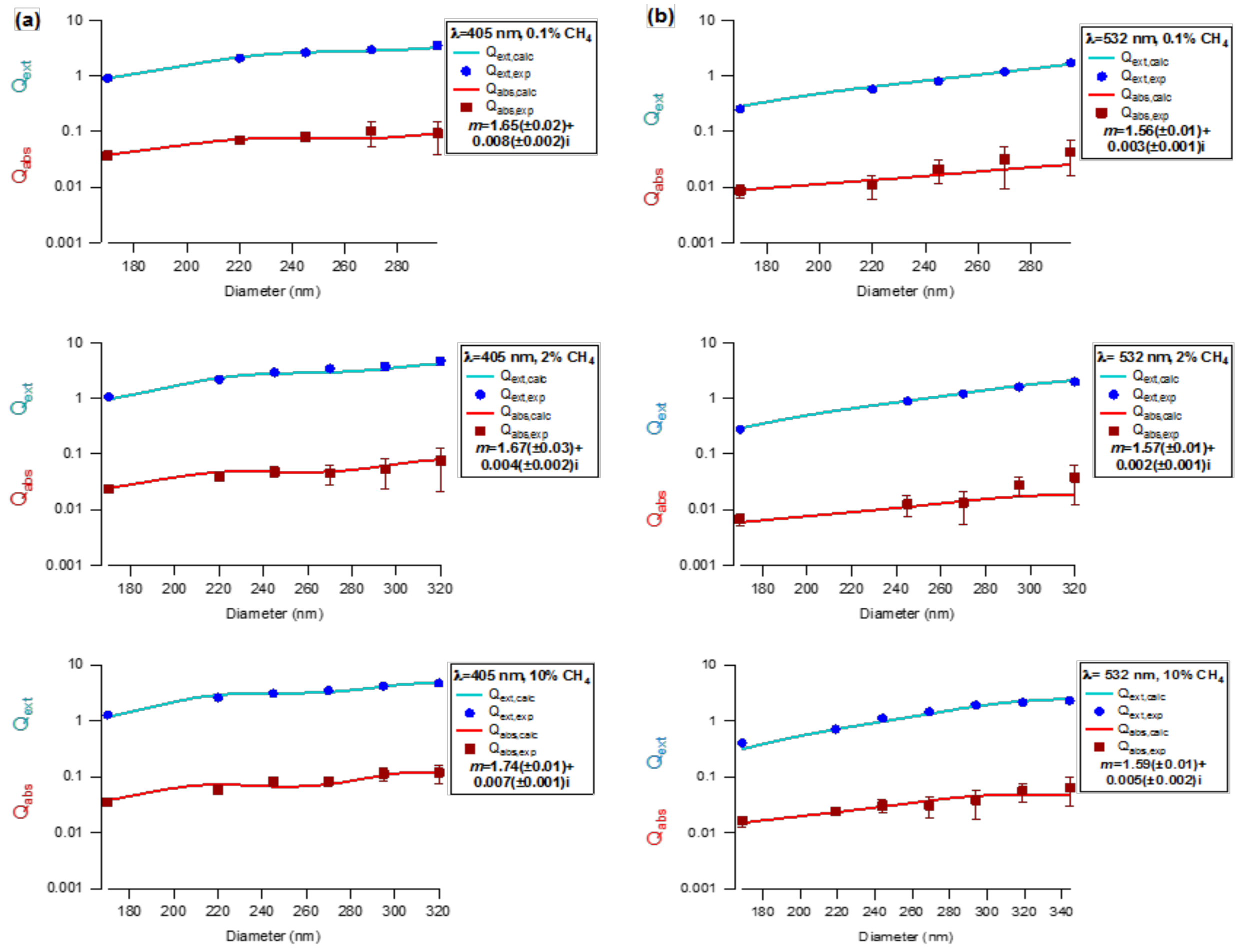

Figure 3.1: Extinction efficiency (Q_{ext}) and absorption efficiency (Q_{abs}) versus particle mobility diameter for haze particles produced with 0.1, 2 and 10% CH_4 at (a) $\lambda = 405$ nm and (b) $\lambda = 532$ nm. The points represent the experimental data and the lines represent the calculated Q_{ext} and Q_{abs} using the n and k that result in the minimization of the merit function. These n and k values for the above retrievals are included in both figures and the uncertainty includes the 1σ standard deviation of the extinction and absorption measurements at each particle mobility diameter. The y-axes on these figures have been put into a log scale in order to see the Q_{abs} fit more clearly.

calculated by the method described in Chapter 2.4. The uncertainties for these individual retrievals include extinction and absorption measurement uncertainties. Here, the optical constants fit the experimental Q_{ext} and Q_{abs} data very well, even when the Q_{abs} values are very small.

Retrieved refractive indices at both wavelengths for all the hazes studied are shown in Table 3.1. The uncertainties for each refractive index term is based on the 1σ standard deviation of the measured extinction and absorption at each particle mobility diameter, and the 1σ standard deviation of the reproducibility of the retrievals. The uncertainties from the measurement techniques are responsible for most of the uncertainties seen in Table 3.1. Percent uncertainties related to experimental reproducibility are $\leq 1.5\%$ in n and $\leq 20\%$ in k. The optical constants of haze retrieved in this study are compared to literature values of haze produced with CH_4 and N_2 only in Figures 3.2a and 3.2b for wavelengths of 405 and 532 nm, respectively. Error bars are included for studies that report uncertainties. Ramirez et al. (2002) determined their uncertainty in a similar manner as this study, whereas other studies report an estimation of uncertainty based on sample variation (Khare et al., 1984) or retrieval reproducibility (Hasenkopf et al., 2010).

Beyond the differences in the complex refractive indices of Khare et al. (1984) and this study, there are other differences in the complex refractive indices retrieved in this study compared to other studies. Despite Hasenkopf et al. (2010) and this study using similar experimental setups, with the major difference being the energy source used to produce haze particles, there is a large difference in the retrieved complex refractive index. While the differences in n are more difficult to explain without knowing the exact molecules that make up the haze particles, the differences in k may be attributed to the greater amount of aromatic molecules in the haze particles produced by UV excitation (Hörst et al., 2018b).

In addition, substrate collection and the environmental pressure at which the hazes are produced are important to consider, as well. All studies in Figure 3.2 except Hasenkopf et al. (2010) and this study collected haze on a substrate. The influence of substrate type used to

	$\lambda = 405$ nm		$\lambda = 532$ nm	
	n	k	n	k
0.1% CH_4	1.66 ± 0.03	0.008 ± 0.002	1.56 ± 0.02	0.003 ± 0.001
2% CH_4	1.68 ± 0.02	0.005 ± 0.001	1.56 ± 0.02	0.002 ± 0.001
10% CH_4	1.71 ± 0.02	0.007 ± 0.002	1.59 ± 0.02	0.005 ± 0.001

Table 3.1: The refractive indices retrieved in this study for haze produced using 0.1, 2 and 10% CH_4. Uncertainties in n and k result from 1σ standard deviations in the extinction and absorption measurements at each particle mobility diameter, along with the 1σ standard deviation of the reproducibility of each retrieval. The uncertainties from the measurement techniques are responsible for most of the uncertainties. The percent uncertainties from experimental reproducibility are $\leq 1.5\%$ in n and $\leq 20\%$ in k.

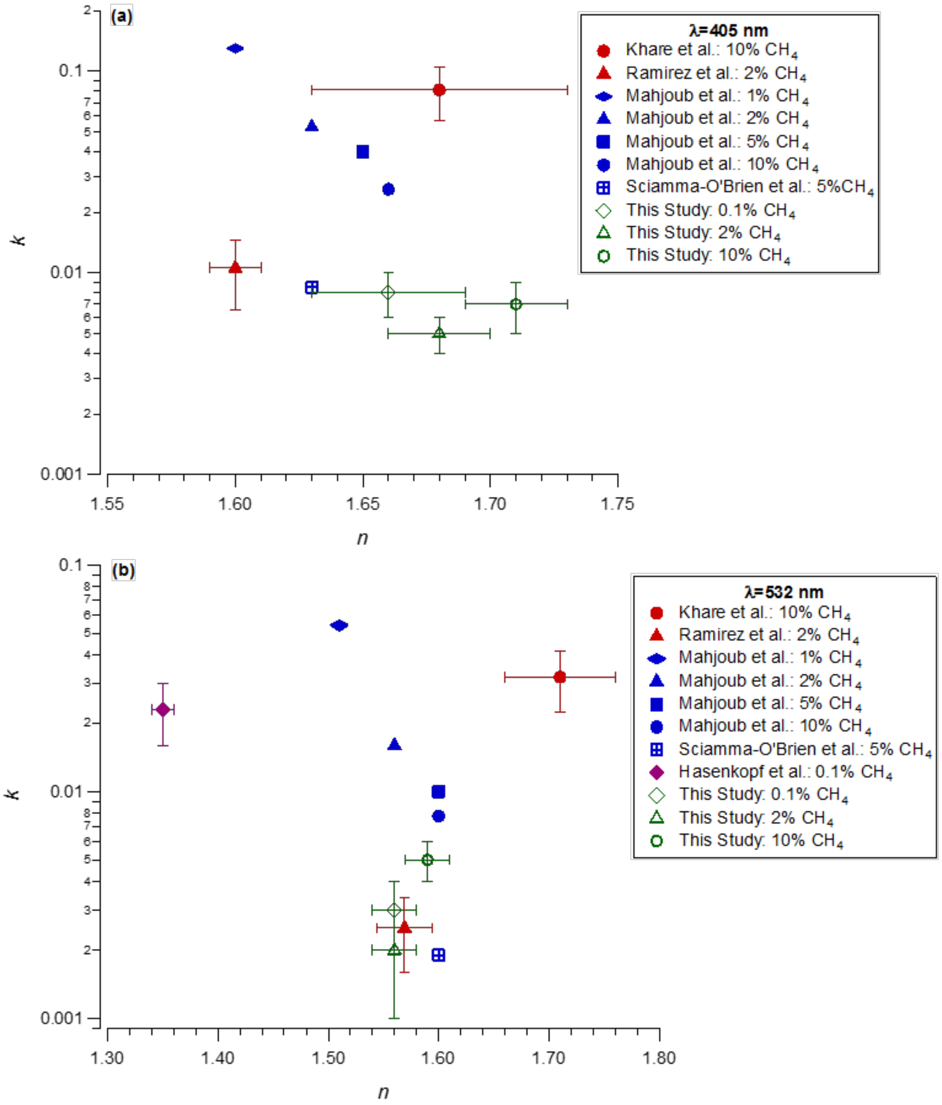

Figure 3.2: Comparison of the complex refractive indices retrieved in this study and those in the literature at (a) $\lambda = 405$ nm and (b) $\lambda = 532$ nm. The literature studies included in this comparison are the studies that only include CH_4 and N_2 in their gas mixtures. Percent CH_4 used in each study is included in the legend and is represented by the shape of the data point. Points with similar colors are values retrieved of hazes produced using the same type of energy source. Red points represent DC discharge, blue points represent capacitively coupled plasma radio frequency (CCP RF) discharge, purple points represent UV lamp with Lyman-α emission and green points represent spark discharge. Linear interpolation has been used for the studies that do not retrieve their complex refractive indices at the exact wavelengths used in this study. Error bars are included for studies that report uncertainties.

collect haze particles can be seen when comparing the studies by Mahjoub et al. (2012) and Sciamma-O'Brien et al. (2012). Both studies use the same energy source and experimental setup as each other, but use different substrates (silicon substrate and Pyrex substrate covered with aluminum and silicon dioxide, respectively) to collect the haze particles, and they retrieve very different optical constants from each other.

Also, the pressure where hazes are produced can influence their k values. Imanaka et al. (2004) showed that for their experimental conditions, varying the environmental pressure over two orders of magnitude resulted in hazes with k values that decreased with increasing pressure. However, no other complex refractive index study has determined the systematic effect of pressure on haze optical constants, and when different studies are compared to each other, there is no exact trend in k based on the pressure at which the hazes were produced. An example of this can be seen between this study, Hasenkopf et al. (2010) and Sciamma-O'Brien et al. (2012), where both this study and Hasenkopf et al. (2010) produced haze particles at about 600 Torr and Sciamma-O'Brien et al. (2012) produced haze particles at a pressure about 3 orders of magnitude lower. Despite the different pressure, at λ =532 nm this study is closer to the k values of Sciamma-O'Brien et al. (2012), with Hasenkopf et al. (2010) retrieving a k value an order of magnitude higher. So while all of these different experimental factors are very important to consider when comparing the differences in the observed k values, it is still difficult to account for all the discrepancies.

For the optical constants retrieved during this study, n at $\lambda = 405$ nm increases with the amount of CH_4 used during haze production, while there is no apparent trend in the n at $\lambda = 532$ nm. The trend of increasing n with increasing CH_4 concentration used during haze production has been previously observed by Mahjoub et al. (2012). They also found that their haze particles uniformly experienced a decreasing k when increasing the CH_4 concentration used during haze production. In contrast, the trend in k in this study is not a positive or negative trend, but a statistically significant V-shaped trend (confidence interval 95%; Table 3.1, Figure 3.2). The k value for both wavelengths initially decreases as the amount of CH_4 used to produce the haze particles increases, and then after 2% CH_4, the k value increases with increasing precursor CH_4.

Because there is such wide variation of n and k values and trends resulting from the many different experimental conditions and analysis methods used, it is difficult to determine which haze is the most "relevant". The impact of using optical constants from one study over another can be seen with the single-scattering albedo ($\tilde{w}$). The single-scattering albedo describes the ratio of light scattered to the total light extinguished by a type of particle, where

$$\tilde{w} = \frac{\sigma_{scat}}{\sigma_{scat} + \sigma_{abs}} \tag{6}$$

and σ_{scat} and σ_{abs} are the scattering and absorption cross sections, respectively. The scattering and the absorption cross sections are calculated from the complex refractive indices using Mie theory. Figures 3.3a and 3.3b show the calculated single-scattering albedo, at $\lambda =$ 405 and 532 nm respectively, for particles with diameters between 10 and 500 nm for the particles produced in this study compared to the single-scattering albedo calculated using the values from Khare et al. (1984). All of the hazes from this study are less absorbing than the haze from Khare et al. (1984). When comparing the particles from this study that were produced with the same amount of CH_4 as the particles from Khare et al. (1984), i.e. 10% CH_4, a particle with a diameter of 100 nm from this study is 1.9 and 1.5 times more scattering at 405 and 532 nm, respectively, than a particle with a diameter of 100 nm from Khare et al. (1984). A similar conclusion about the single-scattering albedo is expected for most of the previous haze optical constant studies from Figure 3.2 that have lower k values than Khare et al. (1984). Therefore, universally using the refractive index values retrieved by Khare et al. (1984) for any type of planetary haze may not be the best solution, and it would be pragmatic for modeling studies to explore the sensitivity of the wide range of different optical constants in the literature on model results.

3.2.2 Elemental Analysis of Haze Particles

Since each type of haze produced in this study has a unique complex refractive index, it suggests that producing haze with different concentrations of CH_4 results in haze with different chemical compositions. To learn more about the chemical properties of the hazes produced, the method developed by Hicks et al. (2015), which combines the Q-AMS and the isotopic labeling of methane gas, briefly described in Chapter 2.5, was used.

Figure 3.4a shows the mass spectrum for each haze produced when carbon is unlabeled and Figure 3.4b shows the mass peaks shifting to higher masses for each haze produced when carbon is isotopically labeled as ^{13}C. The shifted peaks that result in each isotopically-labeled mass spectrum are not exactly the same shape as they were in their respective unlabeled mass spectrum because there is nitrogen in these particles, presumably at variable amounts in different ions, and nitrogen will not shift to higher m/z when carbon alone is isotopically labeled.

Following Hicks et al. (2015), to determine the fraction of carbon, f_C, a plot of $^n\bar{x}_{12}$ and $^n\bar{x}_{13}$ (the signal-weighted mass average at each ion group, n) versus n ion group is made by fitting their slopes, $\bar{x}_{12}$ and $\bar{x}_{13}$, by linear regression through the origin. Examples of these fits for the haze particles in this study are shown in Figure 3.5 The fraction of carbon in the particles in comparison to the other backbone atom results from the difference between the slopes where $f_C = \bar{x}_{13} - \bar{x}_{12}$ since the labeled carbon atoms are responsible for the two different slopes. The fraction of nitrogen, f_N, in the particles can then be calculated as $f_N = 1 - f_C$ since it represents the backbone heavy atom that did not shift in the labeled mass spectrum. Because f_N accounts for the fraction of unlabeled heavy atoms, this method is unable to differentiate between nitrogen and oxygen.

The mass fraction of carbon, nitrogen (and oxygen) and hydrogen (w_C, w_N and w_H, respectively) is found by:

$$w_C = \frac{12 f_C}{\bar{x}_{12}} \tag{7}$$

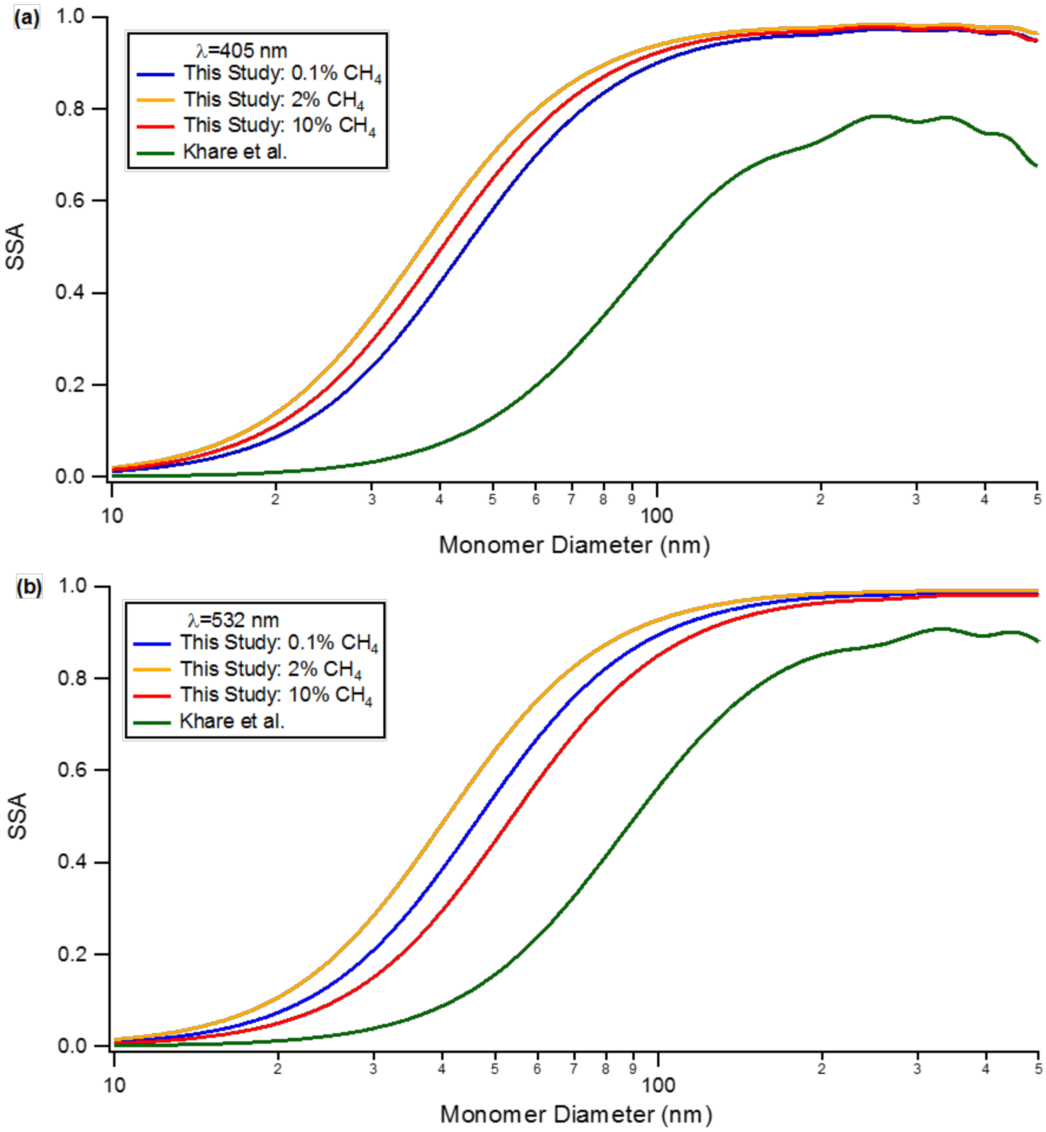

Figure 3.3: Calculated single-scattering albedo for particles between 10 and 500 nm in diameter for the hazes from this study and from Khare et al. (1984) at (a) λ = 405 and (b) λ = 532 nm. Haze particles from this study are uniformly less absorbing than the haze particles from Khare et al. (1984).

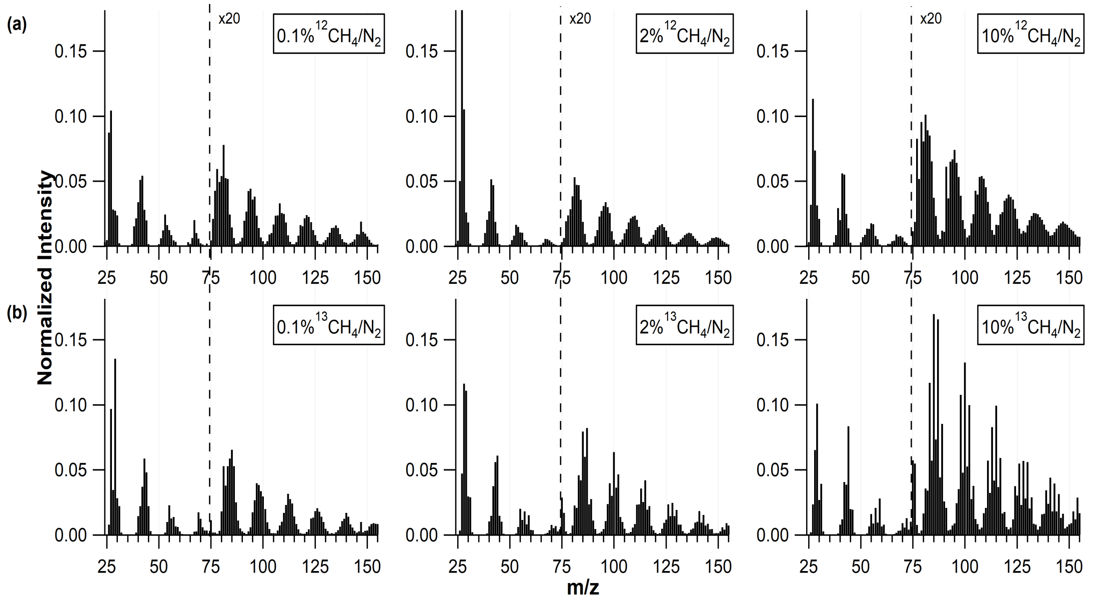

Figure 3.4: Mass spectra normalized to the total mass signal for each haze produced with unlabeled CH_4 (a) and isotopically labeled $^{13}CH_4$ (b). Data for $m/z > 74$ is multiplied by a factor of 20 and gridlines are added to each spectrum for visual aids. Note the movement of peaks to higher m/z for the ^{13}C-labeled spectra.

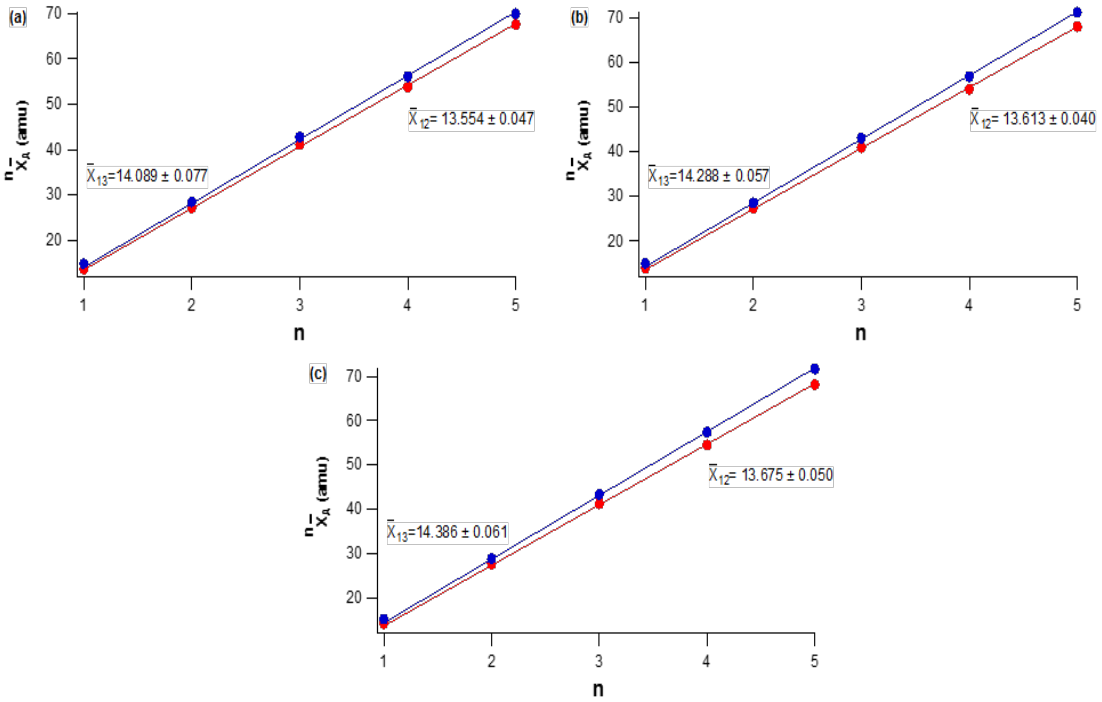

Figure 3.5: The signal-weighted mass average, $^{n}\bar{X}_A$ vs n packet number for particles produced with (a) 0.1, (b) 2 and (c) 10% CH_4. $\bar{X}_{12}$ and $\bar{X}_{13}$ represent the slopes of the fits for the unlabeled and labeled haze particles, respectively.

$$w_N = \frac{14 f_N}{\bar{x}_{12}} \tag{8}$$

$$w_H = \frac{\bar{x}_{12} - 12 f_C - 14 f_N}{\bar{x}_{12}} \tag{9}$$

Uncertainties in the weight percents are calculated in the same manner as described in Hicks et al. (2015).

Figure 3.6 shows the average elemental composition by mass of each type of haze produced in this study. Particles produced with 0.1% CH_4 are composed of 47 ± 8% C, 48 ± 9% N and 5 ± 1% H by mass, particles produced with 2% CH_4 are composed of 59 ± 6% C, 34 ± 7% N and 7 ± 1% H by mass, and particles produced with 10% CH_4 are composed of 66 ± 7% C, 25 ± 8% N and 9 ± 1% H by mass. Uncertainties include experimental reproducibility (1σ). While every experimental system tries to eliminate oxygen, it is very difficult to completely do so in practice. Since there is possible oxygen contamination resulting from water present in the reaction system, the exact oxygen concentration in these particles is unknown because it cannot be constrained with the method of Hicks et al. (2015). Only the fraction of non-isotopically labeled heavy atoms is constrained, which in this study could be both nitrogen and oxygen if there is substantial oxygen contamination. Hicks et al. (2015) report their haze generated by the UV photolysis of 0.1% CH_4 in N_2 to contain 9% O by mass. If the method of oxygen incorporation is independent of energy source, this percent oxygen is expected to be the lower limit of oxygen in this study. Despite a different energy source, most of the experimental setup used in this study is the same as what was used in their study. However, with the addition of pre-purified nitrogen after aerosol production, there is a possibility for another source of oxygen contamination. Therefore, the calculated percent nitrogen should be considered an upper limit.

Figure 3.7 shows the N/C molar ratios in these hazes. Particles synthesized from 0.1% CH_4 have the highest N/C ratio, and as the CH_4 concentration in the initial gas mixture increases, the N/C ratio decreases. Since the amount of oxygen is contained in the mass percent of nitrogen, note that it is very possible that the N/C ratios without the inclusion of oxygen would be lower than what is observed in Figure 3.6. However, the trend in the N/C ratio for each haze is expected to be similar.

3.2.3 Comparison of Haze Optical and Chemical Properties

While the N/C ratio decreases with increasing methane precursor concentration, the imaginary refractive index first decreases and then increases as methane is increased (See Table 3.1). It may be expected that the amount of absorption and the amount of nitrogen in a molecule would be positively correlated due to the potential for nitrogen's lone pair of electrons to contribute to the delocalization of pi electrons in a complex molecule. The effect of nitrogen in haze particles has been previously observed by Mahjoub et al. (2012), who found that their hazes that contained more amine functional groups had higher k values. The increase in haze absorption for the particles produced with the highest CH_4 concentration suggests that other chemical factors, such as conjugation, aromatics and other functional groups, may also be important.

Additional insight into haze particle composition can be found using the ion series ("delta") analysis method to identify functional groups in the molecules that compose the haze particles. Delta analysis originated as an index classification system to determine what class of molecule a mass spectrum belonged to based on the series displacement index (Dromey, 1976). The series displacement index relates the positive shift between the mass fragments present in the mass spectrum to the mass fragments for the alkene series. The use of this method has evolved to being a tool for identification of functional groups present in electron ionization mass spectra, where the delta index for each mass peak, m/z, is calculated as $\Delta = m/z - 14x + 1$ (McLafferty and Tureček, 1993), where x represents the mass peak's packet number defined by visually picking starting and ending points of the packet. The influence of this method in defining x is detailed below. The value of Δ, which corresponds to a type of functional group, is calculated for each peak. The intensity for each Δ number corresponds to the intensity of each peak in the normalized mass spectrum with

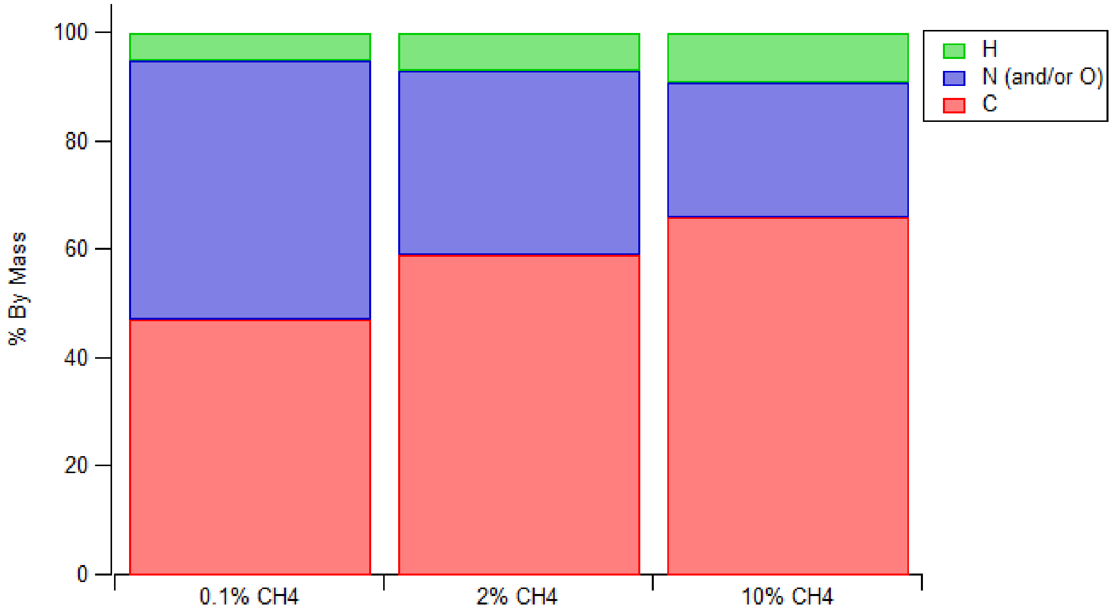

Figure 3.6: Average elemental mass fraction for each haze synthesized in this study. Note the amount of nitrogen and oxygen cannot be differentiated in this method so the percent nitrogen is an upper limit.

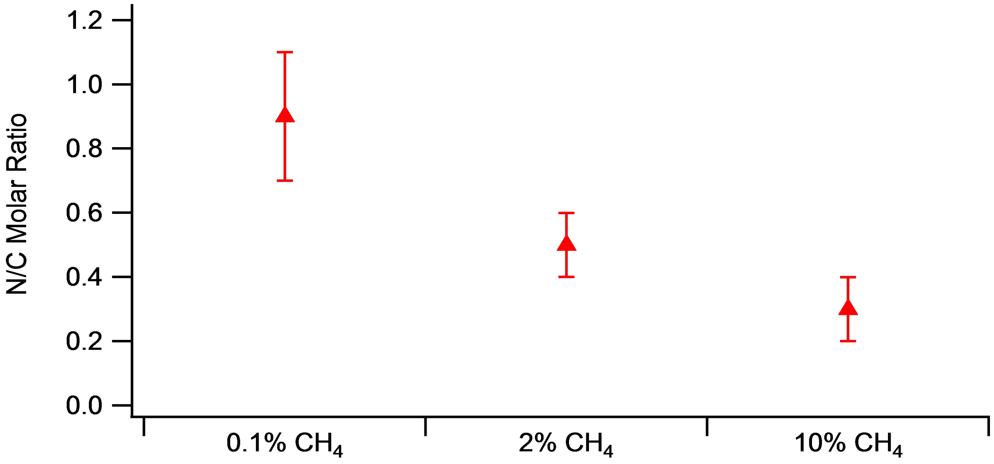

Figure 3.7: N/C molar ratio for each haze produced in this study. As the CH_4 concentration used to produce haze increases, the N/C molar ratio decreases. Note that these exact numbers do not take into account the potential for oxygen contamination. Therefore, these N/C ratios are an upper limit.

that calculated Δ number.

The negative delta index numbers from $\Delta = -8$ to -2 represent mostly aromatic functional groups, although $\Delta = -3$ and -2 can also represent conjugated hydrocarbons. Therefore, $\Delta = -8$ to -4 are solely aromatic functional groups. For the particles in this study, $\Delta = -1$ mostly represents the nitrile functional group (H$\ddot{o}$rst et al., 2018b), but can also represent other conjugated hydrocarbons. As the functional groups become more aliphatic and less conjugated, the delta number becomes more positive. In addition to these hydrocarbons, $\Delta = +1$ and $+3$ possibly include imines and amines, respectively. Moreover, other nitrogen containing functional groups can be included in other Δ numbers as well, for example Δ = -5. At Δ= -5, nitrogen containing aromatics are included, such as pyridyl groups, along with other aromatic groups that do not contain nitrogen. Because of this, obtaining any quantitative information about nitrogen containing species in haze particles from delta analysis is not practical.

The fraction of the haze particle mass loading at each delta index number was calculated using the mass spectrometry data from Figure 3.4a between m/z 12 and 154. Signals at lower m/z are not accurately measured by this instrument due to ion optics limitations. Figure 3.8 shows the results of the delta analysis normalized to 1. Looking at the exclusively aromatic delta numbers ($\Delta = -8$ to -4), Figure 3.9 shows the relationship between k values and the approximate aromatic content in the haze particles (referred to as approximate aromatic content since a portion of the signal at $\Delta = -2$ and -3 can include aromatics, but exact amounts are indeterminable). To test the influence of visually picking starting and ending points of x, the bounds of x were changed by one or two amus. The resulting approximate aromatic content changes by 0.44, 0.22 and 0.36% for the hazes produced with 0.1, 2 and 10% CH_4, respectively, demonstrating that there is little, if any, bias in the method of determining x visually. Based on the extensive literature on AMS analysis of organic species, the aromatic molecules detected had to be present in the particles, and were not formed in the instrument vaporizer. The AMS is known to decompose and fragment

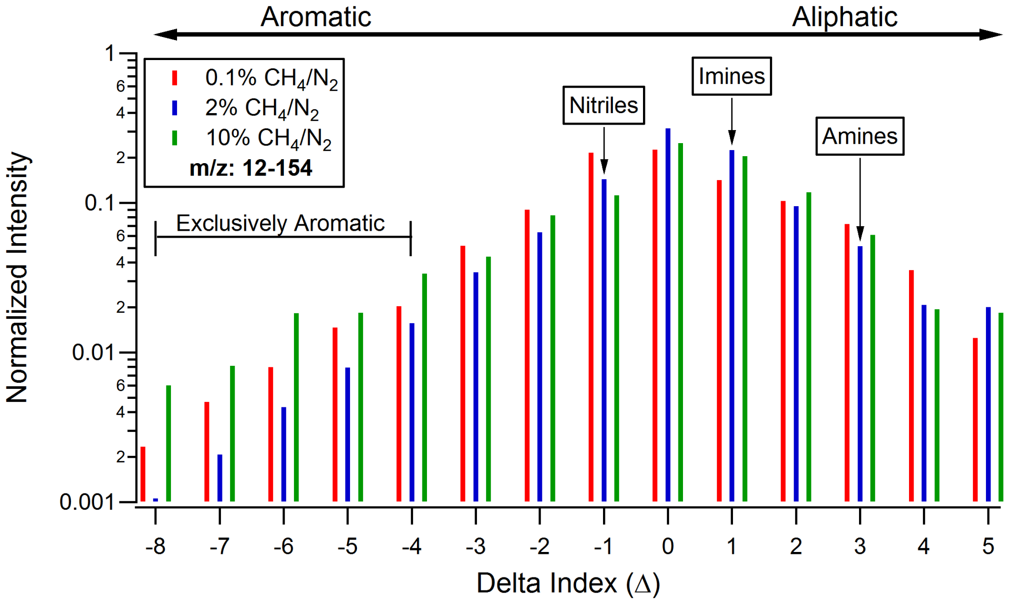

Figure 3.8: The types of functional groups in each haze determined by delta analysis help with understanding the optical properties of each type of haze. Note Δ = -8 to Δ = -4 only represent aromatic functional groups.

the molecules present in the particles, but the formation of large molecular species such as aromatics in substantial amounts has not been reported (e.g. Canagaratna et al., 2007, 2015).

Particles produced from 2% CH_4 have the lowest contribution from $\Delta = -8$ to -4 (aromatics), consistent with the lowest observed k values. On the other hand, particles produced from 10% CH_4 have the highest contribution from functional groups in this region, implying that these particles have the highest aromatic fraction. This could explain why the k values for the haze particles produced from 10% CH_4 are greater than the k values for the haze particles produced from 2% CH_4, despite containing less nitrogen. This result has also been observed by Imanaka et al. (2004), who found haze particles that contained more aromatic features and less aliphatic features had higher k values. Fit lines from linear regression of k versus the % signal at exclusively aromatic delta are shown in Figure 3.9, as well. At $\lambda = 532$ nm, k approaches zero as aromatic signal approaches zero, and in contrast, at $\lambda = 405$ nm, k is greater than zero as aromatic signal approaches zero. This suggests that for the hazes produced in this study, absorption seen at $\lambda = 532$ nm is mostly due to aromatic absorption while the absorption seen at $\lambda = 405$ nm is from other sources in addition to aromatics, likely nitrogen containing molecules.

3.3 Conclusion

Complex refractive indices at $\lambda = 405$ and 532 nm and corresponding chemical composition of haze particles synthesized by a spark discharge source with different amounts of CH_4 in N_2 are reported. The retrieved real refractive indices are similar to most previous studies. However, this study, along with most other studies, finds the magnitude of the imaginary refractive indices to be lower than those of Khare et al. (1984). Future model sensitivity studies using the different literature values of haze optical constants should give a better understanding of the impact of the lower k values on modeled planetary processes that require the complex refractive index of haze as an input parameter.

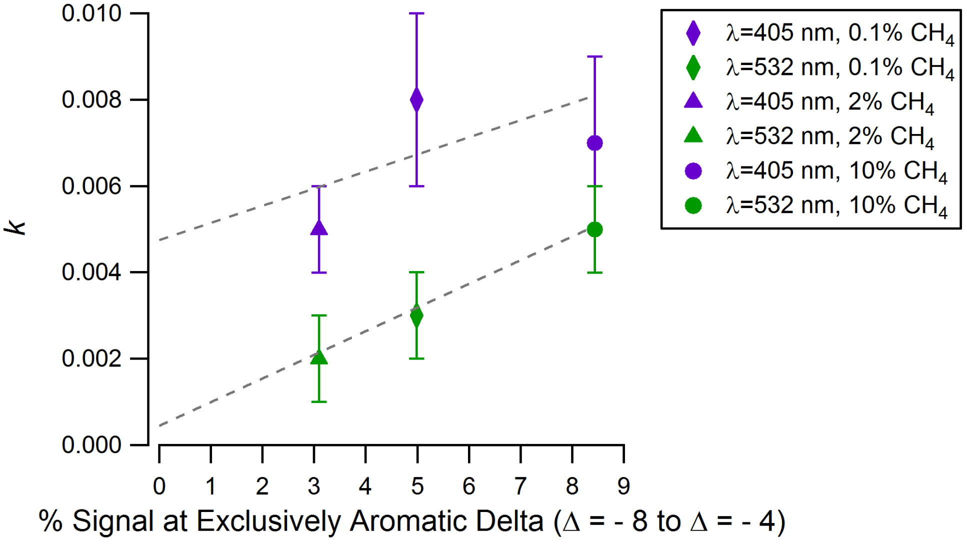

Figure 3.9: Haze k values versus the % signal from exclusively aromatic delta numbers for both $\lambda = 405$ and 532 nm. Fit lines from linear regressions are included to demonstrate the likely source of haze particle absorption at both wavelengths. Since the percent of aromatic signal plotted here does not include all delta numbers that contain aromatic functional groups, i.e. Δ = -2 and -3, these aromatic percentages are not the exact aromatic content in each haze.

Further, the complex refractive index values retrieved in this study depend strongly on the wavelength of light. At $\lambda = 532$ nm, the absorption observed by the haze particles is mainly due to aromatic absorption, while at $\lambda = 405$ nm, the haze particle absorption is due to both aromatics and nitrogen containing molecules. Since many planetary bodies in our solar system have an organic haze, this result is useful in correlating the haze chemical and optical properties. Moreover, the correlation between optical constants and chemical properties can be useful during the quest to find early Earth-like hazy exoplanets. Since the optical constants of these exoplanet hazes will be entirely unknown, understanding the relationship between the optical and chemical properties of haze can be helpful when determining the behavior of hazes in these exoplanet atmospheres.

4 The Effect of Oxygen on Haze Analog Properties

4.1 Introduction

While the hazes formed in oxygenated and non-oxygenated atmospheres are chemically distinct, many modeling studies use the optical properties, specifically the complex refractive index (m), of Titan haze analogs produced with CH_4 in N_2 to simulate haze that could have existed in the ancient Earth's atmosphere (Pavlov et al., 2001; Domagal-Goldman et al., 2008; Haqq-Misra et al., 2008; Wolf and Toon, 2010). The complex refractive index, $m = n + k\mathrm{i}$, describes scattering (n) and absorption (k) of light by the haze particles and depends on particle composition. Additionally, it is also common to use a particle density of 1 g cm^{-3} (see Arney et al. 2016) or values substantially > 1 based on Titan-like organic solids (Sagan and Chyba, 1997) for haze particles in early Earth models. Density depends on particle composition, in addition to particle shape and internal structure, and could be heavily influenced by oxygen content.

Since the complex refractive index and the density of haze particles are both common input parameters for modeling atmospheric hazes, using the values representative of the atmosphere in question is desirable. The complex refractive indices at a wavelength of 405 nm and particle effective densities for organic hazes produced by the ultraviolet (UV) excitation of methane, carbon dioxide and varying amounts of molecular oxygen in nitrogen in a flow system are presented. These values are compared to a methane-only haze analog as a baseline for haze analogs produced in the absence of oxygenated species. The specific precursor gas mixtures used included 0.1% CO_2, 0.1% CH_4 and 0, 2, 20 and 200 ppmv O_2 in N_2. A CO_2:CH_4 ratio of 1:1 was chosen since it produces sufficient aerosol signal for the instrumentation used in this study (Trainer et al., 2006; Hasenkopf et al., 2010). Additionally, the methane-only haze analog was produced with 0.1% CH_4 in N_2 to keep the CH_4 concentration consistent between each haze analog.

4.2 Results and Discussion

4.2.1 Particle Effective Density and Mass Loading

Size distributions measured by the Q-AMS and SMPS for the particles produced in this study are shown in Figure 4.1. It was not possible to measure the Q-AMS size distribution for the particles produced with 200 ppmv O_2 because of the smaller diameters of these particles. The aerodynamic lens transmits particles with a d_{va} between 20 and 1000 nm but the collection efficiency drops off steeply for $d_{va} < 60$ nm (Jayne et al., 2000). About 60% of the particles produced with 200 ppmv O_2 have diameters less than 60 nm. Moreover, the AMS y-axis is normalized to the peak area because the AMS measures the size distribution for the most prominent organic peaks, not every peak in the mass spectrum.

Using the mode d_{va} and d_m from the size distributions for each haze analog, the particle effective densities were calculated by the relationship shown in DeCarlo et al. (2004) and described in Chapter 2.6. The calculated effective densities are included in Table 4.1 and Figure 4.2a shows the particle effective densities as a function of precursor O_2. Because the Q-AMS could not measure the size distribution for the aerosol produced with 200 ppmv O_2, the particle effective density for this analog could not be calculated. To compare to haze analogs synthesized without any oxygenated species present, the effective density of photochemical haze analogs produced with 0.1% CH_4 in N_2 from Hörst and Tolbert (2013) is included as the blue point.

As seen in Figure 4.2a, as the oxygen content in the precursor gas mixture increases (by adding CO_2 and then O_2), the particle effective density increases. The trend of increasing particle density with increasing particle O:C ratio has been observed for Earth aerosol (Pang et al., 2006) and planetary haze analogs (He et al., 2017; Hörst et al., 2018a), suggesting that the oxygen content in the haze analogs produced in this study is increasing with precursor O_2. To confirm this, a measure of oxygen content as a function of precursor O_2 was made using the Q-AMS where the peak at $m/z = 44$ (COO^+) was compared to the total organic

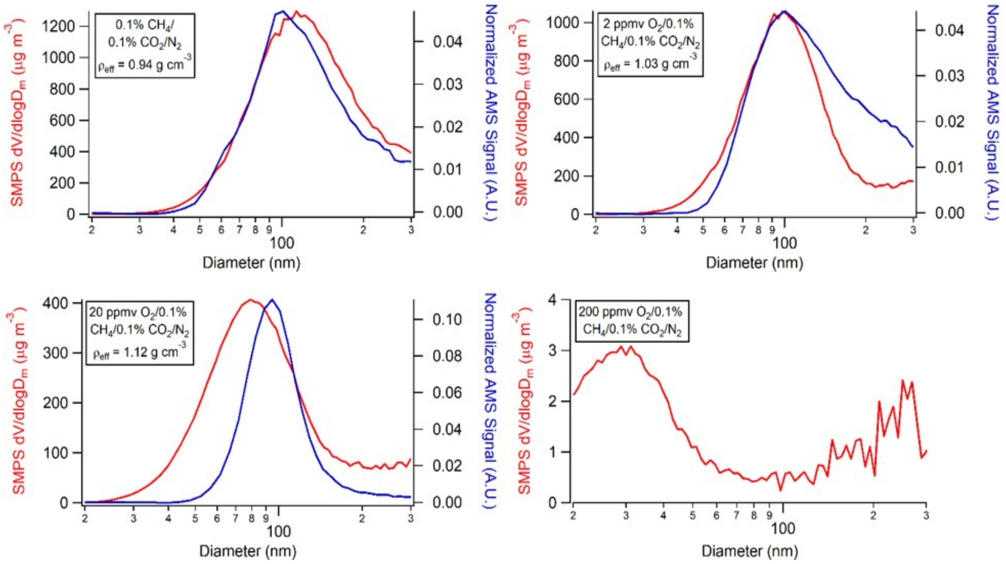

Figure 4.1: Size distributions measured by the SMPS and Q-AMS for haze particles produced in this study. The AMS signal is normalized to the total peak area because the size distributions measured by the AMS are for the most prominent organic peaks, which is not equal to the total number of peaks in the mass spectrum. The mode diameters were used to calculate particle effective density. Due to the low collection efficiency by the AMS for particles with diameters less than 60 nm, the size distribution for the particle population produced with 200 ppmv O_2 could not be measured.

			$\lambda = 405$ nm	
Mixture	ρ_{eff}(g cm^{-3})	m/z 44/total organics	n	k
0.1% CH_4/N_2	0.65 ± 0.11[a]	- - -	1.40 ± 0.02	0.002 ± 0.001
0.1% CH_4/0.1% CO_2/N_2	0.94 ± 0.03	0.081 ± 0.004	1.58 ± 0.04	$0.001\ ^{+0.002}_{-0.001}$
2 ppmv O_2/0.1% CH_4/ 0.1% CO_2/N_2	1.03 ± 0.05	0.084 ± 0.005	1.53 ± 0.03	0.002 ± 0.002
20 ppmv O_2/0.1% CH_4/ 0.1% CO_2/N_2	1.12 ± 0.05	0.094 ± 0.001	1.67 ± 0.03	$0.002\ ^{+0.003}_{-0.002}$

Table 4.1: Uncertainties in particle effective density and m/z 44 to total organics ratio are the 1σ standard deviation of the reproducibility of each experiment. Uncertainties in n and k result from 1σ standard deviations in the extinction, absorption and particle number density measurements at each particle mobility diameter, along with the 1σ standard deviation of the reproducibility of each retrieval. Using the standard deviation for the error bars of the retrieved k values results in a $k < 0$ for certain analogs. However, k cannot be negative so the lower bound error bar for these analogs ends at $k = 0$.

[a] Hörst and Tolbert (2013)

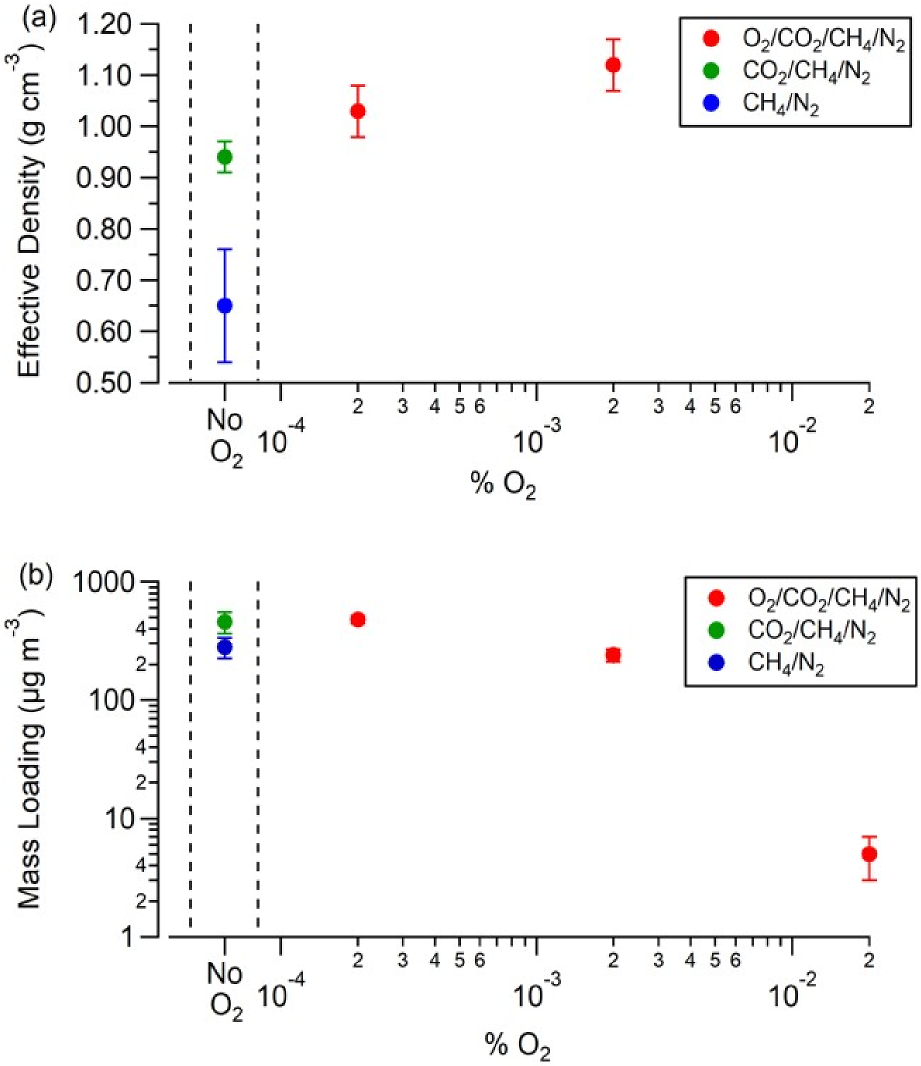

Figure 4.2: (a) Particle effective density and (b) particle mass loading calculated from the particle effective density as a function of precursor O_2. The blue density value is the effective density measured by Hörst and Tolbert (2013) for particles produced with 0.1% CH_4/N_2 and the blue particle mass loading value is the particle mass loading calculated from the values reported in Hörst and Tolbert (2013) for particles produced with 0.1% CH_4/N_2, as well. To calculate the mass loading for particles produced with 200 ppmv O_2, the effective density of the particles produced with 20 ppmv O_2 was used. Since density increases with increasing precursor O_2, the calculated mass loading for the particles produced with 200 ppmv O_2 would be a lower limit.

signal and is included in Table 4.1. As particles are produced with increasing amounts of precursor O_2 from 0, 2 and then 20 ppmv, the ratio of $m/z = 44$ to the total organic signal increases as 0.081 ± 0.004, 0.084 ± 0.005 and 0.094 ± 0.001, respectively, confirming that as precursor oxygen increases to 20 ppmv, oxygen incorporation into the particles increases as well. Since the particles produced with 0 and 2 ppmv O_2 have ratios similar within error bars that are not statistically different from each other, it is possible that these two haze analogs have similar oxygen contents. Due to possible particle morphology differences, these two haze analogs can be compositionally similar but still have statistically different effective densities.

Using the haze analogs' calculated effective densities and the SMPS measured particle number densities, haze analog mass loadings (μg m^{-3}) were calculated. Figure 4.2b displays the mass loading for each haze analog, including the mass loading of photochemical haze analogs produced with 0.1% CH_4 and N_2 calculated using the reported values in Hörst and Tolbert (2013). The effective density measured for the 20 ppmv O_2 haze analog (1.12 g cm^{-3}) was used to calculate the mass loading for the 200 ppmv O_2 haze analog. Since effective density increases with oxygen content, the 200 ppmv O_2 haze analog mass loading represents a lower limit. As Figure 4.2b shows, haze analog mass loading decreases non-linearly with precursor O_2 concentration. Additionally, the mass loading of haze produced with 1:1 CO_2:CH_4 in N_2 is slightly greater than without CO_2, which Trainer et al. (2006) also observed. Moreover, the total mass loading of the haze produced with trace amounts of molecular oxygen is substantial. Even with the addition of 200 ppmv precursor O_2, the mass loading of haze in these experiments is comparable to current mass loadings of organic aerosol in the Earth's atmosphere (Junker et al., 2004; Gupta et al., 2007; Jimenez et al., 2009; Levy et al., 2014; Wang et al., 2016). Therefore, while not being a thick atmospheric haze, this amount of aerosol could still greatly impact the radiative budget and surface temperature of the early Earth, just as the current aerosol in Earth's atmosphere do today.

4.2.2 Particle Complex Refractive Indices

Figure 4.3 shows an example of the extinction and absorption efficiency (Q_{ext} and Q_{abs}, respectively) as a function of particle size for the $CO_2/CH_4/N_2$ haze analog. The points are experimentally retrieved data and the lines are fits of the data using the procedure in Zarzana et al. (2014) and Ugelow et al. (2017) to determine the real and imaginary refractive indices using Mie theory (Chapter 2.4). The figure shows strong agreement between the measured and calculated extinction and absorption efficiencies, and is representative of the agreement between the calculated and experimental data for all the haze analogs studied. Table 4.1 includes the complex refractive indices at 405 nm retrieved for the haze analogs produced in this study, including a non-oxygen containing CH_4/N_2 haze analog. Using the standard deviation for the error bars of the retrieved k values results in a $k < 0$ for certain analogs. However, k cannot be negative so the lower bound error bar for these analogs ends at $k = 0$.

As oxygen is added via CO_2 and O_2, the real refractive index of the resulting haze generally increases. This could mean that greater oxygen incorporation into the haze analogs results in increasing n values. While the n values for the CO_2-containing mixtures without O_2 and with 2 ppmv O_2 are similar within error bars, based on the relative oxygen content measured by the Q-AMS for each haze analog, these two analogs are believed to be compositionally similar.

Whereas haze particles produced with just CH_4 and N_2 have a slight absorption ($k = 0.002$), particles produced with oxygenated species are non-absorbing. Although the measured imaginary refractive indices of the oxygenated analogs are slightly greater than zero, the large error in the retrieved values cannot exclude $k = 0$, especially when considering the raw PAS signals. The raw PAS signal for the haze analog produced with 0.1% CH_4 in N_2 is the only haze analog with raw absorption signal greater than zero, whereas the other haze analogs' raw absorption signal average to about zero (or less). Hasenkopf et al. (2010) measured a larger k value ($k = 0.055$) for haze analogs produced with 0.1% CH_4 and 0.1% CO_2 in N_2 at 532 nm and found that producing particles with CO_2 enhances particle absorp-

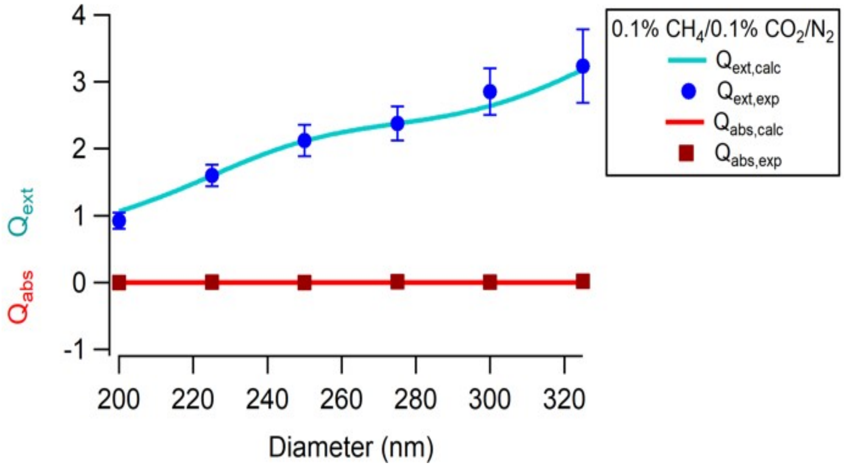

Figure 4.3: A representative plot of extinction efficiency (Q_{ext}) and absorption efficiency (Q_{abs}) versus particle mobility diameter for the $CO_2/CH_4/N_2$ haze analog. The points represent the experimental data and the lines represent the calculated Q_{ext} and Q_{abs} using the n and k that result in the minimization of the merit function. For each haze analog retrieval, the calculated n and k fit the experimental data well. Ugelow et al. (2017) explain the fit further.

tion at this wavelength. However, that experiment was done with CaRD alone and Zarzana et al. (2014) demonstrated that coupling extinction to absorption measurements, as in the present study, greatly improves the complex refractive index retrieval, particularly resulting in enhanced accuracy and precision in k. Gavilan et al. (2017) observed a similar trend to the present study where particles produced with CH_4 and N_2 absorb light more strongly than particles produced with a 1:1 CO_2:CH_4 ratio in N_2. Additionally, for the portion of the visible light spectrum that they were able to obtain valid imaginary refractive indices, low k values ($\leq 10^{-3}$) were reported.

To further confirm that the oxygen containing haze analogs produced in this study are non-absorbing, extinction ($\mathrm{b_{ext}}$, $\mathrm{Mm^{-1}}$) and scattering ($\mathrm{b_{sca}}$, $\mathrm{Mm^{-1}}$) were measured by a cavity attenuated phase shift spectrometer ($\mathrm{CAPS-PM_{ssa}}$; (Onasch et al., 2015; De Haan et al., 2017)) at 450 nm for the total aerosol size distribution. The ratio of particle scattering to particle extinction describes the wavelength dependent single-scattering albedo ($\tilde{w}$), thus the particle's radiative impact, where $\tilde{w} = \frac{\mathrm{b_{sca}}}{\mathrm{b_{ext}}}$. A particle with $\tilde{w} < 1$ is light absorbing, whereas as particle with $\tilde{w} = 1$ is non-absorbing. Figure 4.4 displays the single-scattering albedo calculated from the CAPS measured extinction and scattering by the CH_4/N_2 and $CO_2/CH_4/N_2$ haze analogs, with error bars reflecting the measurement reproducibility

The CAPS single-scattering albedo at 450 nm rises from 0.947 ± 0.008 to 0.995 ± 0.007 when CO_2 is added to the haze mixture, confirming that the aerosol produced without CO_2 is light absorbing, whereas the aerosol produced with CO_2 is essentially non-absorbing. Included in Figure 4.4 is the single-scattering albedo for the particles produced in this study at 405 nm calculated using the retrieved refractive index, mode particle diameter and Mie theory. Agreeing with what is observed at 450 nm, the aerosol produced with CO_2 is non-absorbing, whereas the aerosol produced with only CH_4 and N_2 is light absorbing, and absorbs more light at 405 nm than at 450 nm. This strong wavelength dependence is typical for brown carbon oligomerized aerosol, and is also observed by Gavilan et al. (2017). A haze that is non-absorbing would form a light-scattering layer in the atmosphere. This light

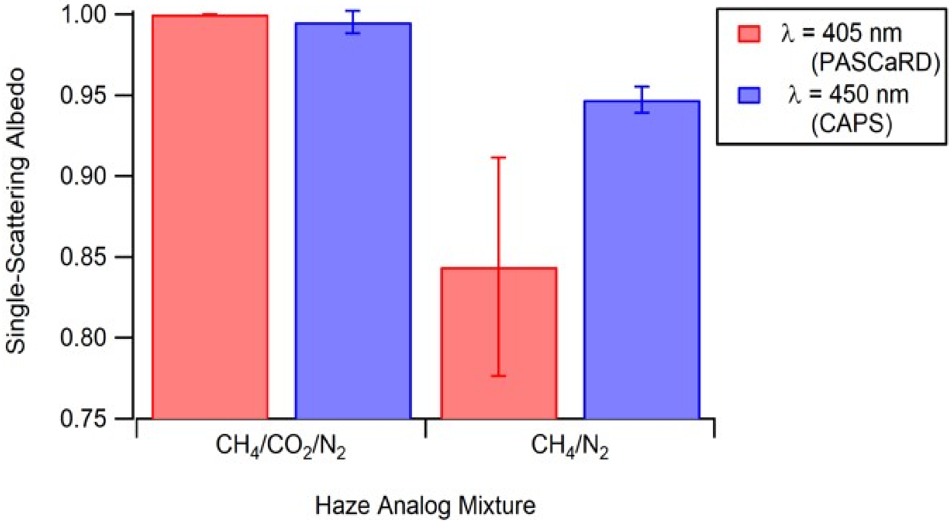

Figure 4.4: The single-scattering albedo measured by CAPS-ssa at 450 nm and calculated from the PASCaRD retrieved refractive index at 405 nm using Mie Theory and the mode particle mobility diameter. The error bars represent the 1σ standard deviation of the reproducibility of both instrument retrievals. In both cases the aerosol produced with the addition of CO_2 is less absorbing than the aerosol produced with only CH_4 and N_2.

scattering haze would prevent certain wavelengths of sunlight from reaching a planets surface. Sagan and Chyba (1997) and Wolf and Toon (2010) calculate that an Archean organic haze could act as an ultraviolet radiation shield to greenhouse gases below the haze. While these studies assume a light absorbing haze, a light scattering haze could act as a shield, as well.

4.3 Conclusion

The particle effective density, particle mass loading and complex refractive indices at 405 nm of photochemical organic hazes synthesized with CO_2, CH_4 and increasing amounts of O_2 in N_2 are reported. Large amounts of haze can form in the presence of up to 20 ppmv O_2, with small amounts of haze particles still forming in the presence 200 ppmv O_2. Additionally, as more oxygen is incorporated into the particles, the effective density and real refractive index increase. With the increase of oxygen in the particles, however, the imaginary refractive index decreases, resulting in non-absorbing haze particles. A light scattering haze would reduce certain wavelengths of light from reaching a planets surface, possibly influencing its climate.

5 Ion Chemistry During Early Earth Haze Formation

5.1 Introduction

Current photochemical modeling that predicts haze formation in the early Earth's atmosphere stem from models by Kasting et al. (1989) and Pavlov et al. (2001). While newer models modify the program to include properties like a fractal haze (Arney et al., 2016) or update the sulfur photochemistry (Zahnle et al., 2006), the organic haze formation scheme proposed by Pavlov et al. (2001) is consistently used. However, the haze that is predicted to form by the Pavlov et al. (2001) model would only include carbon and hydrogen, where the gas-phase is set to condense into haze particles upon the formation of C_4H_2 and C_5H_4. Additionally, gas-phase neutral chemistry is the only pathway that is predicted to lead to haze formation. Because early Earth haze and haze formation was not well understood, the Pavlov et al. (2001) model had to make these assumptions. Since then, however, laboratory simulations of early Earth organic hazes have shown that both oxygen (Hicks et al., 2016; H*ö*rst et al., 2018b; Ugelow et al., 2018) and nitrogen (Hicks et al., 2016) are incorporated into early Earth organic haze analogs. In addition, if Titan is used as an analog for the early Earth, organic haze formation is likely initiated by ion-neutral chemistry and not gaseous neutrals alone (Waite Jr. et al., 2007; Coates et al., 2007, 2010; Wahlund et al., 2009; Lavvas et al., 2013).

Possible ionization sources in the haze formation region of the early Earth's atmosphere include photoionization and galactic cosmic rays. Using Titan as an analog for haze formation in the early Earth's atmosphere, ions would have reacted with neutrals and oppositely charged ions in the upper atmosphere, where they would ultimately become condensed aerosol particles (Lavvas et al., 2013). However, unlike Titan, the early Earth would have contained CO_2 and, depending when in geological time, different amounts of O_2. Laboratory experiments have shown that the composition of haze is different when formed in the presence of oxygen containing species (Trainer et al., 2006; Hicks et al., 2015, 2016; H*ö*rst et al., 2018b; Ugelow et al., 2018), and therefore, it is likely that the gaseous ion-neutral chemistry resulting in haze formation would be different than what is observed in Titan's atmosphere, as well.

When atmospheric species are ionized, the gas species that will ultimately have the positive and negative charges will depend on both the proton affinity and the electron affinity of all the gases in that atmosphere. For positive organic ions, the species with the highest proton affinity will attract the proton and thus become a positive ion. Therefore, what becomes a positive ion and what remains a neutral greatly depends on all of the gas species present in an atmosphere. In atmospheres with a carbon, hydrogen, oxygen and nitrogen source, where neutral gases can be composed of any of these elements, the proton affinity of hydrocarbons generally increases with the inclusion of oxygen and then nitrogen in the molecule backbone. An example of proton affinities increasing for oxygen and nitrogen containing molecules is shown in the top portion of Table 5.1, above the dashed line.

If the species included in the top portion of Table 5.1 were in an atmosphere together, and the time between ion-molecule collisions is shorter than the ion lifetime, $C_4H_{12}N_2$ would more likely exist in its protonated form than C_4H_{10}. Therefore, carbon and hydrogen containing species with nitrogen would most likely exist as a positive ion than a hydrocarbon, or a carbon and hydrogen containing species with oxygen. Additionally, if molecules have multiple nitrogen atoms or a mix of nitrogen and oxygen atoms, generally the molecule with the greatest number of nitrogen atoms would still have the highest proton affinity. However, this is a generalization because acid and base strength also plays a role, where weaker acids and stronger bases have higher proton affinities than stronger acids and weaker bases. An example of this is shown in the bottom portion of Table 5.1, below the dashed line. Pyridine, which only has one nitrogen atom, as a higher proton affinity than pyrazine, which has two nitrogen atoms. This is because pyridine is a stronger base (pKa = 5.25) than pyrazine (pKa = 0.37) since the lone pair on the nitrogens can act as electron withdrawing groups, making pyrazine less likely than pyridine to attract a proton.

Molecule	Formula	Proton Affinity (kJ/mol)
Isobutane	C_4H_{10}	677.8
1-Butanol	$C_4H_{10}O$	789.2
1,4-Butanediol	$C_4H_{10}O_2$	915.6
1- Butanamine	$C_4H_{11}N$	921.5
4-Amino-1-butanol	$C_4H_{11}NO$	984.5
1,4-Butanediamine	$C_4H_{12}N_2$	1005.6
- - - - - - - - - - - - -	- - - - - - - - - - -	- - - - - - - - - - - -
Pyridine	C_5H_5N	930.0
Pyrazine	$C_4H_4N_2$	877.1

Table 5.1: Proton affinities for six C_4 molecules that demonstrate that as oxygen and nitrogen in the molecule increases, the proton affinity increases. However, the proton affinity values of pyridine and pyrazine demonstrate that other properties, like acid and base strength, need to be taken into account as well. Proton affinity values are from Hunter and Lias (1998).

There are two possible ways for the negative organic ions to form. First, when a molecule is ionized, an electron can be lost. Like the positive ions where the molecule with the highest proton affinity will attract the proton to become a positive ion, the molecule with the highest electron affinity will attract that lost electron and become a negative ion. In addition to negative ion formation resulting from differences in electron affinity, proton affinity differences can also result in the formation of negative ions. Here, protons can be transferred from stronger acids to weaker acids, resulting in negatively charged conjugate bases (Shuman et al., 2015).

Because the ion chemistry would likely be different during early Earth haze formation than during Titan haze formation, laboratory simulations are necessary to characterize the ions that could have been produced in early Earth's atmosphere. Here the ion chemical composition was measured during the production of photochemical haze analogs with 0.1% CO_2, 0.1% CH_4 and 0, 2, 20, 200 and 2000 ppmv O_2 in N_2. These gas mixtures were chosen to have ion chemical information that corresponds to aerosol data from Ugelow et al. (2018).

5.2 Experimental

5.2.1 Atmospheric Pressure Interface Time of Flight Mass Spectrometer

To measure the ions produced during haze analog formation, an Aerodyne/Tofwerk Atmospheric Pressure interface Time of Flight Mass Spectrometer (APi-ToF-MS) was used and is shown as a schematic in Figure 5.1. Particles, gaseous neutrals and gaseous ions are produced using the flow system described in Chapter 2.1 and flow directly to the APi-ToF-MS at a flow of 100 sccm. Due to instrument requirements, a 600 sccm prepurified N_2 dilution flow was added after the reaction cell.

Cation and anion measurements cannot happen simultaneously. Instrument settings dictate which type of ion is measured, while the oppositely charged species and neutrals are removed by differential pumping. As ions travel through the mass spectrometer, they move through three separate chambers of decreasing pressure. The first two chambers have

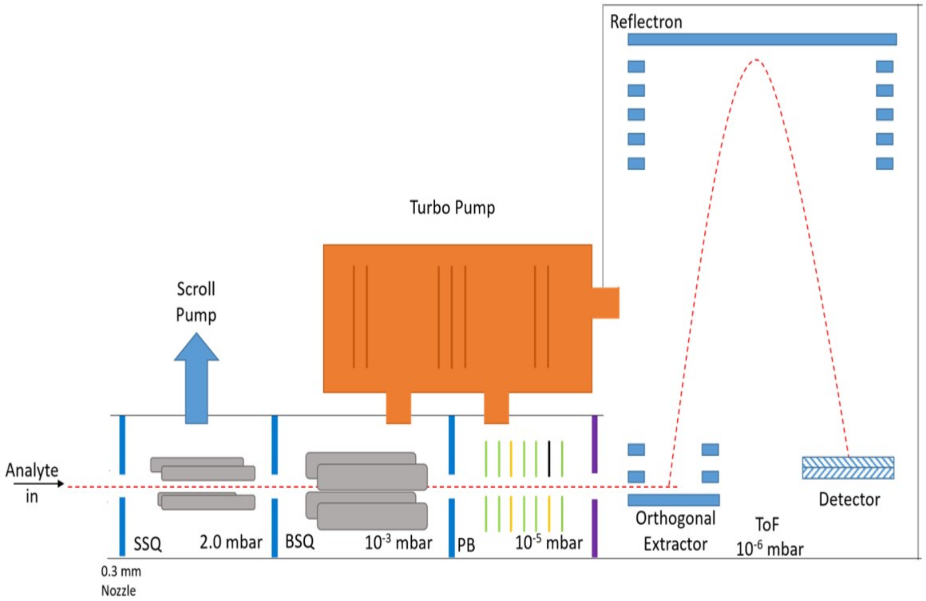

Figure 5.1: Schematic of the Aerodyne/Tofwerk Atmospheric Pressure interface Time of Flight Mass Spectrometer

separate RF-only segmented quadrupoles and the third chamber has a lens stack. The two quadrupoles and the lens stack focus and guide the ions to the time of flight chamber where they are orthogonally extracted. High resolution is achieved through the use of a reflectron. The voltages on the quadrupoles are tuned for ion transmission and resolution.

For each early Earth analog, mass spectra were recorded for the background gases (before the lamp was turned on), when the lamp was turned on (including a 25 minute lamp warm up period), when the lamp was fully warmed up and then when the lamp was turned back off. Since positive and negative ions cannot be measured simultaneously, they were measured in two separate experiments. Therefore, between each positive and negative ion experiment for a specific early Earth analog, the deuterium continuum lamp was cleaned and a new precursor gas mixture was made. This was necessary in order to measure mass spectra during the full lamp warm up in both ion modes.

Mass spectra were obtained for negative ions with a mass range of m/z = 1 - 960 and a mass resolving power of $\sim$ 7000, and for positive ions with a mass range of m/z = 1 - 707 and a mass resolving power of $\sim$ 8000. Using Aerodyne/Tofwerk Tofware (Version 2.5.10) each spectra was mass calibrated, peak fitted (custom peak width and peak shape) and integrated. Mass calibration allows for high mass accuracy ($<$ 8 ppm and $<$ 7 ppm for negative and positive ion mass calibration points, respectively). Junninen et al. (2010) explains the mass calibration process where first a mass calibration is obtained by identifying known ion peaks. Then that calibration is applied to begin identifying unknown ion peaks. The identified, previously unknown ion peaks are added to the mass calibration, fine tuning the mass calibration. Approximately one ion peak per 10 - 20 m/z range is needed for an accurate mass calibration.

Because of the high resolution, high mass accuracy and Tofware peak fitting techniques, overlapping peaks with the same nominal mass can be individually fitted and assigned a chemical formula (Cubison and Jimenez, 2015). Examples of peak fitting and characterizing peaks with the same nominal mass is shown in Figure 5.2. In addition, the integrated ion

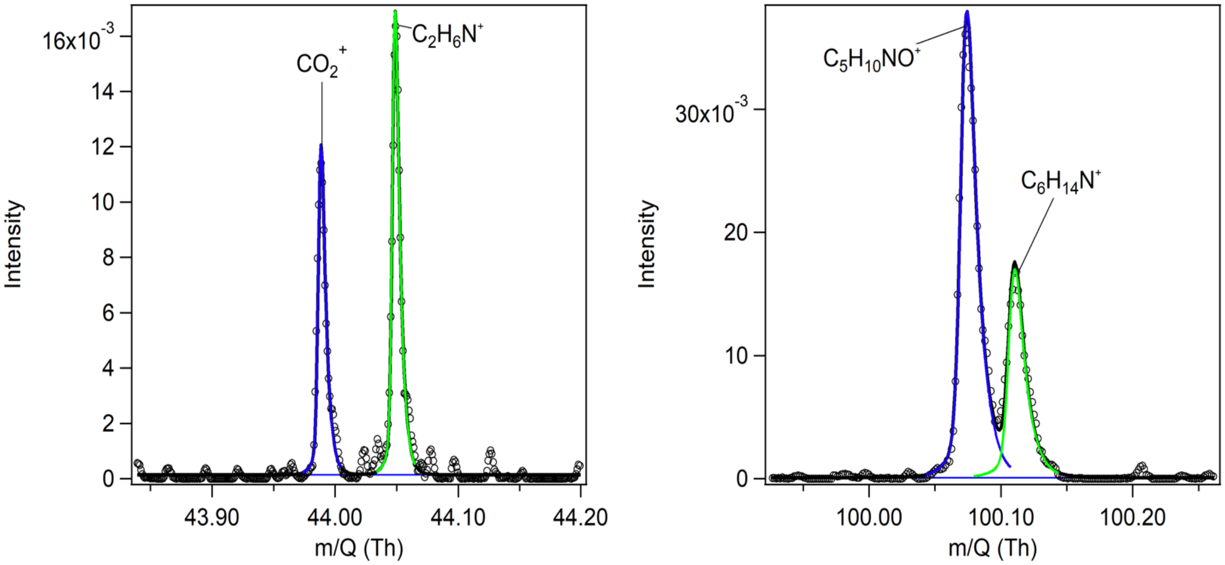

Figure 5.2: Examples of peak fitting and assigning chemical formulae to peaks with the same nominal mass

signal intensity cannot be used quantitatively because no correction for the mass-dependent ion transmission efficiency was used (Heinritzi et al., 2016). However, relative changes at a given m/z are proportional to the absolute changes in ion concentration.

5.3 Results and Discussion

5.3.1 Negative Ions

During the formation of the different haze analogs in this study, negative ions are detected by the APi-ToF-MS once the UV lamp is turned on. Figure 5.3 shows that the total ion count for negative ions increases once the lamp is turned on and returns to background levels after it is turned off. Additionally, the total number of negative ions that are observed by the APi-ToF-MS when the UV lamp is turned on increases for the analogs produced with the largest concentrations of precursor O_2. While the background for the haze analogs, with the exception of the analog produced with 2000 ppmv O_2, is essentially zero ion signal, the analog produced with 2000 ppmv O_2 has a larger (but still low) background ion signal. The higher background is likely due to the larger amount of O_2 ionizing to O_2^- from background ionizing sources, such as galactic cosmic rays and/or ground-based radiation sources (Shuman et al., 2015), thus increasing the negative ion density in the background gases. Additionally, due to the background ionizing sources, it is possible that before the lamp is turned on, there is a negative ion background due to electrons. However, since electrons are easily lost to surfaces, they would elude the background measurements. Therefore, it is possible that the low background reported in Figure 5.3 could be higher due to free electrons.

Using a scanning mobility particle sizer (SMPS, Chapter 2.3) and the particle densities measured during the study detailed in Chapter 4, the haze particle mass loading was determined for the five early Earth analogs produced in this study. The particle effective density for particles produced with 20 ppmv O_2 was used for the particles produced with 200 and 2000 ppmv O_2 (1.12 g cm^{-3}) due to the limitations described in Chapter 4.2.1. Therefore, the particle mass loadings for the two more oxidized haze particles represent a lower limit. The

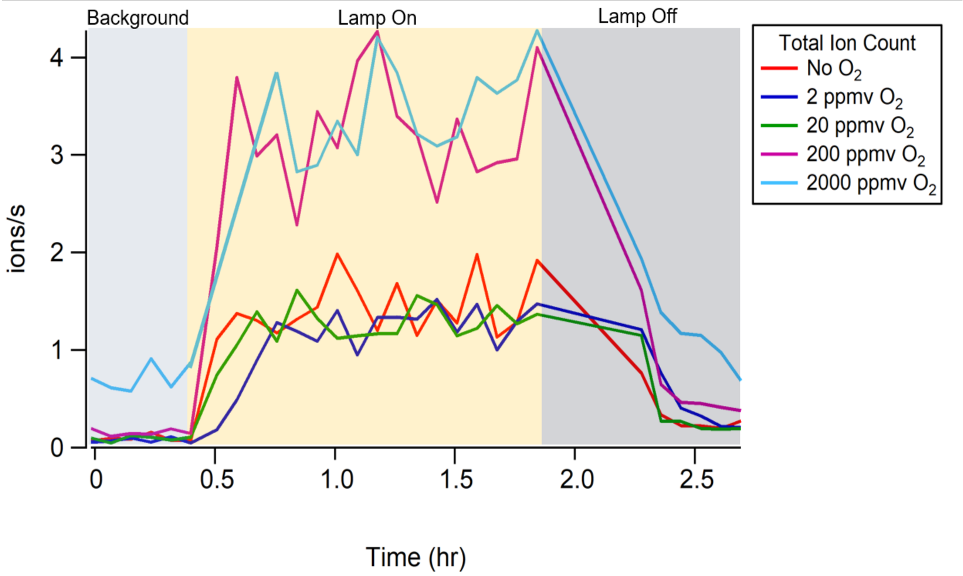

Figure 5.3: Total negative ion count during haze analog formation.

total negative ion count when the UV lamp is on during haze analog formation is compared to the particle mass loading for each haze analog. Figure 5.4 shows that there is an inverse relationship between the relative concentration of negative ions and haze, with a transition occurring between 20 and 200 ppmv precursor O_2. The inverse relationship between ion signal and haze particle mass loading could follow what is observed in Titan's atmosphere where haze forms by the reaction of ions. When more haze particles are produced, there are fewer gas-phase ions because they may have reacted with other ions, neutrals and/or aerosol and possibly turned into haze particles. However, when less haze is produced, there are more gas-phase ions possibly because they have not reacted to form haze particles. If this is what is occurring during haze analog formation, in addition to Titan, ion-neutral chemistry is likely a viable haze formation pathway for the early Earth. However, it is also possible that the total ion count is lower when there are more haze particles produced because the charge is lost to the haze particles. Since the mass range for these experiments that detect the negative ions using the APi-ToF-MS ends at $m/z = 960$, if the aerosol was negatively charged it would elude detection by the APi-ToF-MS.

Figure 5.5 includes an example mass spectrum obtained by the APi-ToF-MS when the UV lamp was turned on, after the warm up period, to produce haze analogs from 2 ppmv O_2/0.1% CO_2/0.1% CH_4 in N_2. The mass range of the negative ions measured is the same for each haze analog and negative ions are colored according to chemical composition. While the exact chemical composition of the ions differs between each analog (the complete list of identified ions is included in Appendix A), most of the negative ions produced during Archean haze analog formation contain both nitrogen and oxygen.

The chemical backbones of the ions produced during the formation of each haze analog (UV lamp on after the lamp warm up period) is shown in Figure 5.6. Each slice of the pie chart represents the percentage of the total negative ion signal measured for each haze analog. Ions with the chemical backbone of C_xNO^- include CNO^- and C_3NO^-, with the signal primarily resulting from CNO^-. Ions with the chemical backbone of NO_z^- include

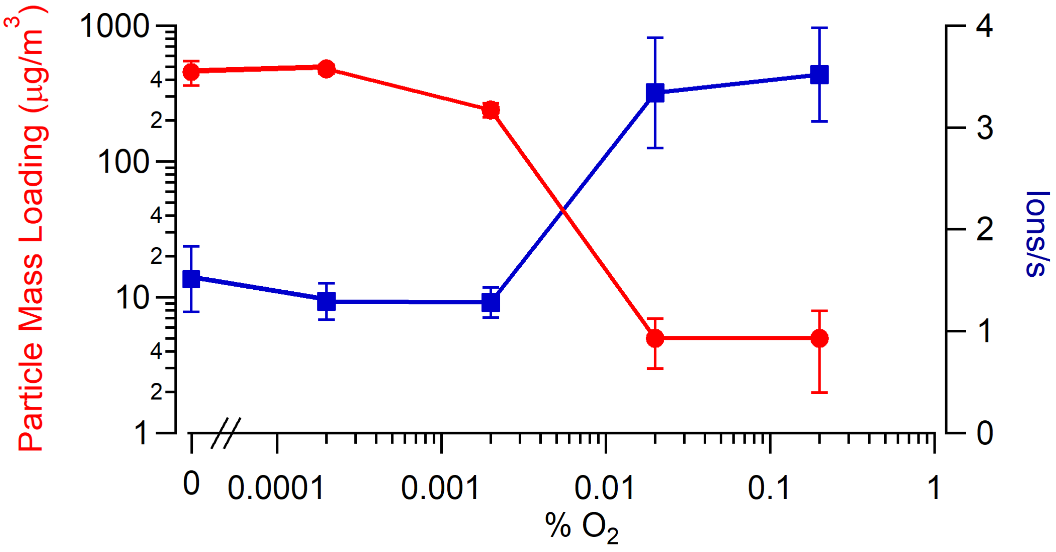

Figure 5.4: Negative ion signal and haze particle mass loading for each haze analog as a function of precursor O_2. Mass loadings are calculated from the SMPS measured number density and effective density values from Chapter 4.2.1.

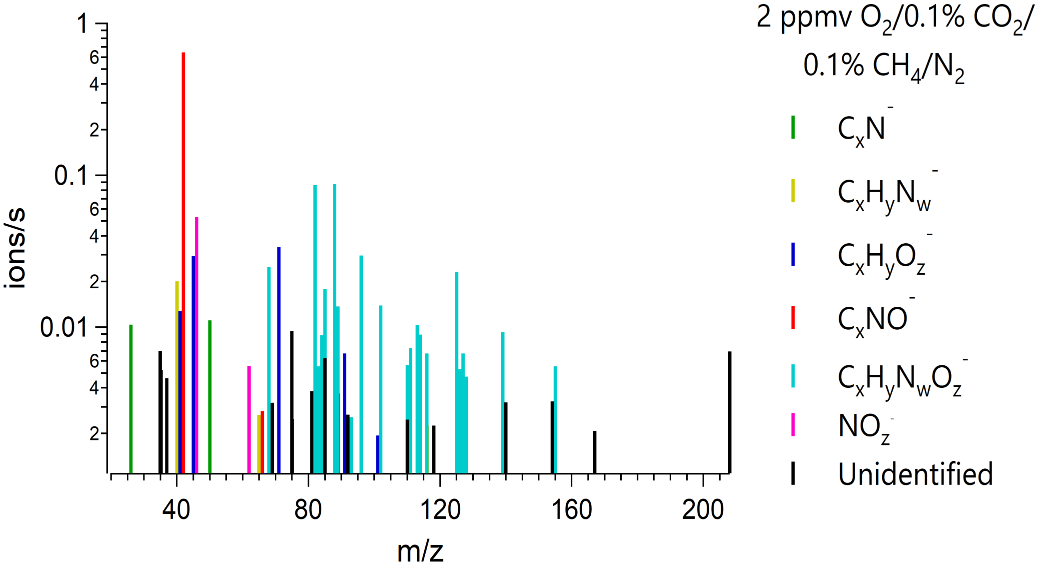

Figure 5.5: An example mass spectrum of the negative ions detected during haze analog formation from 2 ppmv O_2/0.1% CO_2/0.1% CH_4 in N_2.

NO_2^- and NO_3^-. When haze analogs are formed with 0 - 20 ppmv O_2, carbon containing negative ions with both nitrogen and oxygen are the most common species formed. However, when haze analogs are formed with 200 - 2000 ppmv O_2, the most common ion is NO_z^-, which for these analogs is mostly NO_3^-. The second most common ion for the analogs produced with the largest amounts of O_2 are ions with the backbone $C_xH_yO_z^-$. This change from ions containing mostly organic nitrogen, as the CNO^- ion, to inorganic nitrogen, as the NO_3^- ion, shows that there is a transition in the type of chemistry occurring based on the amount of precursor O_2. In addition, because of the greater nitrate signal, ions produced with the largest amounts of O_2 appear to contain less carbon. However, proton affinity differences resulting in the nitrate losing a proton instead of a carbon containing anion is likely the cause for this apparent "loss" of carbon. Therefore, it would be expected that the neutral gases that are produced during early Earth haze analog formation with $\geq$ 200 ppmv O_2 contain more carbon than the anions.

It is possible that the ion $C_xH_yN_wO_z^-$ could be NO_2^- and NO_3^- clustered to C_xH_y. If so, the increase in the NO_z^- ion signal for haze analogs produced with $O_2 \geq 200$ ppmv could be due to NO_2^- and NO_3^- declustering from C_xH_y. Figure 5.7 compares the NO_z^- signal to the $C_xH_yN_wO_z^-$ signal as a percent of the total negative ion signal. If declustering is responsible for the change in the NO_z^- signal with increasing precursor O_2, it would be expected that the increase of NO_z^- would equal the decrease of $C_xH_yN_wO_z^-$. However, the increase in NO_z^- is almost three times greater than the decrease in $C_xH_yN_wO_z^-$. Therefore, while it is possible that some declustering is occurring, it is likely that with large amounts of precursor O_2 during early Earth haze analog formation, greater amounts of nitric acid are being produced resulting in the observed NO_z^- signal increase. This is also supported by the detection of NO_3^- clustered to HNO_3 ($HN_2O_6^-$) for haze analogs formed with $\geq$ 200 ppmv precursor O_2.

Additional insight about the chemical properties of the carbon containing ions can be determined by calculating the rings plus double bond equivalency (RDBE), and the H/C, N/C and O/C molar ratios of the ions. RDBE is a measure of the degree of unsaturation in

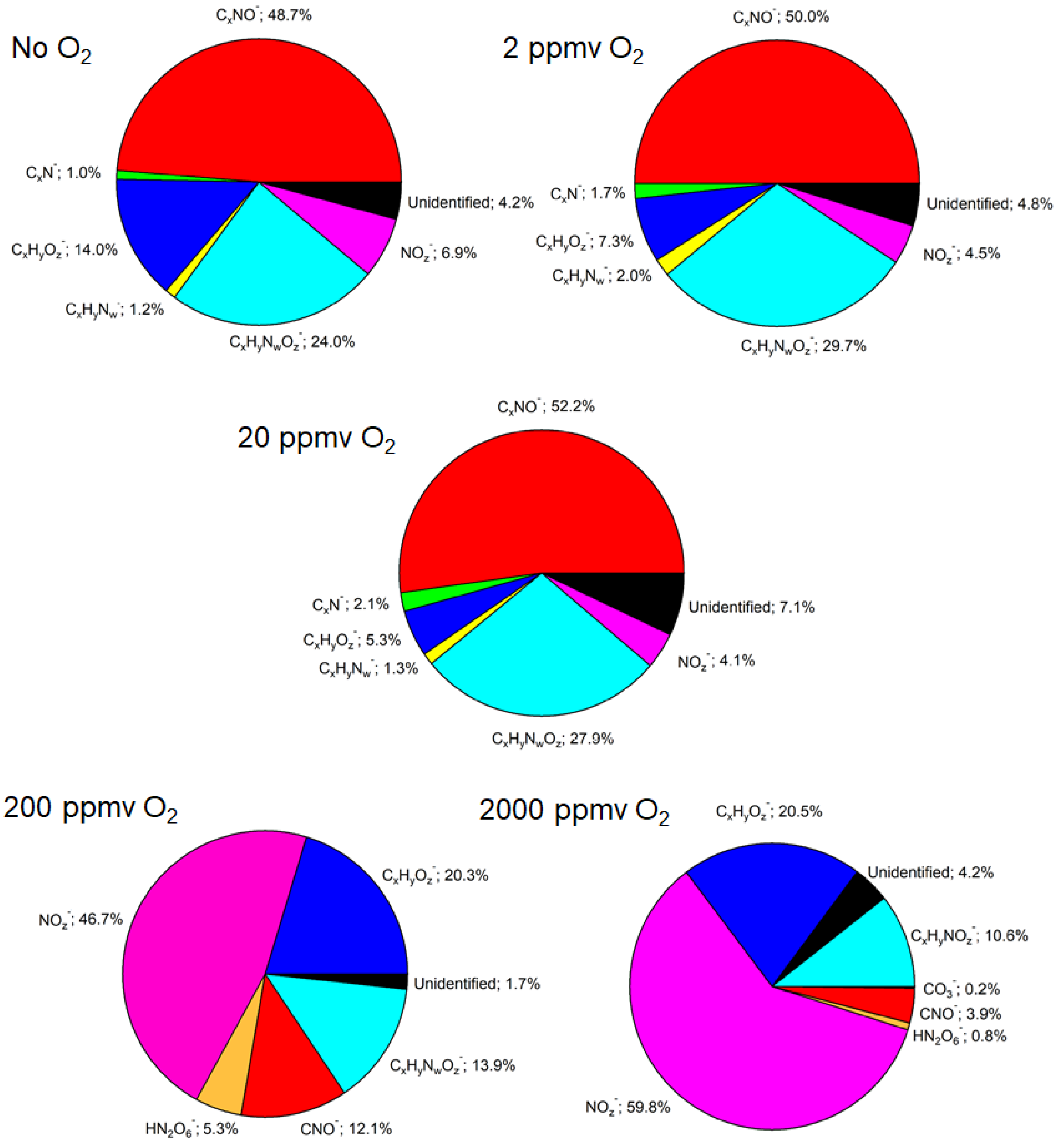

Figure 5.6: Negative ion chemical composition during haze analog formation. Each slice is the percentage of the total negative ion signal measured for each haze analog.

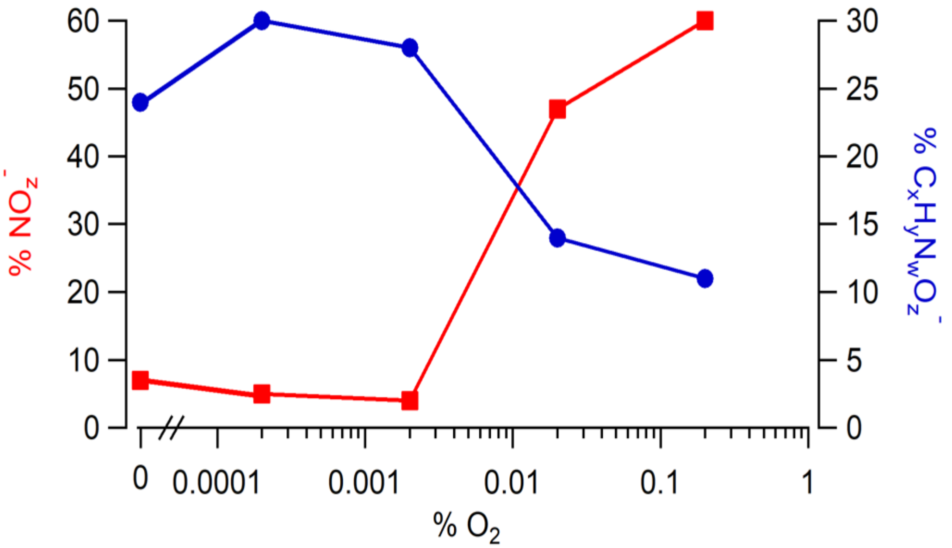

Figure 5.7: NO_z^- signal compared to $C_xH_yN_wO_z^-$ signal. While it is possible NO_z^- clusters form during haze analog production with lower amounts of O_2, the increase in NO_z^- signal with increasing precursor O_2 likely results from increased HNO_3 production.

an organic molecule. It is calculated as $\mathrm{RDBE} = \mathrm{C} - \frac{\mathrm{H}}{2} + \frac{\mathrm{N}}{2} + \frac{\mathrm{X}}{2} + 1$, where C is the number of carbon atoms, H is the number of hydrogen atoms, N is the number of nitrogen atoms and X is the number of halogen atoms in the organic molecule. Molecules that are unsaturated have larger RDBEs than molecules that are saturated. For an empirical chemical formula to be a stable molecule, the RDBE must be a positive integer, where each integer represents either a pi bond or a ring. However, the RDBE of ions and clusters can violate this rule. Ions, with the loss or gain of a proton, will have positive, fractional RDBEs that are 0.5 less than (positive ions) or greater than (negative ions) the RDBE of the parent neutral. Additionally, clusters can have negative RDBEs.

Figure 5.8a shows the signal-weighted average RDBE and the signal-weighted average H/C, N/C and O/C molar ratios of the carbon containing ions as a function of precursor O_2. Figure 5.8b includes the signal-weighted N/C and O/C molar ratios compared to the signal-weighted H/C molar ratio. As analogs are produced with more precursor O_2, their RDBE decreases. This means that the ions are more saturated when larger amounts of precursor O_2 is used to form haze analogs. Additionally, the ion H/C ratio increases for the analogs produced with the greatest concentrations of precursor O_2, supporting the trend of increasing ion saturation observed by the decreasing RDBE. The O/C ratio, which is consistently the highest molar ratio for all of the analogs, increases for the two analogs formed with 200 and 2000 ppmv O_2. The other three analogs produced with 0, 2 and 20 ppmv O_2 have similar O/C ratios to each other. The major difference for these analogs is that the analog produced with no O_2 has an $\mathrm{O/C} > 1$, whereas the other two lower precursor O_2 concentration analogs have an $\mathrm{O/C} < 1$. Also, the N/C ratio is similar for the analogs produced with less O_2 but then decreases as analogs are made with larger amounts of O_2.

Based on the molar ratio and RDBE calculations, negative ions become more oxidized and more saturated with increasing precursor O_2 during early Earth haze analog formation. Comparing the percent of the total negative ion signal due to the ion backbone $\mathrm{C_xH_yO_z^-}$ to the RDBE and O/C molar ratio, illustrated in Figure 5.9, shows a similar trend with

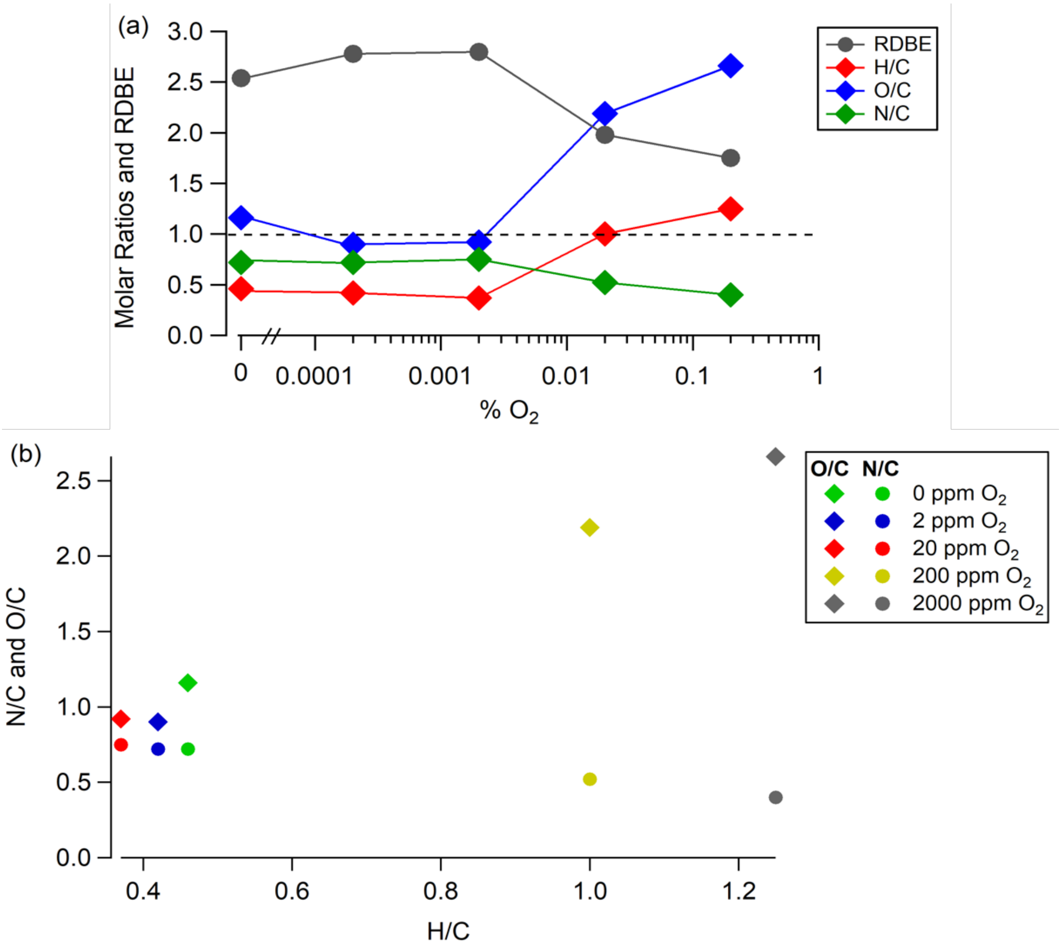

Figure 5.8: (a) Signal-weighted average molar ratios and RDBE of the carbon-containing negative ions produced during haze analog production and (b) signal-weighted average N/C and O/C versus H/C. Ions become more oxidized and more saturated with precursor O_2.

increasing precursor O_2. It is possible then that the more oxidized and saturated ions that arise during early Earth haze analog formation with 200 and 2000 ppmv precursor O_2 are peroxides (R-OO-R).

5.3.2 Preliminary Positive Ion Results

Unlike the negative ion chemistry, the positive ion chemistry for each haze analog is more obviously influenced by background ionization sources, such as galactic cosmic rays and/or ground-based radiation (Shuman et al., 2015). This is shown in Figure 5.10 where the total ion count for the positive ions does not change in intensity during the course of the haze formation experiments. While it is possible that there are small changes in the ion signal when the lamp is turned on from direct ionization by the lamp, these small changes cannot be measured by the APi-ToF-MS in the current setup. Since the lamp's ionization energy is up to 10.8 eV, the precursor gases in the analogs would not be ionized directly. Rather, photochemical reactions that produce neutrals and radicals with lower ionization energies could be directly ionized. In addition, unlike what is observed with the negative ions, the total ion count of the positive ions is the same for each early Earth analog.

Due to the inability to obtain a sufficient mass calibration for the positive ions that form during early Earth haze analog production with precursor O_2 concentrations ≥ 200 ppmv, the chemical compositions of these positive ions remain unknown. The complete list of identified positive ions is included in Appendix A for ions formed during the production of haze analogs with ≤ 20 ppmv precursor O_2. Despite the inability to identify the exact chemical compositions of the positive ions formed during the production of the most oxidized analogs, their raw mass spectra still provide insight on general chemical properties. The raw spectra for the positive ions formed during the production of haze analogs with 0, 2 and 20 ppmv O_2 are similar to each other, and the raw spectra for the positive ions formed during the production of haze analogs with 200 and 2000 ppmv O_2 are different from the other analogs' spectra but similar to each other, as well. Example mass spectra for both of these

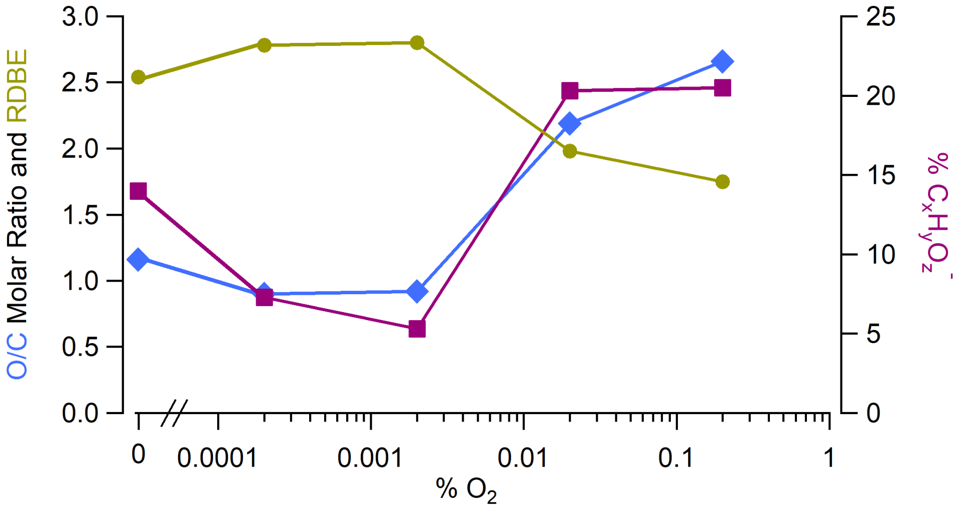

Figure 5.9: RDBE and O/C molar ratio compared to % $C_xH_yO_z^-$ signal for each analog. The increase in % $C_xH_yO_z^-$ signal with precursor O_2 suggests that the negative ions are composed of possibly increasing amounts of peroxides.

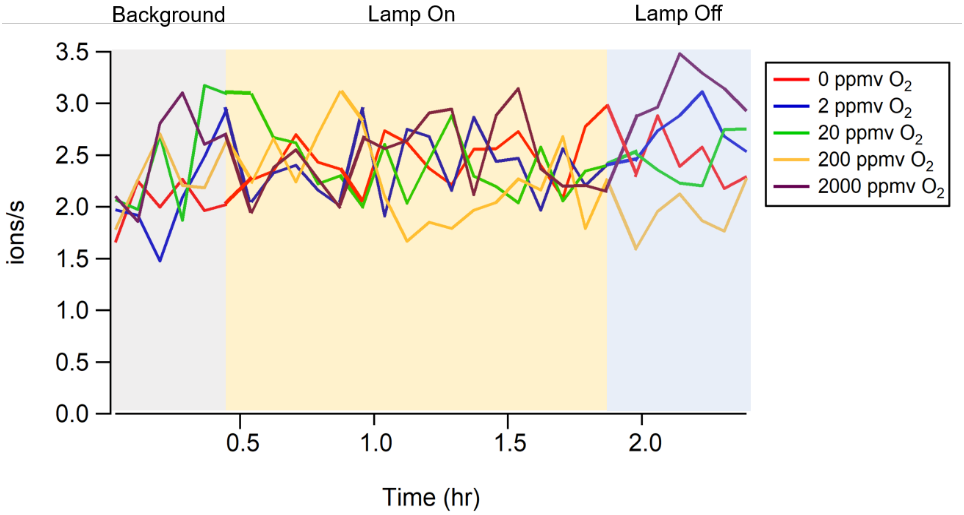

Figure 5.10: Total positive ion count during early Earth haze analog formation.

two types of raw spectra are shown in Figure 5.11. The background mass spectrum for the ions produced with no O_2 is entirely different from the mass spectrum with the lamp on. Here new species are being produced that have higher proton affinities than the background gases, and thus become positive ions. However, for the ions produced with 2000 ppmv O_2, the background mass spectrum is almost the same as the spectrum with the lamp on. This means that the species produced with larger amounts of precursor O_2 have lower proton affinities than the gases in the background. This suggests that species with less nitrogen are produced, possibly along with stronger acids and weaker bases.

Figure 5.12 includes an example positive ion mass spectrum obtained by the APi-ToF-MS when the UV lamp was turned on, after the warm up period, to produce haze analogs from 2 ppmv O_2/0.1% CO_2/0.1% CH_4 in N_2. Positive ions are colored according to chemical composition. The chemical compositions and the mass range of the positive ions measured during haze formation of the 2 ppmv O_2 haze analog is representative of the positive ions formed during 0 and 20 ppmv O_2 haze analog production, as well. For these three analogs, the majority of positive ion signal is due to ions that contain carbon, hydrogen and nitrogen, or carbon, hydrogen, nitrogen and oxygen, fitting with the proton affinity trends illustrated in Table 5.1. In addition, the higher m/z mass peaks labeled unidentified were unable to be identified and assigned a chemical formula because there were multiple ($\geq$3) overlapping peaks at the same mass that could not be separated from each other.

The empirical formula of the organic positive ions that form during haze analog production with 20 ppmv precursor O_2 is plotted versus their mass to charge in Figure 5.13, which is also representative of the organic positive ion backbones of the 0 and 2 ppmv O_2 analogs. As m/z increases, the ions, which first have one nitrogen atom, now have one nitrogen atom and one oxygen atom. Then, the larger positive ions have two nitrogen atoms and one oxygen atom. Lastly, the largest positive ions that were chemically identified have two nitrogen atoms and two oxygen atoms. The different positive ion backbones are most intense in isolated m/z regions, where as ions become more massive, they increase systematically

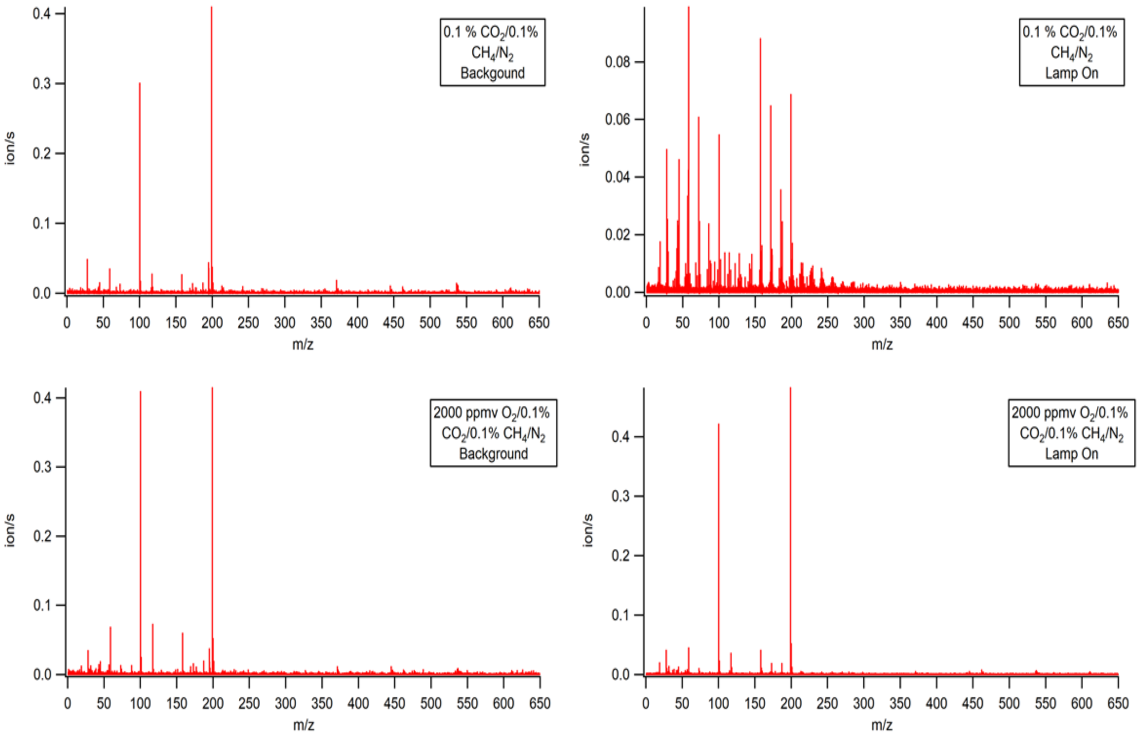

Figure 5.11: Example background and lamp on raw mass spectra of the positive ions that formed with the addition of no precursor O_2 and with 2000 ppmv O_2. The mass spectra of the positive ions formed with no O_2 is representative of the positive ions formed with 2 and 20 ppmv O_2, and the mass spectra of the positive ions formed with 2000 ppmv O_2 is representative of the positive ions formed with 200 ppmv O_2, as well.

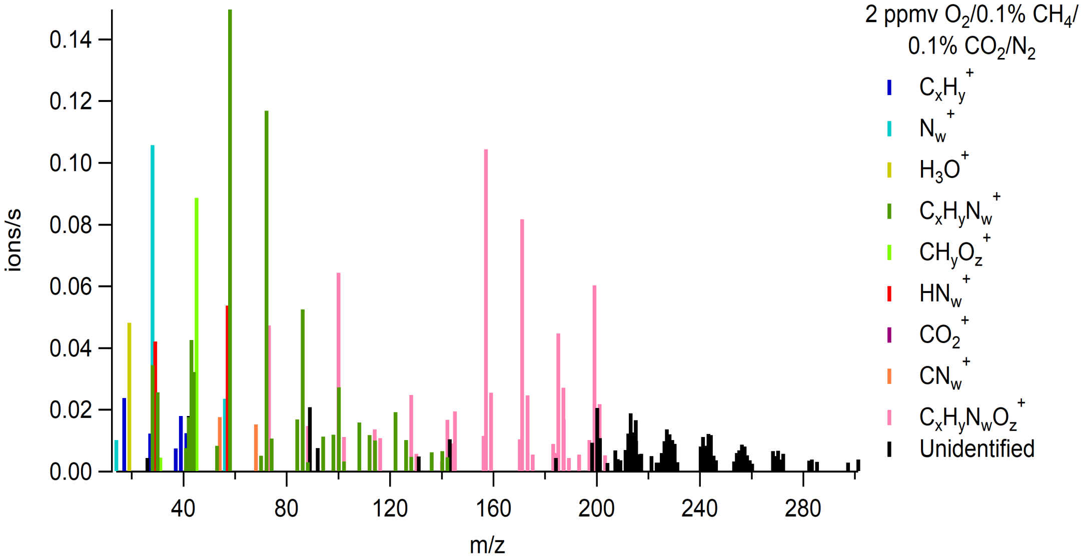

Figure 5.12: An example mass spectrum of the positive ions detected during haze analog formation with 2 ppmv O_2/0.1% CO_2/0.1% CH_4 in N_2.

in proton affinity. This could allude to the neutral species that form during haze analog production. It is possible that larger mass species with one nitrogen atom or one nitrogen atom and one oxygen atom are still formed during haze analog production but are no longer positive ions due to their lower proton affinity.

For the three early Earth analogs produced with $O_2 \leq 20$ ppmv, the signal-weighted average H/C, N/C and O/C molar ratios, along with the signal-weighted RDBE, were calculated. Figure 5.14 displays the molar ratios and RDBE as a function of precursor O_2 concentration. The positive ions for each of the three analogs have a larger H/C molar ratio, which suggests that the ions are saturated. This is confirmed by a lower RDBE, as well. In addition, the N/C and O/C molar ratios for the positive ions are similar for the three analogs. Compared to the negative ions, the positive ions are more saturated and contain less nitrogen and oxygen.

5.3.3 Implications for Early Earth

While the ion chemistry in this study is likely initiated by a combination of ionization by the lamp and background ionization sources, like galactic cosmic rays and ground-based radiation, this type of ion chemistry could also be relevant for the early Earth. While the UV lamp used in this study resulted in a chamber flux higher than what was likely to have existed during the early Earth (Trainer et al., 2006; Claire et al., 2012; Ranjan and Sasselov, 2016), the range of wavelengths emitted by the younger sun would still have included wavelengths with sufficient energy to ionize atmospheric species. Moreover, in current Earth's atmosphere, Lyman-α penetrates into the mesosphere where it can ionize species with lower ionization energies, such as NO (Shuman et al., 2015). Similar ionization pathways where wavelengths with sufficient ionization energies can penetrate past the upper atmosphere could likely have existed during the early Earth, especially since the younger sun had a larger UV flux than present (Claire et al., 2012). In addition, since Titan's haze formation begins in the upper atmosphere, if the same pathway for haze formation occurred

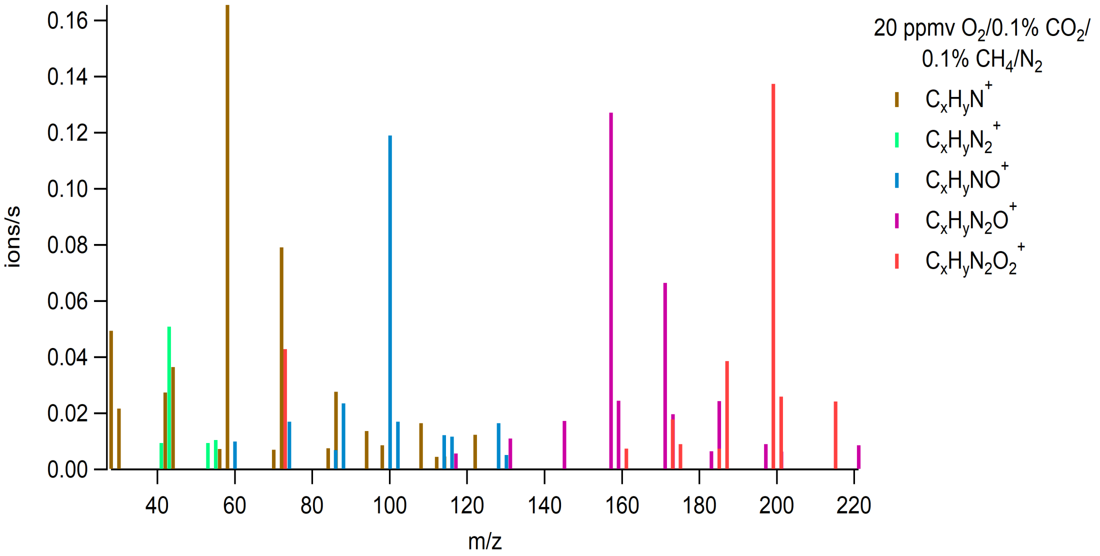

Figure 5.13: The positive organic ions detected during haze analog formation with 20 ppmv O_2/0.1% CO_2/0.1% CH_4 in N_2. As *m/z* increases, the ions increase in oxygen and nitrogen in order of increasing proton affinity.

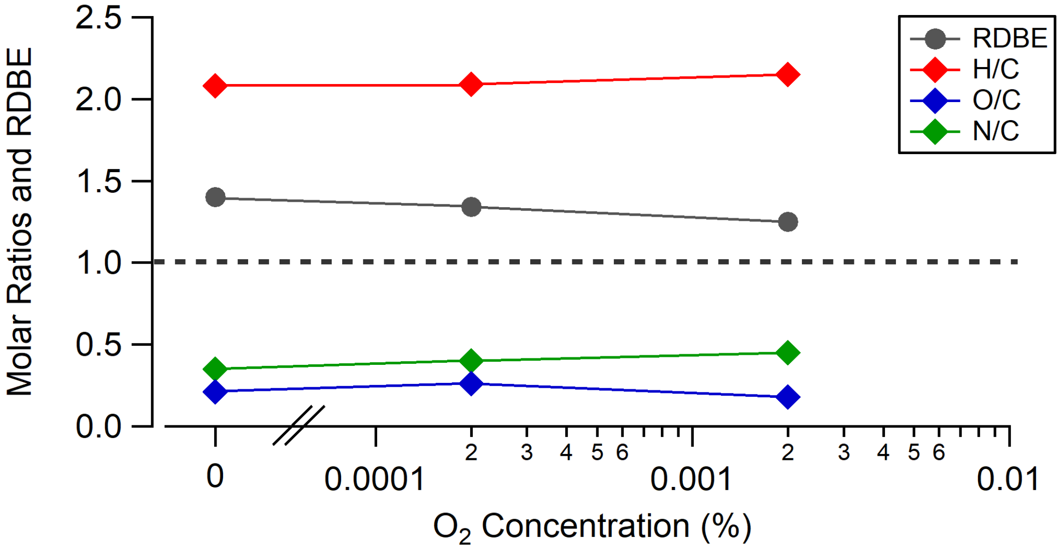

Figure 5.14: Signal-weighted average molar ratios and RDBE of the positive ions produced during haze analog production.

in the early Earth's atmosphere, the stronger ionizing wavelengths the upper atmosphere was exposed to is important to consider, as well.

Along with ionization by solar UV photons, galactic cosmic rays would have been another ionization source present during the early Earth. The galactic cosmic rays could have penetrated down to Earth's surface and ionized the major species and atoms throughout the early Earth's atmosphere, like it does today (Grupen, 2005; Shuman et al., 2015). However, a source of ionization that likely influenced this study but not the atmosphere of the early Earth is ground-based radiation, possibly in the form of gamma rays. Various locations in the world have been monitored for terrestrial gamma rays (Alatise et al., 2008; Moreno et al., 2008; Murty and Karunakara, 2008; Baykara and Doğru, 2009; Lee et al., 2009; Maharana et al., 2010). If gamma rays are present in the laboratory, they cannot be removed and would penetrate the UV reaction cell. However, it is likely that most of the background ionization comes from the galactic cosmic rays due to the higher elevation of Boulder, CO.

Since the ions that were measured in this study could have existed in the atmosphere of the early Earth, it is also necessary to look at the implications of these species. The types of ions formed in this study may have astrobiological significance. The negative ions transition from mostly organic nitrogen, as CNO^-, to inorganic nitrogen, as NO_3^-, with increasing precursor O_2. If CNO^- is cyanate, the cyanate ion has been proposed to have prebiotic significance, where CNO^- can form the nucleic base cytosine by reactions with cyanoacetylene (Ferris et al., 1968). The anion of cyanoacetylene (C_3N^-) has been measured by the APi-ToF-MS in this study's experiments that produced early Earth analogs with 0 - 20 ppmv precursor O_2. This suggests that both ions could have been present in the early Earth's atmosphere together, which could have led to cytosine formation. In addition, Yamagata (1999) reported that adenosine-5'-monophosphate (AMP) can form adenosine-5'-diphosphate (ADP) which then forms adenosine-5'-triphosphate (ATP) all by spontaneous phosphorylation when the reactions occur in an aqueous solution containing calcium phosphate and cyanate. Moreover, the spontaneous phosphorylation only occurs when cyanate is present in the solution. Therefore, if cyanate dissolved in atmospheric water vapor or made its way to the surface and dissolved in liquid water it could have assisted in the production of ATP, which could have been crucial for early life since cells need ATP for basic functions.

In addition to CNO^- having potential significance to prebiotic chemistry, the transition to NO_3^- also has relevance to early life and evolution. Life needs nitrogen, but cannot directly use atmospheric N_2. To overcome this, there are biotic and abiotic sources that "fix" nitrogen, turning N_2 into nitrogen containing nutrients. Nitrate is one of the key nutrients for life that is formed by both biotic and abiotic nitrogen fixation. Nitrogen-fixing bacteria are a biotic source of nitrate from nitrogen fixation, whereas lightening is an abiotic source of nitrate from nitrogen fixation. During the early Earth, the exact sources of nitrogen fixation is difficult to confirm. Lightning could have been an important source of nitrogen fixation during the earliest times in Earth's history (Yung and McElroy, 1979; Kasting and Walker, 1981; Kasting, 1990; Navarro-Gonzaléz et al., 2001). However, there is also evidence that biotic nitrogen fixing existed since 3.5 Ga (Beaumont and Robert, 1999). Based on the results from the current study, nitrate produced during haze formation may be a previously unexplored abiotic nitrogen fixation pathway. Ultimately, the transition between CNO^- and NO_3^- could be indicative of the chemistry and possible life that could have existed during the early Earth in times of none/limited O_2 and in times of significant O_2.

In addition, the transition in the ion chemistry also overlaps with the decrease in haze particle production and is shown in Figure 5.15. When $O_2 \leq 20$ ppmv is used during haze analog formation, an organic haze forms. If there were living organisms at this time as well, it is possible that such an atmospheric haze could have protected organisms from the damaging UV light (Arney et al., 2016). However, once 200 ppmv O_2 is used to produced haze analogs, haze production greatly decreases and would provide less UV shielding for life at the surface.

Using the precursor O_2 x-axis in Figure 5.15 as a time scale, with molecular oxygen increasing over the course of Earth's history, Figure 5.15 shows a possible early Earth scenario

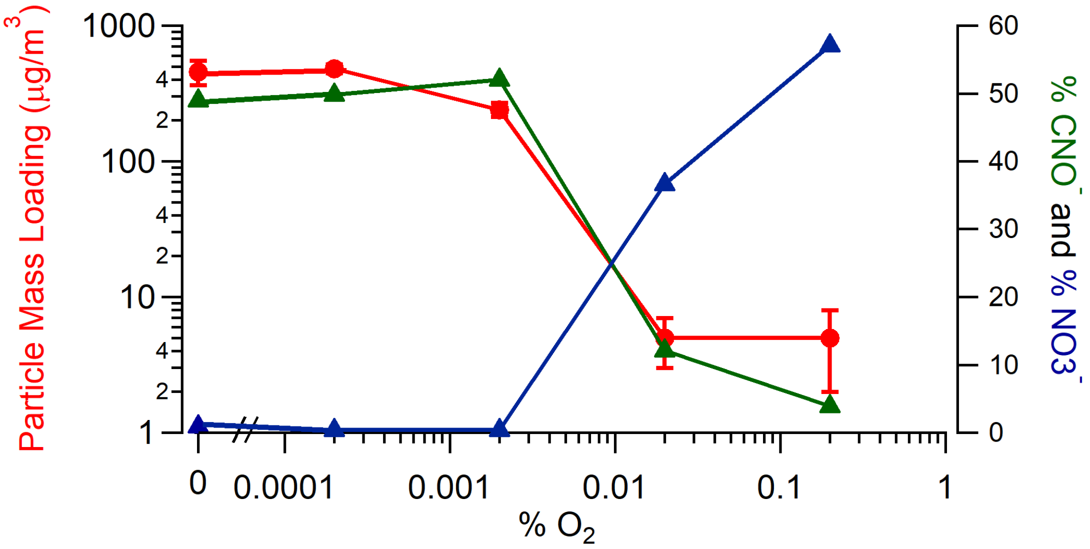

Figure 5.15: Transition between organic and inorganic nitrogen-containing ions (CNO^- to NO_3^-), along with haze formation, as a function of precursor O_2. Using precursor O_2 as a reference to time in Earth's history allows for the comparison of the different types of possible chemistry that could have occurred during different times in Earth's history based on atmospheric O_2 concentrations.

where atmospheric chemistry resulted in the formation of prebiotic molecules and then nutrients to support life, along with a protective UV shielding haze. However, as the early Earth's atmosphere continued to increase in oxygen, haze mass loading decreases, limiting an effective haze UV shield. At the same time, though, ozone would have increased in abundance, where Goldblatt et al. (2006) states that once atmospheric O_2 is greater than 2 x 10^{-5} present atmospheric level (PAL) (4.2 ppm), an ozone layer will begin to form. Therefore, it is possible that once the haze layer is too thin to provide UV shielding, an ozone layer already exists. Since the current study cannot measure neutral species, ozone was not measured as a function of precursor O_2. In addition, O_3^- is very unstable so it is very unlikely to be detected and measured by the APi-ToF-MS. However, CO_3^- was measured for the analogs produced with 2000 ppmv O_2. In current Earth's atmosphere, CO_3^- forms by reactions of O^-, O_4^- and CO_4^- with O_3 (Shuman et al., 2015). Therefore, even though the neutrals were not measured, O_3 is likely produced during haze analogs formation with 2000 ppmv O_2. It is also likely that ozone is produced in this study during haze analog formation using 20 and 200 ppmv O_2 as well since they are both O_2 concentrations greater than 2 x 10^{-5} PAL.

5.4 Conclusion

Negative and positive ions that form during early Earth haze analog production as a function of precursor O_2 were measured. Negative ion chemical compositions become more oxidized and saturated with precursor O_2 and the positive ions are more saturated than the negative ions. Moreover, similar to what is observed in Titan's atmosphere, ion-neutral chemistry is possibly related to early Earth haze analog formation, where there is potentially an inverse relationship between ion signal and haze particle mass loading. Additionally, negative ion composition and the ability to form a thick organic haze is related to the amount of precursor O_2, with a transition observed between 20 and 200 ppmv precursor O_2. The transition from CNO^- to NO_3^- with increasing O_2, which occurs simultaneously with the transition in haze formation, could have been important for the evolution of early life, with atmospheric CNO^-

being an active participant in prebiotic chemistry and NO_3^- being a potential source of fixed nitrogen.

6 Stable Isotope Fractionation In Titan Aerosol Formation

6.1 Introduction

Stable isotope ratio measurements are a powerful tool used to understand both ancient and modern planetary processes. Instruments on the Cassini-Huygens spacecraft along with ground-based observations have measured several isotope pairs, including $^{12}C/^{13}C$ and $^{14}N/^{15}N$, in Titan's atmosphere (Bézard et al., 2014). This includes isotopic measurements of the major atmospheric species, CH_4 and N_2, along with HCN, HC_3N, C_2H_2, C_2H_6 and C_4H_2, where the carbon isotope ratio is similar to the protosolar value and the nitrogen fractionation is enriched (Marten et al., 2002; Gurwell, 2004; Waite Jr. et al., 2005; Vinatier et al., 2007a; Nixon et al., 2008, 2012; Jennings et al., 2008, 2009; Jolly et al., 2010; Niemann et al., 2010; Courtin et al., 2011; Mandt et al., 2012). However, the isotopic composition of Titan's organic aerosol has not been measured and therefore the effect of aerosol formation as an isotopic fractionation pathway in Titan's atmosphere has not been considered.

Laboratory studies have measured the carbon and/or nitrogen isotopic composition of Titan aerosol analogs (Nguyen et al., 2007, 2008; Kuga et al., 2014; Sebree et al., 2016). Sebree et al. (2016) found that the carbon isotopic composition of photochemical organic bulk aerosol analogs are more enriched in ^{13}C, and the degree of enrichment varies with precursor CH_4 concentration. This enrichment in the aerosol analogs is opposite of what is predicted for photochemical products by the kinetic isotope effect. Additionally, both Kuga et al. (2014) and Sebree et al. (2016) found that the nitrogen fractionation in the organic aerosol analogs is opposite of what is observed in Titan's atmospheric N_2 and HCN, with the aerosol analogs being a light nitrogen sink. Similar to the carbon isotopic fractionation, the degree of nitrogen isotopic depletion also varies with precursor CH_4 concentration. The isotopic composition of bulk photochemical aerosol is summarized in Figure 6.1 and adapted from Sebree et al. (2016). The carbon and nitrogen stable isotopes (δ) are reported in per

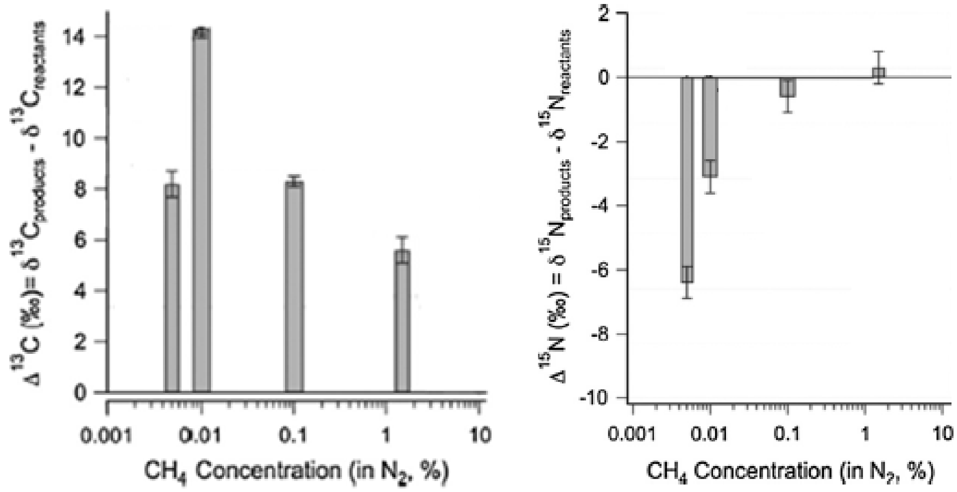

Figure 6.1: Carbon and nitrogen isotopic composition of bulk photochemical aerosol. Photochemical aerosol is a heavy carbon and light nitrogen sink. In addition, the carbon and nitrogen isotopic fractionation varies with precursor CH_4 concentration.

mil (‰) as

$$\delta = (\frac{\mathrm{R}_{\mathrm{sample}}}{\mathrm{R}_{\mathrm{standard}}} - 1) \times 1000 \tag{10}$$

where $\mathrm{R}_{\mathrm{sample}}$ is the heavy to light isotope ratio of the sample (^{13}C/^{12}C or ^{15}N/^{14}N) and $\mathrm{R}_{\mathrm{standard}}$ is the heavy to light isotope ratio of the Vienna Pee Dee Belemnite (VPDB) standard. Δ^{13}C and Δ^{15}N represents the fractionation of the aerosol compared to the initial isotopic fractionation of the precursor CH_4 and N_2, where $\Delta^{13}\mathrm{C} = \delta^{13}\mathrm{C}_{\mathrm{products}}$ - $\delta^{13}\mathrm{C}_{\mathrm{reactants}}$ and $\Delta^{15}\mathrm{N} = \delta^{15}\mathrm{N}_{\mathrm{products}}$ - $\delta^{15}\mathrm{N}_{\mathrm{reactants}}$.

Because the aerosol is enriched with the heavier isotope of carbon, the light carbon isotope sink during haze analog formation is unknown. Here the gas-phase during photochemical aerosol analog production, using 5% CH_4 in N_2, is monitored as a function of reaction time. In the recirculation system described in Chapter 2.2, the isotopic composition of carbon within the gas-phase products is measured as the CH_4 reservoir is depleted. This allows for the monitoring of the isotopic fractionation pathway during photochemical aerosol analog formation. Using gas chromatography mass spectrometry (GC-MS; Chapter 2.7) the gas-phase products are characterized and quantified, and a gas chromatograph coupled to an isotope ratio mass spectrometer was used to measure the isotopic composition of the gas-phase. With the current GC column and temperature programs, only the carbon isotopic composition of CH_4 and C_2H_6 can be measured.

6.2 Experimental

6.2.1 Gas Chromatography-Isotope Ratio Mass Spectrometry

To measure the carbon isotopic composition of the source CH_4 and evolved C_2H_6 a Thermo Scientific Trace Ultra GC Isolink with a Carboxen 1006 PLOT column (Supelco) coupled to a Thermo Scientific Delta V isotope ratio mass spectrometer (IRMS) was used. Gas chromatography with a flame ionization detector is used before the IRMS to separate the gas-phase species to allow for individual isotopic composition measurements for each gas. The

GC inlet temperature was 150°C, and two different GC temperature programs were used to measure the isotopic composition of CH_4 and C_2H_6 and are shown in Figure 6.2a and Figure 6.2b, respectively. Since the CH_4 and C_2H_6 require different GC temperature programs, two separate extractions from the gas sampling port in the recirculation system (Chapter 2.2) are necessary. The extraction for CH_4 analysis requires 100 μL and the extraction for C_2H_6 analysis requires 500 μL. The two extractions are done one after another, but the first gas sample is injected for the CH_4 analysis and then the second gas sample is injected for the C_2H_6 analysis. Therefore, the first injection and second injection are separated by the length of CH_4 GC temperature program. Due to the low signal to noise of the propane peak with the current methods, the isotopic composition of propane could not be measured.

After the GC separates the gas species, they flow to the IRMS combustion system. First the gases are oxidized, where the carbon is oxidized to CO_2, the nitrogen is oxidized to NO_x and the hydrogen is oxidized to H_2O. The oxidized carbon, nitrogen and hydrogen then flow to a reducing oven where the NO_x is reduced to N_2. Next, the H_2O is removed and both CO_2 and N_2 flow to the IRMS detector. In the study presented here, only the carbon isotopic composition was measured. Three Faraday cups catch and record the ion current of four isotopologues of CO_2: $^{12}C^{16}O^{16}O$ ($m/z = 44$), $^{13}C^{16}O^{16}O$ ($m/z = 45$), $^{12}C^{17}O^{16}O$ ($m/z = 45$), $^{12}C^{18}O^{16}O$ ($m/z = 46$). The ion current is then converted into a relative isotopic abundance and compared to a Vienna Pee Dee Belemnite (VPDB) standard for isotopic fractionation.

6.2.2 Gas Sampling and Measurements

The recirculation system is filled with the precursor gas mix and before turning on the UV lamp, background measurements of the gas composition is measured by the GC-MS (Chapter 2.7). In addition, the background isotopic composition of the precursor CH_4 is measured by the GC-IRMS. The CH_4 background measured with the GC-IRMS is done at least three times in order to ensure a precise isotopic composition measurement of CH_4. Once the UV

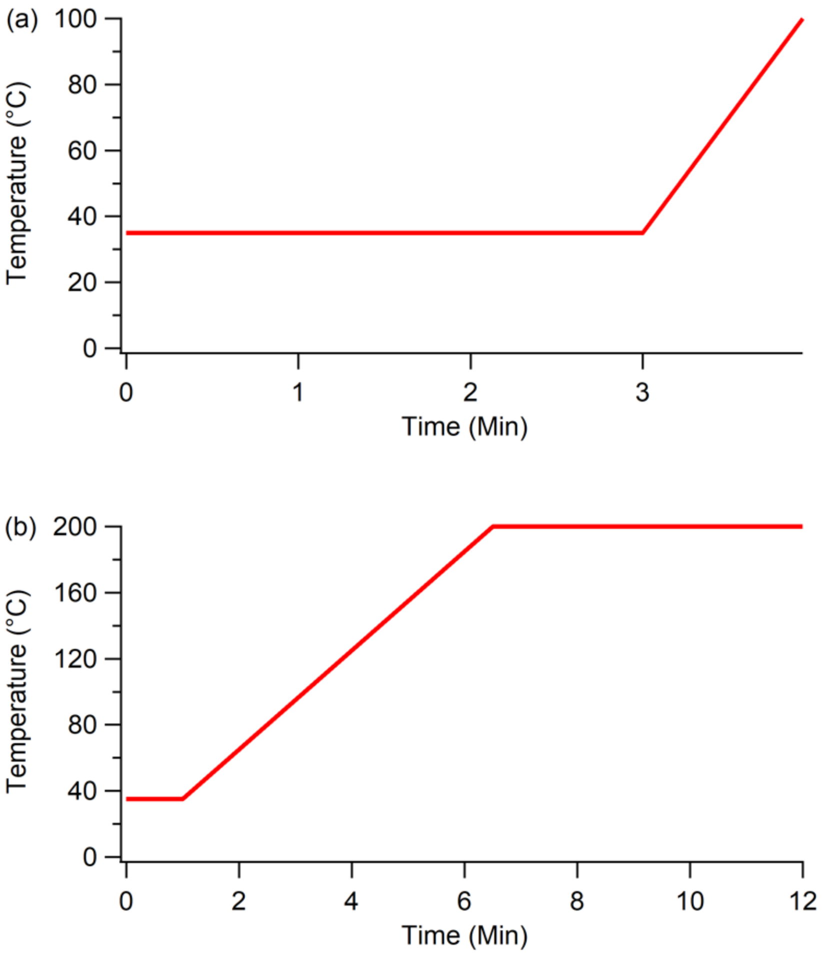

Figure 6.2: GC temperature programs for (a)CH_4 and (b)C_2H_6 during GC-IRMS measurements.

lamp is turned on, GC-IRMS measurements are done once an hour. GC-MS measurements are also done once an hour, but are staggered with the GC-IRMS extractions so that the gases are extracted for the GC-MS thirty minutes after the GC-IRMS extractions. For GC-MS measurements, 300 μL gas samples are extracted.

6.3 Preliminary Results and Discussion

This project is still ongoing so only preliminary results are described here. Using the GC-MS, the consumed CH_4 and evolved secondary products are characterized. Standards were used to quantify the alkane species, whereas the measured nitriles and acetylene are only reported as a peak area (A.U.). Figure 6.3 includes the concentration in ppm (a) and peak area (b) of the GC-MS detected gas species measured during Titan photochemical haze analog formation. Time gaps in the data exist because experiments went on for over 24 hours, including one experiment that measured the isotopic and chemical composition of the gases for over 50 hours.

Initially, all of the detected secondary gases increase in concentration (or intensity), shown in Figure 6.3a and Figure 6.3b as both the concentration over the course of the whole experiment and also zoomed in on the first six hours of the experiment. After a set amount of time that is currently unknown, the concentration of each secondary gas begins to decrease as the secondary products are consumed to produce further products, possibly including haze particles. Assuming the concentration of the secondary alkanes all decrease at hour 6, the alkanes shown in Figure 6.3a exponentially decrease in concentration at increasing rates with increasing carbon number. Where the exponential fit of a line is $y = y0 + A \times \exp(-\tau x)$, τ increases from C_2H_6, C_3H_8 to C_4H_{10} as 0.003, 0.097 and 0.113, respectively. In addition, while most species appear to reach a steady state by hour 44.5, the acetylene concentration decreases to below the GC-MS detection limit (hour 21.5). The detection of acetylene in these experiments may be indicative of the photochemical haze formation pathway since acetylene is believed to have a role in the formation of the precursor gases that make haze

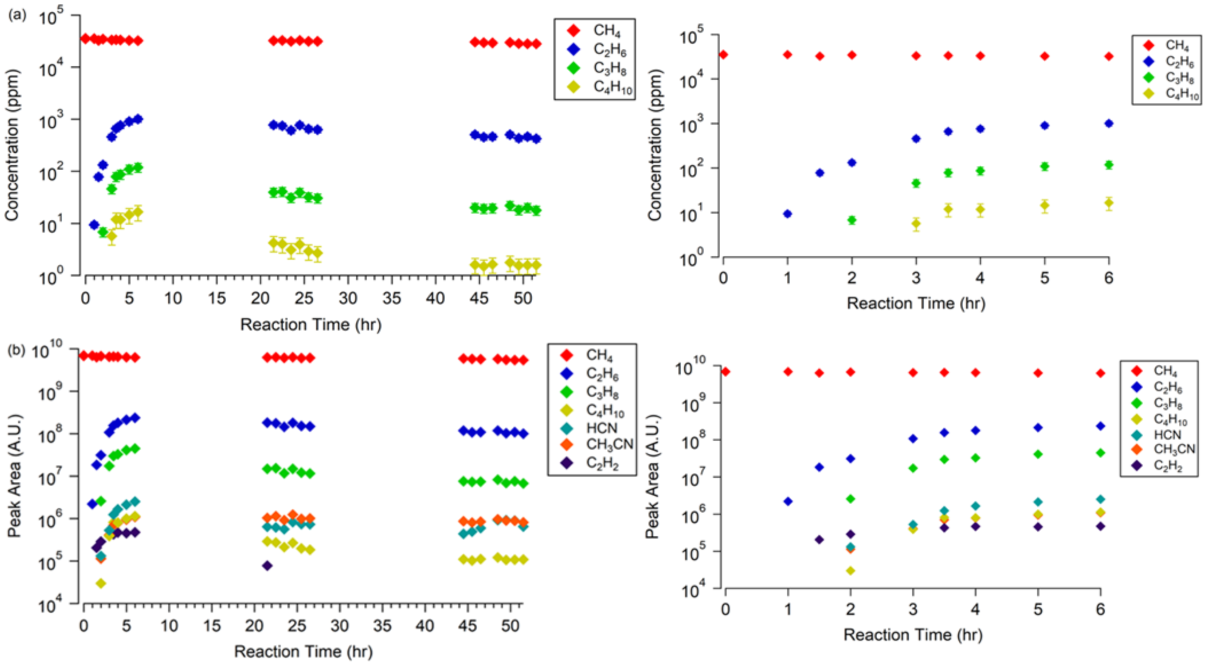

Figure 6.3: Concentrations and peak areas for the gases measured by the GC-MS.

particles in Titan's atmosphere (Tran et al., 2005). Based on the concentrations of the alkanes determined by the GC-MS, carbon isotopic measurements can be done for CH_4, C_2H_6 and possibly C_3H_8.

Using Equation 10, the carbon isotopic fractionation (δ^{13}C) of CH_4 and C_2H_6 compared to VPDB is shown in Figure 6.4, where $R_{\text{standard}} = 0.0112594$. Also shown in Figure 6.4 is the light to heavy carbon isotope ratio ($^{12}C/^{13}C$) for both CH_4 and C_2H_6 calculated based on Equation 10. Since the isotope measurements were done over three different experiment runs, measurements from different experiments are shown as different shapes. The solid shapes are the δ^{13}C values and the outlined shapes are the light to heavy carbon isotope ratios. Both CH_4 and C_2H_6 become more enriched in ^{13}C with the reaction progression. Moreover, the $^{12}C/^{13}C$ ratio values measured in the recirculation experiment for CH_4 and C_2H_6 are similar to the $^{12}C/^{13}C$ ratios measured for these gases in Titan's atmosphere by instruments on the Huygens Probe (Niemann et al., 2010) and the Cassini Orbiter (Nixon et al., 2008, 2012).

While the previous study by Sebree et al. (2016) found that photochemical haze particles produced in a flow system are enriched in ^{13}C, it is unknown if the haze particles produced in the recirculation system are also enriched. Therefore, the light carbon sink is currently unknown. In addition, while the products appear to reach a steady-state, their carbon isotopic composition continues to change. In order to achieve mass balance something new must be forming that becomes more isotopically depleted, possibly including the unmeasured secondary gases or haze particles.

Figure 6.5 shows the enrichment in ^{13}C relative to the initial methane in the gas mixtures as Δ^{13}C ($\Delta^{13}C = \delta^{13}C_{\text{products}}$ - $\delta^{13}C_{\text{reactants}}$). Since multiple experiment runs were done, the different shapes in Figure 6.5 represent the different experiments. A dashed line at zero has been included since $\Delta > 0$ means the molecule is enriched in the heavier isotope and $\Delta < 0$ means the molecule is depleted in the heavier isotope. Both gases become more enriched in ^{13}C relative to the initial CH_4. Initially, C_2H_6 is isotopically lighter than CH_4.

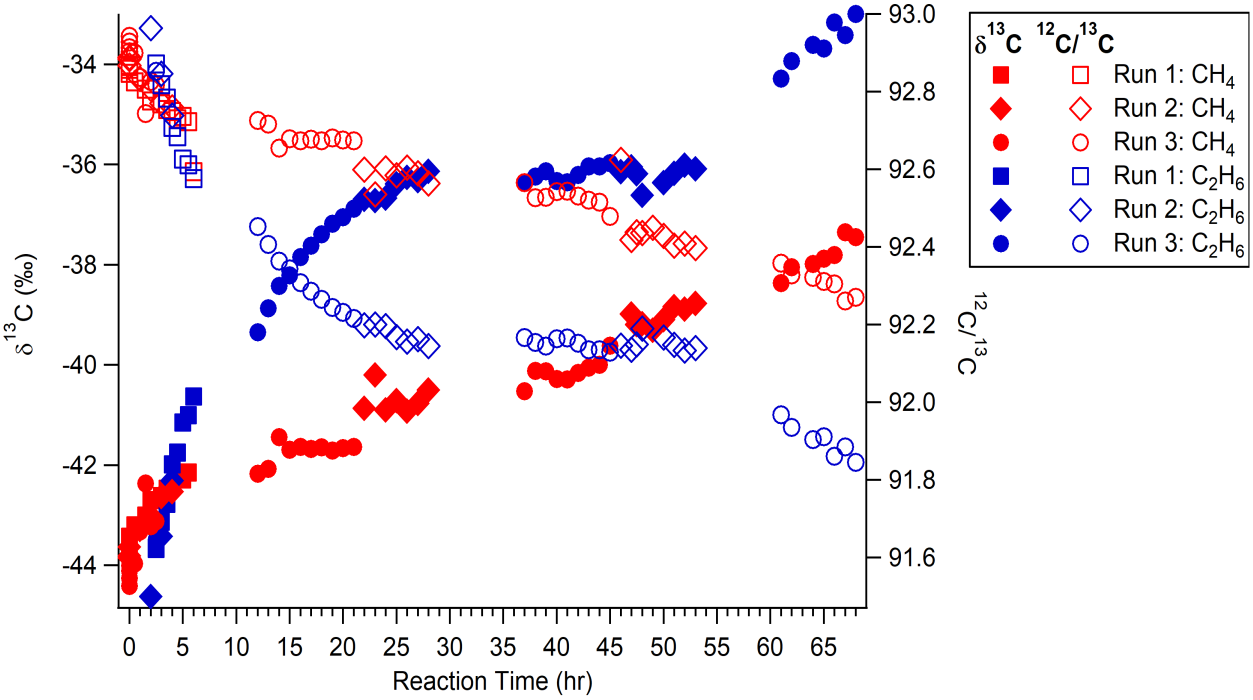

Figure 6.4: Carbon isotopic fractionation relative to VPDB (solid shapes) and the $^{12}C/^{13}C$ ratios (outline shapes) of CH_4 and C_2H_6. Both CH_4 and C_2H_6 become more enriched with reaction time. In addition, the $^{12}C/^{13}C$ ratios of CH_4 and C_2H_6 are similar to those measured in Titan's atmosphere by instruments on the Huygens Probe and the Cassini Orbiter.

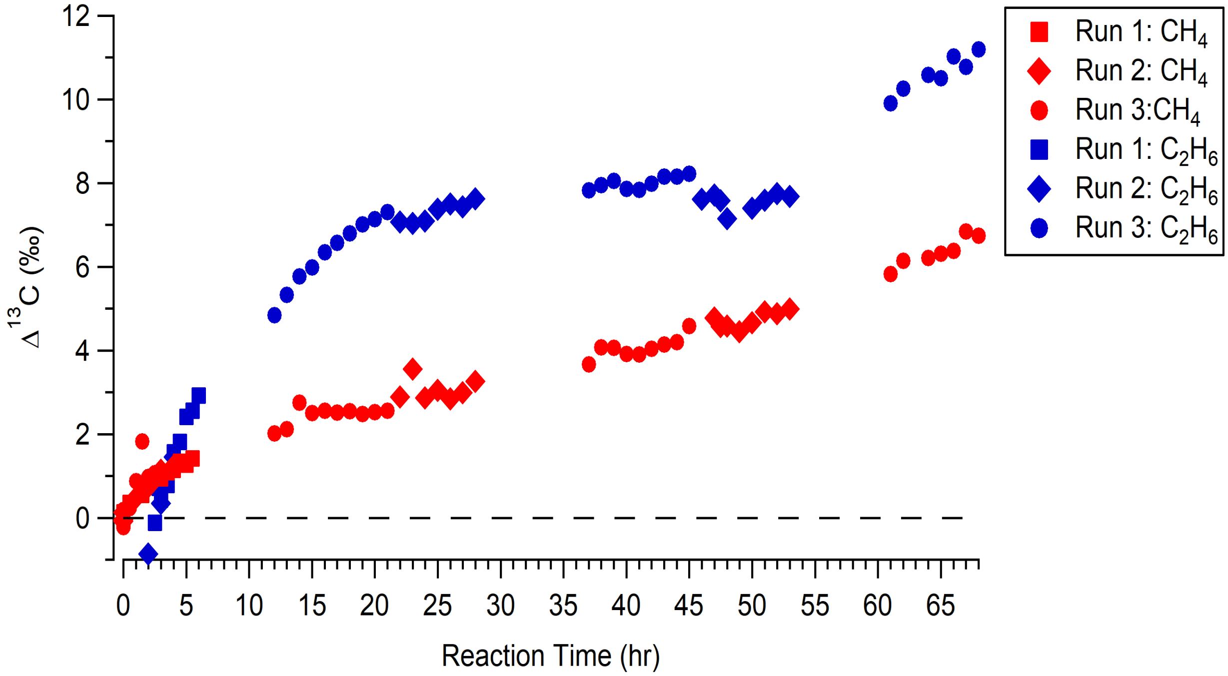

Figure 6.5: Carbon isotopic fractionation of CH_4 and C_2H_6 relative to the initial CH_4. The enrichment of C_2H_6 occurs faster than the enrichment of CH_4.

Being lighter than the source of methane is expected if C_2H_6 forms by reactions of CH_4. Eventually, however, the enrichment of ^{13}C in C_2H_6 occurs faster than the enrichment of CH_4. The heavier isotopic composition of C_2H_6 compared to the source CH_4 potentially points to a different or additional reaction pathway(s) either producing or consuming the CH_4, or possibly a different reaction pathway beyond reactions of CH_4 that results in the production of C_2H_6.

Since the light carbon sink(s) are still unknown, future experiments will be performed to measure the carbon isotopic fractionation of the evolved C_3H_8. To do this, new columns and temperature programs will be used to enhance signal to noise. In addition, if the other evolved gases can be measured with the IRMS, having the carbon isotopic composition of each gas produced during haze analog formation will help with identifying the sink(s) of the ^{12}C. To capture the less abundant gases, including C_3H_8, a stainless steel enrichment cell will be added to the recirculation system. This extra volume will allow for more molecules of the less abundant gases to be measured by the IRMS. Also, simple model calculations will be used to estimate the magnitude of the carbon fractionation and the amount of the "missing" light carbon. This will be done by calculating the Kinetic Isotope Effect (KIE) Fractionation Factor, α, where $\alpha = \mathrm{K_l}/\mathrm{K_h}$. Here $\mathrm{K_l}$ is the reaction rate constants of the reactions with the light isotope and $\mathrm{K_h}$ is the reaction rate constants of the reactions with the heavy isotopes. Future studies will also include aromatic precursors such as benzene and pyridine as reactants in the gas mixture. By adding pyridine, the nitrogen incorporation is expected to increase, so these studies will also measure the isotopic fractionation of the nitrogen in the gas-phase products.

7 Conclusions and Future Directions

7.1 Conclusions

The chemical, physical and optical properties of planetary organic haze analogs, along with the ion chemistry during haze formation, was examined in this thesis. The hazes simulated in these studies were produced by spark discharge and UV light, and were analogs of Titan and the early Earth. The findings of these studies are briefly outlined.

Titan haze analogs were produced by the spark discharge of different amounts of CH_4 in N_2. The complex refractive indices at 405 and 532 nm and corresponding chemical composition was determined. The imaginary refractive index had a V-shape trend which corresponded to particle composition. Particles with more aromatic compounds and nitrogen containing compounds had larger imaginary refractive indices. In addition, as particles were produced with increasing amount of CH_4, less nitrogen incorporation into the particles was observed. While the real refractive indices were similar to most previous studies, the magnitude of the imaginary refractive indices were lower than those of the commonly used refractive indices by Khare et al. (1984). The lower imaginary refractive indices could impact modeled planetary processes that require the complex refractive index of haze as an input parameter.

Early Earth haze analogs were produce by UV excitation of 0, 2, 20, 200 and 2000 ppmv O_2, 0.1% CO_2 and 0.1% CH_4 in N_2. The particle effective density, mass loading and complex refractive indices at 405 nm were determined for the particles that were produced in sufficient abundance for the measurement techniques. Haze particles can still form in the presence of molecular oxygen. As particles are produced with increasing amounts of molecular O_2, the particles become more oxidized and have increasing densities. With increasing amounts of precursor O_2, the haze particle mass loading decreases non-linearly. However, even with 200 and 2000 ppmv O_2, small amounts of haze still forms. In addition, photochemical particles produced in the presence of oxygen were found to be non-absorbing, whereas photochemical particles produced with CH_4 in N_2 were found to be slightly absorbing. A light-scattering haze could have influenced the climate of the Archean Earth, reducing the radiation that reaches the surface.

During the production of the early Earth haze analogs, ambient ions that formed during haze production were measured. Ion signal and particle mass loading are possibly inversely related, suggesting that ion-neutral chemistry could be important for early Earth haze formation. In addition, the negative ions become more oxidized and saturated with increasing precursor O_2 and the positive ions are more saturated than the negative ions. Lastly, a transition was observed in the nitrogen containing negative ions between 20 and 200 ppmv precursor O_2 where the nitrogen containing negative ions changed from being mostly composed of organic nitrogen, as CNO^-, to being mostly composed of inorganic nitrogen, as NO_3^-. This transition also overlaps with when haze analog production decreases. It is possible that the transition from CNO^- to NO_3^- could have relevance for the evolution of life. Haze production during the early Earth could have been an abiotic source for both CNO^-, an important ion for prebiotic chemistry, and NO_3^-, a fixed nitrogen nutrient.

Lastly, Titan haze analogs were produced by UV excitation of 5% CH_4 in N_2 in a closed recirculation system. The neutral gases produced during haze formation were characterized and quantified, and the isotopic composition of CH_4 and C_2H_6 was measured. While the light carbon sink in the system remains unknown, both CH_4 and C_2H_6 become enriched in ^{13}C. In addition, while C_2H_6 is initially lighter than the source CH_4, which is what is expected if C_2H_6 forms by reactions of CH_4, the carbon isotopic fractionation of C_2H_6 increases faster than that of CH_4. This suggests that there is a different or additional reaction pathway(s) either producing or consuming CH_4.

7.2 Future Work

For the early Earth studies detailed in Chapter 4, the PASCaRD system can measure extinction and absorption at both 405 and 532 nm. Since only the complex refractive indices were report at 405 nm, they could also be measured at 532 nm. In addition, the ion chemistry during early Earth haze analog production study described in Chapter 5 could be greatly expanded. First, the APi-ToF-MS can be interfaced with a chemical ionization (CI) source. By including CI to the APi-ToF-MS inlet, neutral gases that are produced during haze formation will get ionized upon entering the instrument and thus can now be detected. Obtaining the chemical information of the neutral gas species will enhance the understanding of early Earth haze formation and the ion-neutral chemistry. Measuring neutrals like O_3 would also put this chemistry in a geological context, as well. In addition, all of the early Earth experiments presented in this thesis could be redone with a CO_2/CH_4 ratio expanding from 1:10 to 10:1 to increase the relevance to different times in the early Earth's history. Lastly, to determine if the ion signal and aerosol mass loading are in fact inversely related, the ion loss rate to the haze particles needs to be calculated.

Bibliography

Aiken, A.C., DeCarlo, P.F., Kroll, J.H., Worsnop, D.R., Huffman, J.A., Docherty, K.S., Ulbrich, I.M., Mohr, C., Kimmel, J.R., Sueper, D., Sun, Y., Zhang, Q., Trimborn, A., Northway, M., Ziemann, P.J., Canagaratna, M.R., Onasch, T.B., Alfarro, M.R., Prevot, A.S.H., Dommen, J., duplissy, J., Metzger, A., Baltensperger, U., Jimenez, J.L., 2008. O/C and OM/OC ratios of primary, secondary, and ambient organic aerosols with high-resolution time-of-flight aerosol mass spectrometry. *Environ. Sci. Technol.* 42, 4478–4485.

Alatise, O.O., Babalola, I.A., Olowofela, J.A., 2008. Distribution of some natural gamma-emitting radionuclides in the soils of the coastal areas of Nigeria. *Environ. Radioact.* 99, 1746–1749.

Arney, G., Domagal-Goldman, S.D., Meadows, V.S., Wolf, E.T., Schwieterman, E., Charnay, B., Claire, M., Hébrard, E., Trainer, M.G., 2016. The pale orange dot: The spectrum and habitability of hazy Archean Earth. *Astrobiology* 16, 873–899.

Atkinson, D.B., Radney, J.G., Lum, J., Kolesar, K.R., Cziczo, D.J., Pekour, M.S., Zhang, Q., Setyan, A., Zelenyuk, A., Cappa, C.D., 2015. Aerosol optical hygroscopicity measurements during the 2010 CARES campaign. *Atmos. Chem. Phys.* 15, 4045–4061.

Atreya, S.K., Adams, E.Y., Niemann, H.B., Demick-Montelara, J.E., Owen, T.C., Fulchignoni, M., Ferri, F., Wilson, E.H., 2006. Titan's methane cycle. *Planet. Space Sci.* 54, 1177–1187.

Awramik, S.M., 1992. The oldest records of photosynthesis. *Photosynth. Res.* 33, 75–89.

Bézard, B., Yelle, R.V., Nixon, C.A., 2014. *The composition of Titan's atmosphere.* Cambridge University Press.

Baykara, O., Doğru, M., 2009. Determination of terrestrial gamma, ^{238}u, ^{232}th, ^{40}k in soil along fracture zones. *Radiat. Meas.* 44, 116–121.

Beaumont, V., Robert, F., 1999. Nitrogen isotope ratios of kerogens in Precambrian cherts: a record of the evolution of atmosphere chemistry? *Precambrian Res.* 96, 63–82.

Biemann, K., 2006. Astrochemistry: Complex organic matter in Titans aerosols? *Nature* 444, 6.

Bohren, C. F., Huffman, D.R., 2004. *Absorption and Scattering of Light by Small Particles.* Wiley-VCH Weinheim, Germany.

Brassé, C., Muñoz, O., Coll, P., Raulin, F., 2015. Optical constants of Titan aerosols and their tholins analogs: Experimental results and modeling/observational data. *Planet. Space Sci.* 109-110, 159–174.

Brown, R.H., Lebreton, J.-P., Waite, J. H., 2009. *Titan from Cassini-Huygens;.* Springer: New York.

Canagaratna, M.R., Jayne, J.T., Jimenez, J.L., Allan, J.D., Alfarra, M.R., Zhang, Q., Onasch, T.B., Drewnick, F., Coe, H., Middlebrook, A., Delia, A., Williams, L.R., Trimborn, A.M., Northway, M.J., DeCarlo, P.F., Kolb, C.E., Davidovits, P., Worsnop, D.R., 2007. Chemical and microphysical characterization of ambient aerosols with the aerodyne aerosol mass spectrometer. *Mass Spectrom. Rev.* 26, 185–222.

Canagaratna, M.R., Jimenez, J.L., Kroll, J.H., Chen, Q., Kessler, S.H., Massoli, P., Hildebrandt Ruiz, L., Fortner, E., Williams, L.R., Wilson, K.R., Surratt, J.D., Donahue, N.M., Jayne, J.T., Worsnop, D.R., 2015. Elemental ratio measurements of organic compounds using aerosol mass spectrometry: characterization, improved calibration, and implications. *Atmos. Chem. Phys.* 15, 253–272.

Cappa, C.D., Kolesar, K.R., Zhang, X., Atkinson, D.B., Pekour, M.S., Zaveri, R.A., Zelenyuk, A., Zhang, Q., 2016. Understanding the optical properties of ambient sub- and supermicron particulate matter: results from the CARES 2010 field study in northern California. *Atmos. Chem. Phys.* 16, 6511–6535.

Chen, F.Z., Wu, C.Y.R., 2004. Temperature-dependent photoabsorption cross sections in the VUV-UV region. l. methane and ethane. *J. Quant. Spectrosc. Radiat. Transfer* 85, 195–209.

Claire, M.W., Sheets, J., Cohen, M., Ribas, I., Meadows, V.S., Catling, D.C., 2012. The evolution of solar flux from 0.1 nm to 160 μm: Quantitative estimates for planetary studies. *Astrophys. J.* 757, 95.

Coates, A.J., Crary, F.J., Lewis, G.R., Young, D.T., Waite Jr., J.H., Sittler Jr., E.C., 2007. Discovery of heavy negative ions in Titans ionosphere. *Geophys. Res. Lett.* 34, L22103.

Coates, A.J., Wellbrock, A., Lewis, G.R., Jones, G.H., Young, D.T., Crary, F.J., Waite, J.H., Johnson, R.E., Hille, T.W., Sittler Jr., E.C., 2010. Negative ions at Titan and Enceladus: recent results. *Faraday Discuss.* 147, 293–305, discussion 379–403.

Courtin, R., Swinyard, B.M., Moreno, R., Fulton, T., Lellouch, E., Rengel, M., Hartogh, P., 2011. First results of Herschel-SPIRE observations of Titan. *Astron. Astrophys.* 536, L2.

Courtin, R., Kim, S.J., Bar-Nun, A., 2015. Three-micron extinction of the Titan haze in the 250-700 km altitude range: Possible evidence of a particle-aging process (research note). *Astron. Astrophys.* 573, A21.

Coustenis, A., Achterberg, R.K., Conrath, B.J., Jennings, D.E., Marten, A., D.,, Gautier Nixon, C.A., Flasar, F.M., Teanby, N.A., Bézard, B., Samuelson, R.E., Carlson, R.C., Lellouch, E., Bjoraker, G.L., Romani, P.N., Taylor, F.W., Irwin, P.G.J., Fouchet, T., Hubert, A., Orton, G.S., Kunde, V.G., Vinatier, S., Mondellini, J., Abba, M.M., Courtin, R., 2007. The composition of Titans stratosphere from Cassini/CIRS mid-infrared spectra. *Icarus* 189, 35–62.

Crary, F.J., Magee, B.A., Mandt, K., Waite Jr., J.H., Westlake, J., Young, D.T., 2009. Heavy ions, temperatures and winds in Titans ionosphere: Combined Cassini CAPS and INMS observations. *Planet. Space Sci.* 57, 1847–1856.

Cravens, T.E., Robertson, I.P., Waite Jr., J.H., Yelle, R.V., Kasprzak, W.T., Keller, C.N., Ledvina, S.A., Niemann, H.B., Luhmann, J.G., McNutt, R.L., Ip, W.-H., De La Haye, V., Müller-Wodarg, I., Wahlund, J.-E., Anicich, V.G., Vuitton, V., 2006. Composition of Titans ionosphere. *Geophys. Res. Lett* 33, L07105.

Crowe, S.A., Dssing, L.N., Beukes, N.J., Bau, M., Kruger, S.J., Frei, R., Canfield, D.E., 2013. Atmospheric oxygenation three billion years ago. *Nature* 501, 535–539.

Cubison, M.J., Jimenez, J.L., 2015. Statistical precision of the intensities retrieved from constrained fitting of overlapping peaks in high-resolution mass spectra. *Atmos. Meas. Tech.* 8, 2333–2345.

Cui, J., Yelle, R.V., Vuitton, V., Waite Jr., J.H., Kasprzak, W.T., Gell, D.A., Niemann, H.B., Müller-Wodarg, I.C.F., Borggren, N., Fletcher, G.G., Patrick, E.L., Raaen, E., Magee, B., 2009. Analysis of Titans neutral upper atmosphere from Cassini Ion Neutral Mass Spectrometer measurements. *Icarus* 200, 581–615.

De Haan, D.O., Hawkins, L.N., Welsh, H.G., Pednekar, J.R., Pennington E.A., , R., Casar de Loera, A., Jimenez, N.G., Symons, M.A., Zauscher, M., Pajunoja, A., Caponi, L., Cazaunau, M., Formenti, P., Gratien, A., Pangui, E., Doussin, J.-F., 2017. Brown carbon production in ammonium- or amine-containing aerosol particles by reactive uptake of methylglyoxal and photolytic cloud cycling. *Environ. Sci. Technol.* 51, 7458–7466.

DeCarlo, P.F., Slowik, J.G., Worsnop, D.R., Davidovits, P., Jimenez, J.L., 2004. Particle morphology and density characterization by combined mobility and aerodynamic diameter measurements. part 1: Theory. *Aerosol Sci. Technol.* 38, 1185–1205.

DeWitt, H.L., Trainer, M.G., Pavlov, A.A., Hasenkopf, C.A., Aiken, A.C., Jimenez, J.L., McKay, C.P., Toon, O.B., Tolbert, M.A., 2009. Reduction in haze formation rate on prebiotic Earth in the presence of hydrogen. *Astrobiology* 9, 447–453.

Dinar, E., Riziq, A.A., Spindler, C., Erlick, C., Kiss, G., Rudich, Y., 2008. The complex refractive index of atmospheric and model humic-like substances (HULIS) retrieved by a cavity ring down aerosol spectrometer (CRD-AS). *Farad. Discuss.* 137, 279–295.

Dodd, M.S., Papineau, D., Grenne, T., Slack, J.F., Rittner, M., Pirajno, F., O'Neil, J., Little, C.T.S., 2017. Evidence for early life in Earths oldest hydrothermal vent precipitates. *Nature* 543, 60–64.

Domagal-Goldman, S.D., Kasting, J.F., Johnston, D.T., Farquhar, J., 2008. Organic haze, glaciations and multiple sulfur isotopes in the Mid-Archean Era. *Earth Planet. Sci. Lett.* 269, 29–40.

Dromey, R.G., 1976. Simple index for classifying mass spectra with applications to fast library searching. *Anal. Chem.* 48, 1464–1469.

Elachi, C., Wall, S., Janssen, M., and 31 coauthors, 2006. Titan Radar Mapper observations from Cassinis T_3 fly-by. *Nature* 441, 709–713.

Ferris, J.P., Sanchez, R.A., Orgel, L.E., 1968. Studies in prebiotic synthesis iii. synthesis of pyrimidines from cyanoacetylene and cyanate. *J. Mol. Biol.* 33, 693–704.

Flagan, R.C., 2001. *Electrical Techniques, in Aerosol Measurement: Principles, Techniques, and Applications.* John Wiley: New York.

Freedman, M.A., Hasenkopf, C.A., Beaver, M.R., Tolbert, M.A., 2009. Optical properties of internally mixed aerosol particles composed of dicarboxylic acids and ammonium sulfate. *J. Phys. Chem. A* 113, 13584–13592.

Fuchs, H., Dubé, W.P., Lerner, B.M., Wagner, N.L., Williams, E.J., Brown, S.S., 2009. A sensitive and versatile detector for atmospheric NO_2 and NO_x based on blue diode laser cavity ring-down spectroscopy. *Environ. Sci. Technol.* 43, 7831–7836.

Gavilan, L., Broch, L., Carrasco, N., Fleury, B., Vettier, L., 2017. Organic aerosols in the presence of CO_2 in the early Earth and exoplanets: UV-Vis refractive indices of oxidized tholins. *Astrophys. J. Lett.* 848, L5.

Gladstone, G.R., Stern, S.A., Ennico, K., and 30 coauthors, 2016. The atmosphere of Pluto as observed by New Horizons. *Science* 351, 1280.

Goldblatt, C., Lenton, T.M., Watson, A.J., 2006. Bistability of atmospheric oxygen and the Great Oxidation. *Nature* 443, 683–686.

Griffith, C.A., Hall, J.L., Geballe, T.R., 2000. Detection of daily clouds on Titan. *Science* 20, 509–513.

Griffith, C.A., Owen, T., Geballe, T.R., Rayner, J., Rannou, P., 2003. Evidence for the exposure of water ice on Titan's surface. *Science* 300, 628–630.

Griffith, C.A., Doose, L., Tomasko, M.G., Penteado, P.F., See, C., 2012. Radiative transfer analyses of Titans tropical atmosphere. *Icarus* 218, 975–988.

Grundy, W.M., Buie, M.W., 2001. Distribution and evolution of CH_4, N_2, and CO ices on Pluto's surface: 1995 to 1998. *Icarus* 153, 248–263.

Grupen, C., 2005. *Astroparticle Physics.* Springer.

Gupta, P.K., Singh, K., Dixit, C.K., Singh, N., Sharma, C., Sahai, S., Jha, D.P., , A.K., amd Singh Tiwari, M.K., Garg, S.C., 2007. Spatial distribution in aerosol mass and size characteristics between Delhi and Hyderabad during land campaign in February 2004. *Indian J. Radio Space* 36, 576–581.

Gurwell, M.A., 2004. Submillimeter observations of Titan: Global measures of stratospheric temperature, CO, HCN, HC_3N, and the isotopic ratios $^{12}C/^{13}C$ and $^{14}N/^{15}N$. *Astrophys. J.* 616, L7–L10.

Haqq-Misra, J.D., Domagal-Goldman, S.D., Kasting, P.J., Kasting, J.F., 2008. A revised, hazy methane greenhouse for the archean Earth. *Astrobiology* 8, 1127–1137.

Hasenkopf, C.A., Beaver, M.R., Trainer, M.G., Dewitt, H.L., Freedman, M.A., Toon, O.B., McKay, C.P., Tolbert, M.A., 2010. Optical properties of Titan and early Earth haze laboratory analogs in the mid-visible. *Icarus* 207, 903–913.

Hörst, S.M., Tolbert, M.A., 2013. In situ measurements of the size and density of Titan aerosol analogs. *Astrophys. J. Lett.* 770, L10–L15.

Hörst, S.M., Yelle, R.V., Buch, A., Carrasco, N., Cernogora, G., Dutuit, O., Quirico, E., Sciamma-O'Brien, E., Smith, M.A., Somogyi, Á., Szopa, C., Thissen, R., Vuitton, V., 2012. Formation of amino acids and nucleotide bases in a Titan atmosphere simulation experiment. *Astrobiology* 12, 809–817.

Hörst, S.M., He, C., Ugelow, M.S., Jellinek, A.M., Pierrehumbert, R.T., Tolbert, M.A., 2018a. Exploring the atmosphere of Neoproterozoic Earth: The effect of o_2 on haze formation and composition. *Astrophys. J., in press.*

Hörst, S.M., Yoon, Y.H., Ugelow, M.S., Parker, A.H., Li, R., de Gouw, J.A., Tolbert, M.A., 2018b. Laboratory investigations of Titan haze formation: In situ measurement of gas and particle composition. *Icarus* 301, 136–151.

He, C., Horst, S.M., Riemer, S., Sebree, J.A., Pauley, N., Vuitton, V., 2017. Carbon monoxide affecting planetary atmospheric chemistry. *Astrophys. J.* 841, L31.

Heinritzi, M., Simon, M., Steiner, G., Wagner, A.C., Kürten, A., Hansel, A., Curtius, J., 2016. Characterization of the mass-dependent transmission efficiency of a CIMS. *Atmos. Meas. Tech.* 9, 1449–1460.

Hicks, R.K., Day, D.A., Jimenez, J.L., Tolbert, M.A., 2015. Elemental analysis of complex organic aerosol using isotopic labeling and unit-resolution mass spectrometry. *Anal. Chem.* 87, 2741–2747.

Hicks, R.K., Day, D.A., Jimenez, J.L., Tolbert, M.A., 2016. Follow the carbon: Isotopic labeling studies of early Earth aerosol. *Astrobiology* 87, 822–830.

Hirtzig, M., Bézard, B., Lellouch, E., Coustenis, A., de Bergh, C., Drossart, P., Campargue, A., Boudon, V., Tyuterev, V., Rannou, P., Cours, T., Kassi, S., Nikitin, A., Mondelain, D., Rodriguez, S., Le Mouélic, S., 2013. Titans surface and atmosphere from Cassini/VIMS data with updated methane opacity. *Icarus* 226, 470–486.

Holland, H., 2006. The oxygenation of the atmosphere and oceans. *Phil. Trans. R. Soc. B* 361, 903–915.

Hunter, E.P., Lias, S.G., 1998. Evaluated gas phase basicities and proton affinities of molecules: An update. *J. Phys. Chem. Ref. Data* 27, 413–656.

Imanaka, H., Khare, B.N., Elsila, J.E., Bakes, E.L.O., McKay, C.P., Cruikshank, D.P., Sugita, S., Matsui, T., Zare, R.N., 2004. Laboratory experiments of Titan tholin formed in cold plasma at various pressures: implications for nitrogen-containing polycyclic aromatic compounds in Titan haze. *Icarus* 168, 344–366.

Imanaka, H., Cruikshank, D.P., Khare, B.N., McKay, C.P., 2012. Optical constants of Titan tholins at mid-infrared wavelengths (2.5-25 μm) and the possible chemical nature of Titan's haze particles. *Icarus* 218, 247–261.

Irwin, P.G.J., Weir, A.L., Smith, S.E., Taylor, F.W., Lambert, A.L., Calcutt, S.B., Cameron-Smith, P.J., Carlson, R.W., Baines, K., Orton, G.S., Drossart, P., Encrenaz, T., Roos-Serote, M., 1998. Cloud structure and atmospheric composition of Jupiter retrieved from Galileo near-infrared mapping spectrometer real-time spectra. *J. Geophys. Res.* 103, 23001–23021.

Israël, G., Szopa, C., Rauli, F., Cabane, M., Niemann, H.B., Atreya, S.K., Bauer, S.J., Brun, J.-F., Chassefière, E., Coll, P., Condé, E., Coscia, D., Hauchecorne, A., Millian, P., Nguyen, M.-J., Owen, T., Riedler, W., Samuelson, R.E., Siguier, J.-M Stelle, M., Sternberg, R., Vidal-Madjar, C., 2005. Complex organic matter in Titans atmospheric aerosols from in situ pyrolysis and analysis. *Nature* 438, 796–799.

Izon, G., Zerkle, A.L., Zhelezinskaia, I., Farquhar, J., Newton, R.J., Poulton, S.W., Eigenbrode, J.L., Claire, M.W. 2015. Multiple oscillations in Neoarchaean atmospheric chemistry. *Earth and Planet. Sci. Lett.* 431, 264–273.

Jayne, J.T., Leard, D.C., Zhang, X, Davidovits, P., Smith, K.A., Kolb, C.E., Worsnop, D.R., 2000. Development of an aerosol mass spectrometer for size and composition analysis of submicron particles. *Aerosol Sci. Technol.* 33, 49–70.

Jennings, D.E., Nixon, C.A., Jolly, A., Bézard, B., Coustenis, A., Vinatier, S., Irwin, P.G.J., Teanby, N.A., Romani, P.N., Achterberg, R.K., 2008. Isotopic ratios in Titan's atmosphere from Cassini CIRS limb sounding: HC_3N in the north. *Astrophys. J. Lett.* 681, L109–L111.

Jennings, D.E., Romani, P.N., Bjoraker, G.L., Sada, P.V., Nixon, C.A., Lunsford, A.W., Boyle, R.J., Hesman, B.E., McCabe, G.H., 2009. $^{12}C/^{13}C$ ratio in ethane on Titan and implications for methanes replenishment. *J. Phys. Chem. A.* 113, 11101–11106.

Jimenez, J.L., Jayne, J.T., Shi, Q., Kolb, C.E., Worsnop, D.R., Yourshaw, I., Seinfeld, J.H., Flagan, R.C., Zhang, X., Smith, K.A., Morris, J.W., Davidovits, P., 2003. Ambient aerosol sampling using the Aerodyne Aerosol Mass Spectrometer. *J. Geophys. Res.* 108, 8425.

Jimenez, J.L., Canagaratna, M.R., Donahue, N.M., and 61 coauthors, 2009. Evolution of organic aerosols in the atmosphere. *Science* 326, 1525–1529.

Jolly, A., Fayt, A., Benilan, Y., Jacquemart, D., Nixon, C.A., Jennings, D.E., 2010. The ν_8 bending mode of diacetylene: From laboratory spectroscopy to the detection of ^{13}C isotopologues in Titan's atmosphere. *Astrophys. J.* 714, 852–859.

Junker, C., Sheahan, J.N., Jennings, S.G., O'Brien, P., Hinds, B.D., Martinez-Twary, E., Hansen, A.D.A., White, C., Garvey, D.M., Pinnick, R.G., 2004. Measurement and analysis of aerosol and black carbon in the southwestern United States and Panama and their dependence on air mass origin. *J. Geophys. Res.* 109.

Junninen, H., Ehn, M., Petäjä, T., Luosujarvi, L., Kotiaho, T., Kostiainen, R., Rohner, U., Gonin, M., Fuhrer, K., Kulmala, M., Worsnop, D.R., 2010. A high-resolution mass spectrometer to measure atmospheric ion composition. *Atmos. Meas. Tech.* 3, 1039–1053.

Kameta, K., Kouchi, N., Ukai, M., Hatano, Y., 2002. Photoabsorption, photoionization, and neutral-dissociation cross sections of simple hydrocarbons in the vacuum ultraviolet range. *J. Electron Spectrosc. Related Phenom.* 123, 225–238.

Kasting, J., Zahnle, K., Pinto, J., Young, A., 1989. Sulfur, ultraviolet radiation, and the early evolution of life. *Orig. Life Evol. Biosph* 19, 98–108.

Kasting, J.F., 1990. Bolide impacts and the oxidation state of carbon in the Earth's early atmosphere. *Origins Life Evol. Biosph.* 20, 199–231.

Kasting, J.F., 1993. Earth's early atmosphere. *Science* 259, 920–926.

Kasting, J.F., Ono, S., 2006. Palaeoclimates: the first two billion years. *Phil. Trans. R. Soc. B* 361, 917–929.

Kasting, J.F., Walker, J.C.G., 1981. Limits on oxygen concentrations in the prebiological atmosphere and the rate of abiotic fixation of nitrogen. *J. Geophys. Res.* 86, 1147–1158.

Kasting, J.F., Pavlov, A.A., Siefert, J.L., 2001. A coupled ecosystem-climate model for predicting the methane concentration in the archean atmosphere. *Orig. Life Evol. Biosphere* 31, 271–286.

Khare, B. N., Sagan, C., Thompson, W. R., Arakawa, E. T., Votaw, P., 1987. Solid hydrocarbon aerosols produced in simulated Uranian and Neptunian stratospheres. *J. Geophys. Res.* 92, 15067–15082.

Khare, B.N., Sagan, C., Arakawa, E.T., Suits, F., Callcott, T.A., Williams, M.W., 1984. Optical constants of organic tholins produced in a simulated Titanian atmosphere: From soft x-ray to microwave frequencies. *Icarus* 60, 127–137.

Kuga, M., Carrasco, N., Marty, B., Marrocchi, Y., Bernard, S., Rigaudier, T., Fleury, B., Tissandier, L., 2014. Nitrogen isotopic fractionation during abiotic synthesis of organic solid particles. *Earth Planet. Sci. Lett.* 393, 2–13.

Kurzweil, F., Claire, M., Thomazo, C., Peters, M., Hannington, M., Strauss, H, 2013. Atmospheric sulfur rearrangement 2.7 billion years ago: Evidence for oxygenic photosynthesis. *Earth Planet. Sci. Lett.* 366, 17–26.

Lack, D.A., Lovejoy, E.R., Baynard, T., Pettersson, A., Ravishankara, A.R., 2006. Aerosol absorption measurement using photoacoustic spectroscopy: Sensitivity, calibration, and uncertainty developments. *Aerosol Sci. Technol.* 40, 697–708.

Lack, D.A., Langridge, J.M., Bahreini, R., Cappa, C.D., Middlebrook, A.M., Schwarz, J.P., 2012a. Brown carbon and internal mixing in biomass burning particles. *PNAS* 109, 14802–14807.

Lack, D.A., Richardson, M.S., Law, D., Langridge, J.M., Cappa, C.D., McLaughlin, R.J., Murphy, D.M., 2012b. Aircraft instrument for comprehensive characterization of aerosol optical properties, part 2: Black and brown carbon absorption and absorption enhancement measured with photo acoustic spectroscopy. *Aerosol Sci. Technol.* 46, 555–568.

Lambe, A.T., Cappa, C.D., Massoli, P., Onasch, T.B., Forestieri, S.D., Martin, A.T., Cummings, M.J., Croasdale, D.R., Brune, W.H., Worsnop, D.R., Davidovits, P., 2013. Relationship between oxidation level and optical properties of secondary organic aerosol. *Environ. Sci. Technol.* 47, 6349–6357.

Lang-Yona, N., Rudich, Y., Segre, E., Dinar, E., Riziq, A.A., 2009. Complex refractive indices of aerosols retrieved by continuous wave-cavity ring down aerosol spectrometer. *Anal. Chem.* 81, 1762–1769.

Lavvas, P., Yelle, R.V., Koskinen, T., Bazinc, A., Vuitton, V., Vigren, E., Galand, M., Wellbrocke, A., Coates, A.J., Wahlund, J.E-., Crary, F.J., Snowden, D., 2013. Aerosol growth in Titans ionosphere. *PNAS* 110, 2729–2734.

Le Gall, A., Malaska, M.J., Lorenz, R.D., Janssen, M.A., Tokano, T., Hayes, A.G., Mastrogiuseppe, M., Lunine, J.I., Veyssiére, G., Encrenaz, P., Karatekin, O., 2016. Composition, seasonal change, and bathymetry of Ligeia Mare, Titan, derived from its microwave thermal emission. *J. Geophys. Res.* 121, 233–251.

Lee, S.K., Wagiran, H., A.T.,, Ramli Apriantoro, N.H., K.A.,, Wood 2009. Radiological monitoring: Terrestrial natural radionuclides in Kinta District, Perak, Malaysia. *J. Environ. Radioact.* 100, 368–374.

Levy, M.E., Zhang, R., Zheng, J., Tan, H., Wang, Y., Molina, L.T., Takahama, S., Russell, L.M., Li, G., 2014. Measurements of submicron aerosols at the California-Mexico borderduring the Cal-Mex 2010 field campaign. *Atmos. Environ.* 88, 308–319.

Lorenz, R.D., Wall, S., Radebaugh, J., and 37 coauthors 2006. The sand seas of titan: Cassini RADAR observations of longitudinal dunes. *Science* 312, 724–727.

Lu, H.-C., Chen, K.-K., Chen, H.-F., Cheng, B.-M., Ogilvie, J.F., 2010. Absorption cross section of molecular oxygen in the transition E $^3\Sigma_\mathrm{u}^-$ $\nu = 0$ - X $^3\Sigma_\mathrm{g}^-$ $\nu = 0$ at 38 K. *Astron. Astrophys.* 520, A19.

Lunine, J.I., Atreya, S.K., 2008. The methane cycle on Titan. *Nat. Geosci.* 1, 159–164.

Magee, B.A., Waite, J.H., Mandt, K.E., Westlake, J., Bell, J., Gell, D.A., 2009. INMS-derived composition of Titans upper atmosphere: Analysis methods and model comparison. *Planet. Space Sci.* 57, 1895–1916.

Maharana, M., Krishnan, N., Sengupta, D., 2010. Spatial distribution of gamma radiation levels in surface soils from Jaduguda uranium mineralization zone, Jharkhand, India, using γ-ray spectrometry, and determination of outdoor dose to the population. *J. Med. Phys.* 35, 235–241.

Mahjoub, A., Carrasco, N., Dahoo, P.R., Gautier, T., Szopa, C., Cernogora, G., 2012. Influence of methane concentration on the optical indices of Titan's aerosols analogues. *Icarus* 221, 670–677.

Mahjoub, A., Carrasco, N., Dahoo, P.R., Fleury, B., Gautier, T., Cernogora, G., 2014. Effect of the synthesis temperature on the optical indices of organic materials produced by $N_2 - CH_4$ RF plasma. *Plasma Processes Polym.* 11, 409417.

Mandt, K.E., Waite, J.H., Teolis, B., Magee, B.A., Bell, J., Westlake, J.H., Nixon, C.A., Mousis, O., Lunine, J.I., 2012. The $^{12}C/^{13}C$ ratio on Titan from Cassini INMS measurements and implications for the evolution of methane. *Astrophys. J.* 749, 160.

Marten, A., Hidayat, T., Biraud, Y., Moreno, R., 2002. New millimeter heterodyne observations of Titan: Vertical distributions of nitriles HCN, HC_3N, CH_3CN, and the isotopic ratio $^{15}N/^{14}N$ in its atmosphere. *Icarus* 158, 532–544.

McKay, C.P., Pollack, J.B., Courtin, R., 1989. The thermal structure of Titan's atmosphere. *Icarus* 80, 23–53.

McKay, C.P., Pollack, J.B., Courtin, R., 1991. The greenhouse and antigreenhouse effects on Titan. *Science* 253, 1118–1121.

McLafferty, F.W. Tureček, F., 1993. *Interpretation of Mass Spectra.* University of Science Books, Sausalito, CA.

Moreno, V., Baixeras, C., Font, L.I., J.,, Bach 2008. Indoor radon levels and their dynamics in relation with the geological characteristics of La Garrotxa, Spain. *Radiat. Meas.* 43, 1532–1540.

Mount, G.H., Warden, E.S., Moos, H.W., 1977. Photoabsorption cross sections of methane from 1400 to 1850 $\mathring{A}$. *Astrophys. J.* 214, L47–L49.

Murty, V.R., Karunakara, N., 2008. Natural radioactivity in the soil samples of Botswana. *Radiat. Meas.* 43, 1541–1545.

Navarro-Gonzaléz, R., McKay, C.P., Mvondo, D.N., 2001. A possible nitrogen crisis for Archaean life due to reduced nitrogen fixation by lightning. *Nature* 412, 61–64.

Negrão, A., Coustenis, A., Lellouch, E., Maillard, J.P., Rannou, P., Schmitt, B., McKay, C.P., Boudon, V., 2006. Titans surface albedo variations over a Titan season from near-infrared CFHT/FTS spectra. *Planet. Space Sci.* 54, 1225–1246.

Nguyen, M.-J., Raulin, F., Coll, P., Derenne, S., Szopa, C., Cernogora, G., Israël, G., Bernard, J.-M., 2007. Carbon isotopic enrichment in Titan's tholins? implications for Titan's aerosols. *Planet. Space Sci.* 55, 2010–2014.

Nguyen, M.-J., Raulin, F., Coll, P., Derenne, S., Szopa, C., Cernogora, G., Israël, G., Bernard, Jean-Miche 2008. From Titans tholins to Titans aerosols: Isotopic study and chemical evolution at Titans surface. *Adv. Space Res.* 42, 48–53.

Niemann, H.B., Atreya, S.K., Demick, J.E., Gautier, D., Haberman, J.A., Harpold, D.N., Kasprzak, W.T., Lunine, J.I., Owen, T.C., Raulin, F., 2010. Composition of Titan's lower atmosphere and simple surface volatiles as measured by the Cassini-Huygens probe gas chromatograph mass spectrometer experiment. *J. Geophys. Res.* 115, E12006.

Nixon, C.A., Achterberg, R.K., Vinatier, S., Bézard, B., Coustenis, A., Irwin, P.G.J., Teanby, N.A., de Kok, R., Romani, P.N., Jennings, D.E., Bjoraker, G.L., Flasar, F.M., 2008. The ^{12}C/^{13}C isotopic ratio in Titan hydrocarbons from Cassini/CIRS infrared spectra. *Icarus* 195, 778–791.

Nixon, C.A., Temelso, B., Vinatier, S., Teanby, N.A., Bézard, B., Achterberg, R.K., Mandt, K.E., Sherrill, C.D., Irwin, P.G.J., Jennings, D.E., 2012. Isotopic ratios in Titan's methane: Measurements and modeling. *Astrophys. J.* 749, 159.

Onasch, T.B., Massoli, P., Kebabian, P.L., Hills, F.B., Bacon, F.W., Freedman, A., 2015. Single scattering albedo monitor for airborne particulates. *Aerosol Sci. Technol.* 49, 267–279.

Pang, Y., Turpin, B.J., Gundel, L. A., 2006. On the importance of organic oxygen for understanding organic aerosol particles, aerosol science and technology,. *Aerosol Sci. Technol.* 40, 128–133.

Pavlov, A.A., Kasting, J.F., 2002. Mass-independent fractionation of sulfur isotopes in Archean sediments: strong evidence for an anoxic Archean atmosphere. *Astrobiology* 2, 27–41.

Pavlov, A.A., Brown, L.L., Kasting, J.F., 2001. UV shielding of NH_3 and O_2 by organic hazes in the Archean atmosphere. *J. Geophys. Res.* 106, 23267–23287.

Pyror, W.R., Hord, C.W., 1991. A study of photopolarimeter system UV absorption data on Jupiter, Saturn, Uranus, and Neptune: Implications for auroral haze formation. *Icarus* 91, 161–172.

Radebaugh, J., Lorenz, R.D., Kirk, R.L., Lunine, J.I., Stofan, E.R., Lopes, R.M.C., Wall, S.D., the Cassini Radar Team, 2007. Mountains on Titan observed by Cassini Radar. *Icarus* 192, 77–91.

Radney, J.G., Ma, X., Gillis, K.A., Zachariah, M.R., Hodges, J.T., Zangmeister, C.D., 2013. Direct measurements of mass-specific optical cross sections of single-component aerosol mixtures. *Anal. Chem.* 85, 8319–8325.

Radney, J.G., You, R., Ma, X., Conny, J.M., Zachariah, M.R., Hodges, J.T., Zangmeister, C.D., 2014. Dependence of soot optical properties on particle morphology: Measurements and model comparisons. *Environ. Sci. Techol.* 48, 3169–3176.

Ramirez, S.I., Coll, P, da Silva, A., Navarro-González, R., Lafait, J., Raulin, F., 2002. Complex refractive index of Titan's aerosol analogues in the 200-900 nm domain. *Icarus* 156, 515–529.

Ranjan, S., Sasselov, D.D., 2016. Influence of the uv environment on the synthesis of prebiotic molecules. *Astrobiology* 16, 68–88.

Rannou, P., Cours, T., Le Mouélic, S., Rodriguez, S., Sotin, C., Drossart, P., Brown, R., 2010. Titan haze distribution and optical properties retrieved from recent observations. *Icarus* 208, 850–867.

Riziq, A.A., Erlick, C., Dinar, E., Rudich, Y., 2007. Optical properties of absorbing and non-absorbing aerosols retrieved by cavity ring down CRD spectroscopy. *Atmos. Chem. Phys.* 7, 1523–1536.

Roe, H.G., de Pater, I., Macintosh, B.A., McKay, C.P., 2002. Titan's clouds from Gemini and Keck adaptive optics imaging. *Astrophys. J.* 581, 1399–1406.

Sagan, C., Chyba, C., 1997. The Early faint sun paradox: Organic shielding of ultraviolet-labile greenhouse gases. *Science* 276, 1217–1221.

Sagan, C., Mullen, G., 1972. Earth and Mars: Evolution of atmospheres and surface temperatures. *Science* 177, 52–56.

Schopf, J.W., 1993. Microfossils of the early Archean apex chert: New evidence of the antiquity of life. *Science* 260, 640–646.

Sciamma-O'Brien, E., Dahoo, P.R., Hadamcik, E., Carrasco, N., Quirico, E., Szopa, C., Cernogora, G., 2012. Optical constants from 370 nm to 900 nm of Titan tholins produced in a low pressure RF plasma discharge. *Icarus* 218, 356–363.

Sebree, J.A., Stern, J.C., Mandt, K.E., Domagal-Goldman, S.D., Trainer, M.G., 2016. ^{13}C and ^{15}N fractionation of CH_4/N_2 mixtures during photochemical aerosol formation: Relevance to Titan. *Icarus* 270, 421–428.

Segura, A., Meadows, V.S., Kasting, J.F., Crisp, D., Cohen, M., 2007. Abiotic formation of O_2 and O_3 in high-CO_2 terrestrial atmospheres. *Astron. Astrophys.* 472, 665–679.

Shuman, N.S., Hunton, D.E., Viggiano, A.A., 2015. Ambient and modified atmospheric ion chemistry: From top to bottom. *Chem. Rev.* 115, 4542–4570.

Stark, G., Yoshino, K., Smith, P.L., Ito, K., 2007. Photoabsorption cross section measurements of CO_2 between 106.1 and 118.7 nm at 295 and 195 K. *J. Quant. Spectrosc. Radiat. Transfer* 103, 67–73.

Tomasko, M.G., Archinal, B., Becker, T., and 37 coauthors, 2005. Rain, winds and haze during the Huygens probes descent to Titans surface. *Nature* 438, 765–778.

Tomasko, M.G., Doose, L., Engel, S., Dafoe, L.E., West, R., Lemmon, M., Karkoschka, E., See, C., 2008. A model of Titans aerosols based on measurements made inside the atmosphere. *Planet. Space Sci.* 56, 669–707.

Toon, O.B., Pollack, J.B., Khare, B.N., 1976. The optical constants of several atmospheric aerosol species: Ammonium sulfate, aluminum oxide, and sodium chloride. *J. Geophys. Res.* 81, 5733–5748.

Trainer, M.G., Pavlov, A.A., Jimenez, J.L., McKay, C.P., Worsnop, D.R., Toon, O.B., Tolbert, M.A., 2004. Chemical composition of Titan's haze: Are PAHs present? *Geophys. Res. Lett.* 31, L17S08.

Trainer, M.G., Pavlov, A.A., DeWitt, H.L., Jimenez, J.L., McKay, C.P., Toon, O.B., Tolbert, M.A., 2006. Organic haze on Titan and the early Earth. *PNAS* 103, 18035–18042.

Trainer, M.G., Jimenez, J.L., Yung, Y.L., Toon, O.B., Tolbert, M.A., 2012. Nitrogen incorporation in CH_4-N_2 photochemical aerosol produced by far ultraviolet irradiation. *Astrobiology* 12, 315–326.

Trainer, M.G., Sebree, J.A., Yoon, Y.H., Tolbert, M.A., 2013. The influence of benzene as a trace reactant in titan aerosol analogs. *Astrophys. J. Lett.* 766, L4.

Tran, B.N., Joseph, J.C., Ferris, J.P., Persans, P.D., Chera, J.J., 2003. Simulation of Titan haze formation using a photochemical flow reactor The optical constants of the polymer. *Icarus* 165, 379–390.

Tran, B.N., Joseph, J.C., Force, M., Briggs, R.G., Vuitton, V., Ferris, J.P., 2005. Photochemical processes on Titan: Irradiation of mixtures of gases that simulate Titans atmosphere. *Icarus* 177, 106–115.

Turtle, E.P., Perry, J.E., McEwen, A.S., Del Genio, A.D., Barbara, J., West, R.A., Dawson, D.D., Porco, C.C., 2009. Cassini imaging of Titan's high-latitude lakes, clouds, and south-polar surface changes. *Geophys. Res. Lett.* 36, L02204.

Turtle, E.P., Del Genio, A.D., Barbara, J.M., Perry, J.E., Schaller, E.L., McEwen, A.S., West, R.A., Ray, T.L., 2011a. Seasonal changes in Titan's meteorology. *Geophys. Res. Lett.* 38, L03203.

Turtle, E.P., Perry, J.E., Hayes, A.G., Lorenz, R.D., Barnes, J.W., McEwen, A.S., West, R.A., Del Genio, A.D., Barbara, J.M., Lunine, J.I., Schaller, E.L., Ray, T.L., Lopes, R.M.C., Stofan, E.R., 2011b. Rapid and extensive surface changes near Titans equator: Evidence of april showers. *Science* 18, 1414–1417.

Ugelow, M.S., Zarzana, K.J., Day, D.A., Jimenez, J.L., Tolbert, M.A., 2017. The optical and chemical properties of discharge generated organic haze using in-situ real-time techniques. *Icarus* 294, 1–13.

Ugelow, M.S., De Haan, D.O., Hörst, S.M., Tolbert, M.A., 2018. The effect of oxygen on haze analog properties. *Astrophys. J. Lett., in press.*

Vinatier, S., Bézard, B., Fouchet, T., Teanby, N.A., de Kok, R., Irwin, P.G.J., Conrath, B.J., Nixon, C.A., Romani, P.N., Flasar, F.M., Coustenis, A. 2007a. Vertical abundance profiles of hydrocarbons in Titans atmosphere at 15°S and 80°N retrieved from Cassini/CIRS spectra. *Icarus* 188, 120–138.

Vinatier, S., Bézard, B., Nixon, C.A., 2007b. The Titan $^{15}N/^{14}N$ and $^{12}C/^{13}C$ isotopic ratios in HCN from Cassini/CIRS. *Icarus* 191, 712–721.

Vinatier, S., Rannou, P., Anderson, C.M., Bézard, B., de Kok, R., Samuelson, R.E., 2012. Optical constants of Titans stratospheric aerosols in the 701500 cm^1 spectral range constrained by Cassini/CIRS observations. *Icarus* 219, 5–12.

Wagener, R., Caldwell, J., Fricke, K.H., 1986. The geometric albedos of Uranus and Neptune between 2100 and 3350 A. *Icarus* 67, 281–288.

Wahlund, J.-E., Galand, M., Müller-Wodarg, I., Cui, J., Yelle, R.V., Crary, F.J., Mandt, K., Magee, B., Waite Jr., J.H., Young, D.T., Coates, A.J., Garnier, P., Ågren, K., André, M., Eriksson, A.I., Cravens, T.E., Vuitton, V., Gurnett, D.A., Kurth, W.S., 2009. On the amount of heavy molecular ions in Titan's ionosphere. *Planet. Space Sci.* 57, 1857–1865.

Waite Jr., J.H., Niemann, H., Yelle, R.V., Kasprzak, W.T., Cravens, T.E., Luhmann, J.G., McNutt, R.L., Ip, W-H., Gell, D., De La Haye, V., Müller-Wordag, I., Magee, B., Borggren, N., Ledvina, S., Fletcher, G., Walter, E., Miller, R., Scherer, S., Thorpe, R., Xu, J., Block, B., Arnett, K., 2005. Ion neutral mass spectrometer results from the first flyby of Titan. *Science* 308, 982–986.

Waite Jr., J.H., Young, D.T., Cravens, T.E., Coates, A.J., Crary, F.J., Magee, B., Westlake, J., 2007. The process of tholin formation in titans upper atmosphere. *Science* 316, 870–875.

Wang, Q., Zhao, J., Du, W., Ana, G., Wang, Z., Sun, L., Wang, Y., Zhang, F., Li, Z., Ye, X., Sun, Y., 2016. Characterization of submicron aerosols at a suburban site in central China. *Atmos. Environ.* 131, 115–123.

Washenfelder, R.A., Flores, J.M., Brock, C.A., Brown, S.S., Rudich, Y., 2013. Broadband measurements of aerosol extinction in the ultraviolet spectral region. *Atmos. Meas. Tech.* 6, 861–877.

Wiedensohler, A. 1988. An approximation of the bipolar charge distribution for particles in the submicron size range. *J. Aerosol Sci.* 19, 387–389.

Wilde, S.A., Valley, J.W., Peck, W.H., Graham, C.M., 2001. Evidence from detrital zircons for the existence of continental crust and oceans on the earth 4.4 Gyr ago. *Nature* 409, 175–178.

Wolf, E.T., Toon, O.B., 2010. Fractal organic hazes provided an ultraviolet shield for early Earth. *Science* 328, 1266–1268.

Yamagata, Y., 1999. Prebiotic formation of ADP and ATP from AMP, calcium phosphates and cyanate in aqueous solution. *Orig. Life. Evol. Biosph.* 29, 511–520.

Yoon, Y.H., Hörst, S.M., Hicks, R.K., Li, R., de Gouw, J.A., Tolbert, M.A., 2014. The role of benzene photolysis in Titan haze formation. *Icarus* 233, 233–241.

Yoshino, K., Esmond, J.R., Sun, Y., Parkinson, W.H., Ito, K., Matsui, T., 1996. Absorption cross section measurements of carbon dioxide in the wavelength region 118.7 - 175.5 nm and the temperature dependence. *J. Quant. Spectrosc. Radiat. Transfer* 55, 53–60.

Yung, Y.L., McElroy, M.B., 1979. Fixation of nitrogen in the prebiotic atmosphere. *Science* 203, 1002–1004.

Zahnle, K., Claire, M., Catling, D., 2006. The loss of mass-independent fractionation in sulfur due to a Palaeoproterozoic collapse of atmospheric methane. *Geobiology* 4, 271–283.

Zahnle, K.J., 1986. Photochemistry of methane and the formation of hydrocyanic acid (HCN) in the Earth's early atmosphere. *J. Geophys. Res.* 91, 2819–2834.

Zarzana, K.J., 2014. *Optical Properties of Absorbing Atmospheric Aerosol.* PhD thesis, University of Colorado.

Zarzana, K.J, De Haan, D.O., Freedman, M.A., Hasenkopf, C.A., Tolbert, M.A., 2012. Optical properties of the products of α-dicarbonyl and amine reactions in simulated cloud droplets. *Environ. Sci. Technol* 46, 4845–4851.

Zarzana, K.J., Cappa, C.D., Tolbert, M.A., 2014. Sensitivity of aerosol refractive index retrievals using optical spectroscopy. *Aerosol Sci. Technol.* 48, 1133–1144.

Zerkle, A.L., Claire, M.W., Domagal-Goldman, S.D., Farquhar, J., Poulton, S.W., 2012. A bistable organic-rich atmosphere on the Neoarchaean Earth. *Nat. Geosci.* 5, 359–363.

Zhang, X., Kim, H., Parworth, C.L., Young, D.E., Zhang, Q., Metcalf, A.R., Cappa, C.D., 2016. Optical properties of wintertime aerosols from residential wood burning in Fresno, CA: Results from DISCOVER-AQ 2013. *Environ. Sci. Technol.* 50, 1681–1690.

Appendix A Identified Ions

The following ions are the ions identified for each analog in the study described in Chapter 5. The tables are grouped by analog, with the negative ions listed in Table A and the positive ions listed in Table B.

Chemical Formula	Exact Mass (Da)
CN^-	26.003623
$C_2H_2N^-$	40.019273
C_2HO^-	41.003288
CHN_2^-	41.014522
CNO^-	41.998537
CHO_2^-	44.998203
NO_2^-	45.993452
C_3N^-	50.003623
NO_3^-	61.988366
C_3NO^-	65.998537
$C_3H_2NO^-$	68.014187
$C_3H_3O_2^-$	71.013853
$CH_2N_3O^-$	72.020335
$C_4H_4NO^-$	82.029837
$C_3H_2NO_2^-$	84.009102
$C_2HN_2O_2^-$	85.004351
$C_4H_5O_2^-$	85.029503
$C_2H_2NO_3^-$	88.004016
$CHN_2O_3^-$	88.999265
$C_3H_5O_3^-$	89.024418
$C_2H_3O_4^-$	91.003682
$CH_2NO_4^-$	91.998931
$C_4H_2N_3^-$	92.025421
$C_5H_6NO^-$	96.045487
$C_3H_4NO_3^-$	102.019667
$C_4H_3N_2O_2^-$	111.020001
$C_4H_5N_2O_2^-$	113.035651
$C_4H_3O_4^-$	115.003682
$C_7H_3N_2^-$	115.030172
$C_7H_2N_3^-$	128.025421
$C_5HN_2O_3^-$	136.999265
$CH_2N_2O_6^-$	137.991834

Table 1A: Negative ions identified during haze formation with 0.1% CO_2, 0.1% CH_4 and N_2.

Chemical Formula	Exact Mass (Da)
H_4N^+	18.033826
H_3O^+	19.017841
$C_2H_3^+$	27.022927
N_2^+	28.005599
CH_2N^+	28.018175
CHO^+	29.002191
HN_2^+	29.013424
CH_4N^+	30.033826
C_3H^+	37.007276
$C_3H_3^+$	39.022927
CHN_2^+	41.013424
$C_3H_5^+$	41.038577
N_3^+	42.008673
$C_2H_4N^+$	42.033826
$CH_3N_2^+$	43.029075
CO_2^+	43.989281
$C_2H_6N^+$	44.049476
CHO_2^+	44.997106
$C_2HN_2^+$	53.013424
CN_3^+	54.008673
$C_2H_3N_2^+$	55.029075
N_4^+	56.011747
HN_4^+	57.019572
$C_3H_8N^+$	58.065126
$C_3H_{10}N^+$	60.080776
$C_3H_2NO^+$	68.013090
$C_4H_8N^+$	70.065126
$C_4H_{10}N^+$	72.080776
$C_3H_8NO^+$	74.060040
$C_4H_{12}N^+$	74.096426
$C_5H_{10}N^+$	84.080776
$C_4H_8NO^+$	86.060040
$C_5H_{12}N^+$	86.096426
$C_4H_{10}NO^+$	88.075690
$C_5H_{14}N^+$	88.112076
$C_3N_4^+$	92.011747
$C_6H_8N^+$	94.065126
$C_6H_{12}N^+$	98.096426
$C_5H_{10}NO^+$	100.075690
$C_6H_{14}N^+$	100.112076
$C_5H_{12}NO^+$	102.091340
$C_6H_{16}N^+$	102.127726
$C_7H_{10}N^+$	108.080776
$C_7H_{14}N^+$	112.112076

Chemical Formula	Exact Mass (Da)
$C_6H_{12}NO^+$	114.091340
$C_7H_{16}N^+$	114.127726
$C_6H_{14}NO^+$	116.106990
$C_8H_{12}N^+$	122.096426
$C_8H_{16}N^+$	126.127726
$C_7H_{14}NO^+$	128.106990
$C_8H_{18}N^+$	128.143376
$C_6H_{12}NO_2^+$	130.086255
$C_7H_{16}NO^+$	130.122641
$C_8H_{20}N^+$	130.159026
$C_9H_{14}N^+$	136.112076
$C_9H_{18}N^+$	140.143376
$C_8H_{16}NO^+$	142.122641
$C_7H_{15}N_2O^+$	143.117889
$C_7H_{17}N_2O^+$	145.133540
$C_8H_{17}N_2O^+$	157.133540
$C_8H_{19}N_2O^+$	159.149190
$C_9H_{17}N_2O^+$	169.133540
$C_9H_{19}N_2O^+$	171.149190
$C_8H_{17}N_2O_2+$	173.128454
$C_9H_{21}N_2O^+$	173.164840
$C_{10}H_{19}N_2O^+$	183.149190
$C_{10}H_{21}N_2O^+$	185.164840
$C_9H_{19}N_2O_2^+$	187.144104
$C_{10}H_{23}N_2O^+$	187.180490
$C_{11}H_{21}N_2O6+$	197.164840
$C_{11}H_{23}N_2O^+$	199.180490
$C_{11}H_{22}NO_2^+$	200.164505
$C_{10}H_{21}N_2O_2^+$	201.159754
$C_{11}H_{25}N_2O^+$	201.196140
$C_{12}H_{19}N_2O^+$	207.149190

Table 1B: Positive ions identified during haze formation with 0.1% CO_2, 0.1% CH_4 and N_2.

Chemical Formula	Exact Mass (Da)
CN^-	26.003623
$C_2H_2N^-$	40.019273
C_2HO^-	41.003288
CNO^-	41.998537
CHO_2^-	44.998203
NO_2^-	45.993452
C_3N^-	50.003623
NO_3^-	61.988366
$C_3HN_2^-$	65.014522
C_3NO^-	65.998537
$C_4H_3O^-$	67.018938
$C_3H_2NO^-$	68.014187
$C_3HO_2^-$	68.998203
$C_3H_3O_2$-	71.013853
$C_2H_3O_3^-$	75.008768
$C_4H_4NO^-$	82.029837
$C_3H_3N_2O^-$	83.025086
$C_3H_2NO_2^-$	84.009102
$C_2HN_2O_2^-$	85.004351
$C_2H_2NO_3^-$	88.004016
$CHN_2O_3^-$	88.999265
$C_3H_5O_3^-$	89.024418
$C_2H_3O_4^-$	91.003682
$C_4HN_2O^-$	93.009436
$C_5H_6NO^-$	96.045487
$C_4H_5O_3^-$	101.024418
$C_3H_4NO_3^-$	102.019667
$C_6H_8NO^-$	110.061137
$C_4H_3N_2O_2^-$	111.020001
$C_4H_5N_2O_2^-$	113.035651
$C_4H_4NO_3^-$	114.019667
$C_4H_6NO_3^-$	116.035317
$C_8H_6N^-$	116.050573
$C_5H_5N_2O_2^-$	125.035651
$C_5H_4NO_3^-$	126.019667
$C_4H_3N_2O_3^-$	127.014916
$C_5H_6NO_3^-$	128.035317
$C_6H_7N_2O_2^-$	139.051301
$C_6H_7N_2O_3^-$	155.046216

Table 2A: Negative ions identified during haze formation with 2 ppmv O_2, 0.1% CO_2, 0.1% CH_4 and N_2.

Chemical Formula	Exact Mass (Da)
N^+	14.002525
CH_5^+	17.038577
H_3O^+	19.017841
$C_2H_3^+$	27.022927
N_2^+	28.005599
CH_2N^+	28.018175
CHO^+	29.002191
HN_2^+	29.013424
CH_4N^+	30.033826
CH_3O^+	31.017841
C_3H^+	37.007276
$C_3H_3^+$	39.022927
CHN_2^+	41.013424
$C_3H_5^+$	41.038577
N_3^+	42.008673
$C_2H_4N^+$	42.033826
$CH_3N_2^+$	43.029075
CO_2^+	43.989281
$C_2H_6N^+$	44.049476
CHO_2^+	44.997106
$C_2HN_2^+$	53.013424
CN_3^+	54.008673
N_4^+	56.011747
HN_4^+	57.019572
$C_3H_8N^+$	58.065126
CN_4^+	68.011747
$C_4H_8N^+$	70.065126
$C_4H_{10}N^+$	72.080776
$CHN_2O_2^+$	73.003254
$C_3H_8NO^+$	74.06004
$C_4H_{12}N^+$	74.096426
$C_5H_{10}N^+$	84.080776
$C_5H_{12}N^+$	86.096426
$C_4H_{10}NO^+$	88.07569
$C_5H_{14}N^+$	88.112076
$C_6H_8N^+$	94.065126
$C_6H_{12}N^+$	98.096426
$C_5H_{10}NO^+$	100.07569
$C_6H_{14}N^+$	100.112076
$C_5H_{12}NO^+$	102.09134
$C_6H_{16}N^+$	102.127726
$C_7H_{10}N^+$	108.080776
$C_7H_{14}N^+$	112.112076
$C_6H_{12}NO^+$	114.09134

Chemical Formula	Exact Mass (Da)
$C_7H_{16}N^+$	114.127726
$C_6H_{14}NO^+$	116.10699
$C_8H_{12}N^+$	122.096426
$C_8H_{16}N^+$	126.127726
$C_7H_{14}NO^+$	128.10699
$C_8H_{18}N^+$	128.143376
$C_7H_{16}NO^+$	130.122641
$C_9H_{14}N^+$	136.112076
$C_8H_{14}NO^+$	140.10699
$C_9H_{18}N^+$	40.143376
$C_8H_{16}NO^+$	142.122641
$C_9H_{20}N^+$	142.159026
$C_7H_{14}NO_2^+$	144.101905
$C_8H_{18}NO^+$	144.138291
$C_7H_{17}N_2O^+$	145.13354
$C_9H_{18}NO^+$	156.138291
$C_8H_{17}N_2O^+$	157.13354
$C_8H_{19}N_2O^+$	159.14919
$C_{10}H_{20}NO^+$	170.153941
$C_9H_{19}N_2O^+$	171.14919
$C_9H_{21}N_2O^+$	173.16484
$C_8H_{19}N_2O_2^+$	175.144104
$C_{10}H_{19}N_2O^+$	183.14919
$C_{10}H_{18}NO_2^+$	184.133205
$C_{10}H_{21}N_2O^+$	185.16484
$C_9H_{19}N_2O_2^+$	187.144104
$C_{10}H_{23}N_2O^+$	187.18049
$C_9H_{21}N_2O_2^+$	189.159754
$C_{11}H_{17}N_2O^+$	193.13354
$C_{11}H_{21}N_2O^+$	197.16484
$C_{10}H_{19}N_2O_2^+$	199.144104
$C_{11}H_{23}N_2O^+$	199.18049
$C_{10}H_{21}N_2O_2^+$	201.159754
$C_{10}H_{23}N_2O_2^+$	203.175404

Table 2B: Positive ions identified during haze formation with 2 ppmv O_2, 0.1% CO_2, 0.1% CH_4 and N_2.

Chemical Formula	Exact Mass (Da)
CN^-	26.003623
$C_2H_2N^-$	40.019273
C_2HO^-	41.003288
CNO^-	41.998537
NO_2^-	45.993452
C_3N^-	50.003623
NO_3^-	61.988366
C_3NO^-	65.998537
$C_3H_2NO^-$	68.014187
$C_3HO_2^-$	68.998203
$C_3H_3O_2^-$	71.013853
$C_4H_4NO^-$	82.029837
$C_3H_2NO_2^-$	84.009102
$C_2HN_2O_2^-$	85.004351
$C_2H_2NO_3^-$	88.004016
$CHN_2O_3^-$	88.999265
$C_2H_3O_4^-$	91.003682
$C_5H_6NO^-$	96.045487
$C_4H_5O_3^-$	101.024418
$C_6H_8NO^-$	110.061137
$C_4H_3N_2O_2^-$	111.020001
$C_4H_5N_2O_2^-$	113.035651
$C_4H_4NO_3^-$	114.019667
$C_4H_6NO_3^-$	116.035317
$C_8H_6N^-$	116.050573
$C_5H_5N_2O_2^-$	125.035651
$C_9H_3O^-$	127.018938
$C_5H_6NO_3^-$	128.035317
$C_8H_5N_2^-$	129.045822
$C_7H_4N_5^-$	158.047219

Table 3A: Negative ions identified during haze formation with 20 ppmv O_2, 0.1% CO_2, 0.1% CH_4 and N_2.

Chemical Formula	Exact Mass (Da)
N^+	14.002525
CH_5^+	17.038577
H_3O^+	19.017841
$C_2H_3^+$	27.022927
N_2^+	28.005599
CH_2N^+	28.018175
CHO^+	29.002191
HN_2^+	29.013424
CH_4N^+	30.033826
$C_3H_3^+$	39.022927
CHN_2^+	41.013424
$C_3H_5^+$	41.038577
N_3^+	42.008673
$C_2H_4N^+$	42.033826
HN_3^+	43.016498
$CH_3N_2^+$	43.029075
CO_2^+	43.989281
$C_2H_6N^+$	44.049476
CHO_2^+	44.997106
$C_2HN_2^+$	53.013424
CN_3^+	54.008673
$C_2H_3N_2^+$	55.029075
N_4^+	56.011747
$C_3H_6N^+$	56.049476
HN_4^+	57.019572
$C_3H_8N^+$	58.065126
C_2H6NO^+	60.04439
CN_4^+	68.011747
$C_4H_8N^+$	70.065126
$C_4H_{10}N^+$	72.080776
$CHN_2O_2^+$	73.003254
$C_3H_8NO^+$	74.06004
$C_4H_{12}N^+$	74.096426
$C_5H_{10}N^+$	84.080776
$C_4H_8NO^+$	86.06004
$C_5H_{12}N^+$	86.096426
$C_4H_{10}NO^+$	88.07569
$C_6H_8N^+$	94.065126
$C_6H_{12}N^+$	98.096426
$C_5H_{10}NO^+$	100.07569
$C_6H_{14}N^+$	100.112076
$C_5H_{12}NO^+$	102.09134
$C_7H_{10}N^+$	108.080776
$C_7H_{14}N^+$	112.112076

Chemical Formula	Exact Mass (Da)
$C_6H_{12}NO^+$	114.09134
$C_7H_{16}N^+$	114.127726
$C_6H_{14}NO^+$	116.10699
$C_5H_{13}N_2O^+$	117.102239
$C_8H_{12}N^+$	122.096426
$C_7H_{14}NO^+$	128.10699
$C_7H_{16}NO^+$	130.122641
$C_6H_{15}N_2O^+$	131.117889
$C_7H_{17}N_2O^+$	145.13354
$C_8H_{17}N_2O^+$	157.13354
$C_8H_{19}N_2O^+$	159.14919
$C_7H_{17}N_2O_2^+$	161.128454
$C_9H_{19}N_2O^+$	171.14919
$C_8H_{17}N_2O_2^+$	173.128454
$C_9H_{21}N_2O^+$	173.16484
$C_8H_{19}N_2O_2^+$	175.144104
$C_{10}H_{19}N_2O^+$	183.14919
$C_9H_{17}N_2O_2^+$	185.128454
$C_{10}H_{21}N_2O^+$	185.16484
$C_9H_{19}N_2O_2^+$	187.144104
$C_{11}H_{21}N_2O^+$	197.16484
$C_{10}H_{19}N_2O_2^+$	199.144104
$C_{10}H_{21}N_2O_2^+$	201.159754
$C_{11}H_{25}N_2O^+$	201.19614
$C_{11}H_{23}N_2O_2^+$	215.175404
$C_{13}H_{21}N_2O^+$	221.16484

Table 3B: Positive ions identified during haze formation with 20 ppmv O_2, 0.1% CO_2, 0.1% CH_4 and N_2.

Chemical Formula	Exact Mass (Da)
C_2HO^-	41.003288
CNO^-	41.998537
CHO_2^-	44.998203
NO_2^-	45.993452
NO_3^-	61.988366
$C_3H_2NO^-$	68.014187
$C_3H_3O_3^-$	87.008768
$C_2H_2NO_3^-$	88.004016
$CHN_2O_3^-$	88.999265
$C_3H_5O_3^-$	89.024418
$C_2H_3O_4^-$	91.003682
$CH_2NO_4^-$	91.998931
$C_5HO_2^-$	92.998203
$CHN_2O_4^-$	104.99418
$C_2H_3O_5^-$	106.998597
$CH_2NO_5^-$	107.993846
$C_4HO_4^-$	112.988032
$CH_2NO_6^-$	123.98876
$HN_2O_6^-$	124.984009
$C_3H_4NO_5^-$	134.009496
$C_5H_3N_4O^-$	135.031234
$C_3H_5O_6^-$	137.009161
$C_5H_3O_6^-$	158.993511
$C_{12}H_7N_2O_2^-$	211.051301

Table 4A: Negative ions identified during haze formation with 200 ppmv O_2, 0.1% CO_2, 0.1% CH_4 and N_2.

Chemical Formula	Exact Mass (Da)
CNO^-	41.998537
CHO_2^-	44.998203
NO_2^-	45.993452
CO_3^-	59.985292
NO_3^-	61.988366
$CH_3O_3^-$	63.008768
$C_3HO_2^-$	68.998203
$C_2HO_3^-$	72.993117
$C_3H_3O_3^-$	87.008768
$C_2H_2NO_3^-$	88.004016
$C_3H_5O_3^-$	89.024418
$C_2H_3O_4^-$	91.003682
$CH_2NO_4^-$	91.998931
$C_2H_3O_5^-$	106.998597
$CH_2NO_5^-$	107.993846
$C_4HO_4^-$	112.988032
$C_3H_3O_5^-$	118.998597
$CH_2NO_6^-$	123.98876
$HN_2O_6^-$	124.984009
$C_5H_3O_4^-$	127.003682
$C_4H_5O_5^-$	133.014247
$C_3H_4NO_5^-$	134.009496
$C_3H_3O_6^-$	134.993511
$C_3H_5O_6^-$	137.009161
$C_5H_3O_7^-$	174.988426

Table 5A: Negative ions identified during haze formation with 2000 ppmv O_2, 0.1% CO_2, 0.1% CH_4 and N_2.